DISS. ETH NO. 26270

Tracking and correction of motion in high-field MRI of the brain

A thesis submitted to attain the degree of

DOCTOR OF SCIENCES of ETH ZURICH

(Dr. sc. ETH Zurich)

presented by

Alexander Aranovitch

(M.Sc. TU München)

born on September 16th, 1989

citizen of Germany

accepted on the recommendation of

Prof. Dr. Klaas P. Prüssmann

Prof. Dr. Klaus Scheffler

2019

Contents

Summary

Magnetic Resonance Imaging (MRI) is an established technique for brain imaging that permits the non-invasive visualization of structures with a variety of contrasts. However, the long acquisition times of MR images increase the susceptibility to rigid-body head motion of the subject. Therefore, head motion is a major confounding factor in the clinical setting where subjects with difficulties to cooperate are regularly scanned, such as children or the elderly and also neurological patients. As a consequence, the diagnostic value is limited, scans need to be repeated and, in severe cases, useful MRI is not possible. Head motion also impedes research applications, particularly those relying on high-resolution imaging as even healthy and cooperative subjects exhibit subtle, involuntary head motion, especially during extended scan durations associated with high-resolution imaging.

To address these issues, a number of motion correction techniques have been developed. Retrospective correction methods seek to correct for motion corrupted data in a processing step, whereas prospective correction methods implement a control loop that adjusts the scan geometry during scan execution based on head tracking data. Prospective motion correction (PMC) is a general strategy to account for occurring rigid-body translation and rotation of the head during MR scans. Specific implementations differ by the way head tracking data is obtained during the scan. To date, the best tracking performance is obtained using dedicated markers attached to the subject's head. The two main categories of marker-based tracking are optical methods that

perform marker tracking with in-bore cameras and methods that localize nuclear magnetic resonance (NMR) markers using the gradient fields of the scanner. Optical methods are capable of motion detection independently of the MR sequence, which is highly convenient. However, they demand a line-of-sight between the camera and the markers which is a limiting factor for head imaging, particularly in the high-field regime where dense receiver arrays tend to obstruct visual access. NMR markers naturally overcome this limitation since they are localized using gradient fields which permeate the receiver array. Their major drawback is the interference with the MR sequence, which typically implies dedicated tracking modules interleaved with the sequence and generally increases the sequence duration. High-frequency sinusoidal gradients superimposed onto the sequence can be used to overcome the issue of sequence prolongation. However, this approach still poses an obstacle to routine use since it still requires sequence manipulation and extensive calibration of gradient dynamics.

A key goal of the present thesis is to overcome the previous limitations of motion detection with NMR markers and drive it towards versatile PMC for routine clinical and research settings.

The approach pursued to overcome the need for sequence alteration is to harvest position information from the gradient dynamics natively present in MRI sequences. To this end, the free induction decays (FIDs) of NMR markers are collected across multiple snippets distributed over one or more TR of the sequence. Joint evaluation of the marker phase time courses extracted from their FIDs results in a well-posed problem for marker localization if sufficiently diverse waveforms are observed on the three axes. This approach was validated for the case of 2D and 3D

gradient recalled echo sequences and demonstrated with phantom and in vivo measurements at 7T. It was found that the suggested approach successfully overcomes the need for sequence alteration and achieves a high tracking precision (~10 μm). The high-resolution sequence along with a finely structured phantom allowed to study also subtle effects of PMC, such as a minute decrease in effective resolution as a consequence of finite tracking precision. In vivo scans were performed with and without instructed motion and very good image quality was obtained for the motion corrected scans even when local tissue displacement amounted to a few millimeters, e.g. in the frontal lobe region.

The second effort to enhance the utility of motion detection with NMR markers is to remove the need for sequence calibration. The position of an NMR marker can be calculated given the knowledge of the gradient fields the marker was exposed to during the acquired FIDs. Changing the sequence parameters will generally affect the gradient waveforms and therefore requires re-calibration. Obviating the calibration step is achieved by adding a set of stationary markers at known positions in the laboratory frame. This set of markers serves to determine the field evolution which allows to calculate the position of head-mounted markers in the laboratory frame. The tracking performance of this approach was evaluated in terms of accuracy and precision and compared to currently employed calibration-based tracking approaches. This method not only significantly enhances the utility of NMR marker tracking by eliminating the calibration step, but the results also testify to an improved tracking performance. It eliminated systematic tracking errors caused by thermal system drift and field variations induced by

varying gradients during scan execution. A tracking precision between 5 and 30 µm is reported. The high sensitivity of field measurement also captures field noise to some degree, which further improves the tracking precision. In vivo PMC with long high-resolution scans was finally carried out to demonstrate the feasibility of motion detection with NMR markers without any sequence calibration.

The present thesis further focusses on the development, validation and demonstration of imaging methodology for the special case of high-resolution T2* weighted imaging at high field. T2* based scans offer rich contrast and are increasingly being used in neuro MRI for the detection and characterization of a range of medical conditions, such as microbleeds or neurodegenerative diseases. Apart from motion problems, such scans suffer from field fluctuations in the imaging volume induced by breathing and shoulder or limb motion, but also as a consequence of hardware imperfections. The issue of field perturbation has been addressed previously using real-time field control that aims at stabilizing the field at a reference baseline by actuating up to third-order shims based on field measurements from an array of NMR sensors around the imaging volume.

Enhancing high-resolution T2* weighted scans was pursued in this thesis by developing simultaneous prospective motion correction and real-time field control, both based on NMR sensors. This approach combined the advantages of prospective correction mechanisms, which include a thorough correction of field and motion artefacts as well as the high sensing bandwidth and precision of NMR sensors needed to adequately sample head motion and breathing induced field dynamics. This work was carried out in two steps. First, the method for joint

operation of these two correction loops was developed and characterized. It was important to consider that the two control loops both manipulate the magnetic fields in the scanner bore and at the same time derive their inputs from these fields. Therefore, a strategy was devised to minimize potential crosstalk between these two approaches that particularly relied on avoiding DC signals for marker localization and optimizing the timing of input measurements for the two loops. The stability of the proposed system was analyzed using controlled inputs and pure noise on either loop to inspect the influence on the respective other loop. Motion detection was virtually unaffected by shim actuation and the impact of rotated gradient waveforms on the field measurements was minute for common rotation angles. For larger angles, moderate field deviations were observed but no backpropagation into motion parameters occurred. Therefore, no compromises in the individual performances of the loops were detected. Phantom and in vivo measurements were performed to study the impact of each correction loop on image quality and to fully assess the impact of dual correction. Moreover, in vivo scenarios with increased field perturbations and motion were studied to demonstrate the ability of dual control to achieve good image quality in particularly challenging scenarios. Consistently improved image quality was observed and the dual correction accounted for complementary effects of field fluctuations and head motion. High image quality was also obtained in the scenarios with increased perturbations.

In a second step, the ability of the suggested dual correction approach to control for head motion and field fluctuations, being two of the most prominent physiological confounds, was utilized for the exploration of

T2* weighted scans with highest image resolution (0.25 x 0.25 x 1 mm^3) and a scan duration of one hour. 2D scans were acquired in all orientations and covered cortical regions, the subcortical brain as well as the brainstem. Depiction of caudal regions with T2* contrast is generally more challenging due to an increased exposure to field fluctuations as a consequence of closer proximity to the sources of perturbation. Dual control resulted in a high image quality of the performed scans. The obtained dataset was examined with respect to the visualization of anatomical details using anatomical atlases. A large variety of anatomical structures was identified including small brain nuclei and tracts, such as the medial longitudinal fasciculus or substructure of the red nucleus as well as subtle features in white and grey matter areas, e.g. the direct visualization of the microstructure of the corpus callosum and observation of distinct laminar contrast variation in cortical grey matter.

Altogether, this thesis contributes to the advancement of motion detection with NMR markers which facilitates their practical use for motion correction in neuro MRI. Also, a method is developed and validated which simultaneously accounts for field perturbations and head motion, rendering high-resolution T2* weighted scans more robust and yielding very promising results in such scans at ultra-high field. The proposed methods help leveraging the potential of high-field MRI.

Zusammenfassung

Die Magnetresonanztomographie (MRT) ist eine etablierte Methode zur nicht-invasiven Schnittbildgebung des Gehirns mit vielen verschiedenen Kontrasten. Allerdings ist diese Methode aufgrund der langen Bildakquisitionsdauer anfällig für Kopfbewegungen des Patienten oder Probanden. Daher gehört die Kopfbewegung zu den entscheidenden Störfaktoren im klinischen Bereich, wo Patienten mit eingeschränkter Kooperationsfähigkeit regelmäßig untersucht werden, wie zum Beispiel Kinder, ältere Menschen oder Menschen mit neurologischen Erkrankungen. Kopfbewegung während des Scans führt zu einer verminderten diagnostischen Qualität des Bildes, zur Wiederholung von Scans und in besonders schwerwiegenden Fällen ist eine sinnvolle MRT-Untersuchung unmöglich. Außerdem spielt die Kopfbewegung auch in fortgeschrittenen Forschungsanwendungen eine Rolle, insbesondere dann, wenn hochauflösende Scans gemacht werden. Denn auch gesunde Probanden mit voller Kooperationsbereitschaft können kleine, unwillkürliche Kopfbewegung während der besonders langen Bildakquisitionsdauer hochaufgelöster Scans nicht vermeiden.

Um diesem Problem zu begegnen, sind verschiedene Methoden zur Bewegungskorrektur entwickelt worden. Retrospektive Korrekturen bedienen sich der Datenverarbeitung, um Bewegungsartefakte zu beseitigen, während prospektive Methoden einen Regelkreis benutzen, um Laufzeitparameter einer MRT-Aufnahme in Echtzeit basierend auf Kopf-Tracking anzupassen. Prospektive Bewegungskorrektur versteht sich als allgemeine Strategie, um auftretende Starrkörperbewegung des

Kopfes in Form von Translation und Rotation zu berücksichtigen. Das beste Kopf-Tracking wird erreicht, indem am Kopf angebrachte Marker getrackt werden. Zu den Hauptkategorien solcher Methoden gehören einerseits optische Verfahren, welche in der Röhre des MRT-Gerätes zu installierende Kameras verwenden, um Marker zu verfolgen und andererseits Verfahren, die auf Kernspinresonanz basierende Sensoren („NMR-Marker“) verwenden, die mithilfe der magnetischen Gradientenfelder des MRT-Gerätes lokalisiert werden. Optische Methoden funktionieren unabhängig von der ausgeführten Bildgebungssequenz, was sehr praktisch ist. Allerdings benötigen sie eine freie Sichtlinie von der Kamera zu den jeweiligen Markern, was bei MRT des Kopfes ein Problem sein kann, besonders wenn die Sichtlinie durch dichte Kopfspulen unterbrochen wird, wie sie häufig im Hochfeldregime eingesetzt werden. NMR-Marker haben dieses Problem nicht, da die Gradientenfelder, die zur Positionsbestimmung verwendet werden, die Kopfspule ungehindert durchdringen. Dass die Bildgebungssequenz zum Zwecke des Trackings angepasst werden muss, ist der große Nachteil dieser Methoden. Typischerweise werden dafür spezielle Module zwischengeschaltet, was die Scandauer verlängert. Dieses Problem wird durch hochfrequente sinusförmige Gradientensignale, welche der Sequenz überlagert werden, gelöst, jedoch stellen sie für die praktische Verwendung ein Problem dar, da Eingriffe in die Sequenz weiterhin nötig sind und sie außerdem einer ausführlichen Kalibration bedürfen.

Ein wesentliches Ziel der vorliegenden Arbeit ist es, die Limitationen der Bewegungsdetektion basierend auf NMR-Markern zu beseitigen und

somit deren Eignung zur prospektiven Bewegungskorrektur in der klinischen und wissenschaftlichen Routine zu fördern.

Um Sequenzmodifikationen zum Zwecke des Trackings zu vermeiden, werden dynamische Gradientensignale verwendet, die intrinsisch in MRT-Sequenzen vorhanden sind. Dafür werden die Daten der NMR-Marker über mehrere Schnipsel hinweg verarbeitet, die innerhalb einer oder mehrerer Repetitionszeiten der Sequenz aufgenommen werden. Wenn die Schnipsel während hinreichend verschiedener Gradientendynamik aufgenommen werden, so ergeben sie ein mathematisch wohlgestelltes Problem zur Berechnung der Markerpositionen. Dieser Ansatz wurde mit 2D und 3D Gradientenecho-Scans im Phantom und in-vivo bei 7T demonstriert. Die Ergebnisse zeigten, dass eine äußerst hohe Trackingpräzision (~ 10 µm) auch ohne Sequenzänderungen möglich ist. Ein fein strukturiertes Phantom erlaubte zusammen mit der hochaufgelösten Sequenz auch subtile Effekte von prospektiver Bewegungskorrektur zu untersuchen, wie z.B. eine kleine Verminderung der effektiven Auflösung als Konsequenz endlicher Trackingpräzision. In-vivo ergaben die korrigierten Scans eine verbesserte Bildqualität, sowohl mit als auch ohne instruierter Bewegung. Dies war auch dann der Fall, wenn sich Gewebe lokal um mehrere Millimeter verschoben hat, wie etwa im Frontallappen.

Der zweite Ansatz um Bewegungsdetektion mit NMR-Markern in die praktische Anwendung zu bringen beschäftigte sich mit der Vermeidung der Kalibration zwecks Markertracking. Die Position eines NMR-Markers wird berechnet, wenn bekannt ist, unter welchen Feldern dessen Signal aufgenommen wurde. Änderung der Sequenzparameter führt im Allgemeinen zu einer Änderung der Felder und benötigt daher eine

erneute Kalibration. Indem eine zweite Gruppe von NMR-Markern stationär im Laborbezugssystem platziert wird, kann der Kalibrationsschritt vermieden werden. Dabei werden diese stationären Marker benutzt, um die Felddynamik in Echtzeit zu berechnen, sodass die am Kopf angebrachten Marker lokalisiert werden können. Dieser Ansatz wurde im Hinblick auf Akkuratesse und Präzision des Trackings untersucht und mit kalibrationsbasierten Ansätzen verglichen. Diese Methode erhöht nicht nur die praktische Anwendbarkeit von Markertracking, sondern die Ergebnisse zeigen auch eine klare Verbesserung der Trackingqualität. Systematische Trackingfehler wurden beseitigt, die bei Kalibrationsansätzen aufgrund einer Variation der ausgespielten Gradienten auftraten, wie sie z.B. als Konsequenz der Phasenkodierung oder thermischer Instabilität entstehen. Eine Präzision von 5 bis 30 µm wurde erzielt. Die Experimente deuten darauf hin, dass auch Feldrauschen mithilfe der hohen Sensitivität der Feldmessungen teilweise eingefangen wurde, was die Trackingpräzision leicht verbessert. Die praktische Umsetzbarkeit des vorgeschlagenen Ansatzes wurde in-vivo mithilfe langer hochaufgelöster Scans demonstriert.

Die vorliegende Arbeit fokussiert sich ferner auf die Entwicklung, Validierung und Demonstration einer Methode für hochauflösende T2* gewichtete Bildgebung bei hohen Feldstärken. T2* basierte Scans bieten einen reichen Kontrast und werden zunehmend für MRI des Kopfes zur Detektion und Charakterisierung von z.B. Mikroblutungen oder neurodegenerativen Erkrankungen verwendet. Neben Bewegungsproblemen sind solche Scans auch gegenüber Feldstörungen empfindlich, die aufgrund magnetischer Suszeptibilität

durch Atmung oder Bewegung der Extremitäten entstehen und daher besonders bei hohen Feldstärken relevant sind. Auch Eigenschaften der Hardware können Feldstörungen verursachen. Die Stabilisierung des Feldes im Kopfbereich wurde durch eine kürzlich entwickelte Methode erreicht, die auf Basis von NMR basierten Feldmessungen das Shimsystem steuert, um Feldstörungen im Kopfbereich auszugleichen.

In dieser Arbeit wurde simultane Feld- und Bewegungskorrektur basierend auf NMR-Sensoren entwickelt, um die Bildgebung mit hochauflösenden T2* Scans zu verbessern. Dieser Ansatz vereint die Vorteile einer umfassenden prospektiven Korrektur sowie der hohen Bandbreite und Präzision NMR basierter Messtechnik, die benötigt wird, um Kopfbewegung und durch Atmung verursachte Feldänderungen angemessen zu erfassen. Diese Arbeit wurde in zwei Schritten durchgeführt. Zunächst stand die Entwicklung und Charakterisierung dieses Systems mit zwei Regelkreisen im Vordergrund. Dabei musste beachtet werden, dass beide Regelkreise die Felder im MR-System manipulieren und dabei ihren Input aus eben diesen Feldern beziehen. Daher wurde eine Strategie entwickelt, um potenzielle Einflüsse der Regelkreise aufeinander zu minimieren, welche insbesondere auf der Vermeidung von DC Signalanteilen zur Markerlokalisierung sowie einem optimierten Timing der jeweiligen Inputmessungen beruhte. Die Stabilität des Systems wurde mithilfe kontrollierter Aktuation in beiden Regelkreisen untersucht. Diese Untersuchung ergab, dass Bewegungsdetektion unabhängig von Feldänderungen durch das Shimsystem ist und dass die Rotation der Gradientenfelder auf die Inputmessungen des Regelkreises zur Feldkorrektur für typische Winkel keine Einflüsse hat. Für größere Rotationswinkel wurde ein geringer

Einfluss gemessen, der sich jedoch nicht in die Bewegungsdetektion fortgepflanzt hat und somit der Regelkreis stabil blieb. Die Kombination der beiden Methoden ergab keine Einbußen in der Leistung der einzelnen Methoden. Phantom und in-vivo Messungen wurden durchgeführt, um die Wirkung der Korrekturmechanismen und der dualen Korrektur zu evaluieren. In-vivo wurden auch Szenarien mit erhöhter Bewegung und Feldstörung betrachtet. In allen Szenarien wurden gute Bildergebnisse erzielt und belegten, dass Bewegungs- und Feldkorrektur für komplementäre Effekte korrigieren.

In einem zweiten Schritt wurde das Potenzial dieser dualen Korrektur zum Ausgleich von Bewegungs- und Feldstörungen genutzt, um höchstaufgelöste (0.25 x 0.25 x 1 mm³) T2* gewichtete Scans mit einer Messdauer von einer Stunde durchzuführen. 2D Scans wurden in allen Orientierungen aufgenommen und deckten kortikale und subkortikale Regionen ab sowie den Hirnstamm. Dabei ist die Abbildung tieferer Hirnregionen mit T2* Kontrast allgemein schwieriger, da dort die Feldänderungen durch Atmung aufgrund der größeren Nähe zum Brustkorb besonders stark sind. Mithilfe der dualen Korrektur wurde eine gute Bildqualität erreicht und anschließend wurden anatomische Strukturen auf den Bildern identifiziert. Viele kleine Nuclei und Trakte wurden dabei identifiziert, wie z.B. der Fasciculus longitudinalis medialis oder die Substruktur des Nucleus ruber. Auch in der weißen und grauen Substanz wurden interessante Strukturen abgebildet, zum Beispiel die Faserstruktur des Corpus callosum oder eine laminare Kontrastmodulation in der kortikalen grauen Materie.

Zusammenfassend hat die vorliegende Arbeit zur Weiterentwicklung von Bewegungsdetektion mit NMR-Markern beigetragen, was deren Einsatz

für Bewegungskorrektur in der MRT des Kopfes in die praktische Anwendbarkeit rückt. Außerdem wurde eine Methode entwickelt und validiert, die gleichzeitig Kopfbewegung und Feldstörungen korrigiert, was die Robustheit von hochaufgelösten T2* gewichteten Scans erhöht und vielversprechende Ergebnisse im Hochfeld liefert. Die entwickelten Methoden helfen das Potenzial der Hochfeld-MRT umzusetzen.

Chapter 1

Introduction

1.1 The motion problem in MRI

Motion is an inevitable phenomenon when imaging living organisms, particularly animals or humans. Basic physiological processes involve motion, e.g. blood flow, breathing, or peristalsis. Motion is also present due to intentional or unintentional movements of body parts, such as head or limb motion, but also swallowing or coughing.

For magnetic resonance imaging (MRI), motion plays an ambivalent role since it may preclude successful imaging, but it may also carry important functional information. The latter aspect is seized upon by techniques such as flow and perfusion imaging or DTI (diffusion tensor imaging). The focus of the present the thesis will be on how to overcome the detrimental effects of motion, head motion in particular. Head motion is a prominent confounding factor in brain MRI, introducing artefacts such as ghosting and blurring in structural scans and inconsistencies in time series data. It is useful to distinguish between rigid-body and deformable

motion. A prominent example of the former is bulk head motion, while the heart undergoes deformable motion.

The impact of head motion during neuro MRI has recently been assessed in a clinical setting where about one fifth of the scans required repetition, resulting in an additional annual cost of an estimated $115000 USD per scanner[1]. The degree to which head motion affects image quality generally depends on the type and intensity of motion on the one hand, and the imaging technique and scan parameters used on the other hand. The latter aspect includes the sampling scheme of k-space and image resolution. High image resolution renders the scan more sensitive to even subtle head motion, and tends to require a longer acquisition time, which in turn intensifies the prevalence of motion. In the following, a few considerations on the mechanism of the detrimental effect of head motion on the image acquisition process are provided.

Image acquisition in MRI is a relatively slow and often sequential process. Scan durations of structural scans are typically on the order of minutes which is a time scale at which head motion prevails. An MR experiment consists of sequential signal excitation, signal encoding and signal reception. All steps are, in principle, affected by motion of the imaged object.

The sensitivity to motion of the imaged object becomes apparent when considering the signal $s(t)$ generated in a receive coil with sensitivity profile $\boldsymbol{c}(\boldsymbol{r})$ (neglecting relaxation and field inhomogeneities)

$$s(t) = \int_V \boldsymbol{m}(\boldsymbol{r})\, \boldsymbol{c}(\boldsymbol{r})\, e^{-i\int_0^t \omega(\boldsymbol{r},\tau)d\tau}\, d^3r \qquad [1.1]$$

where $\boldsymbol{m}(\boldsymbol{r})$ denotes the transverse magnetization, $\omega(\boldsymbol{r}, t)$ is the spatially and temporally varying precession frequency and the integral is taken over the imaging volume V. Here, demodulation to the Larmor frequency ω_0 is already assumed. The spatial and temporal dependence of $\omega(\boldsymbol{r}, t)$ is induced by dynamic gradients that can be introduced within the k-space formulation where the three spatially linear gradients $G_x(\tau), G_y(\tau)$ and $G_z(\tau)$ are used to define $k_x(t) = \gamma \int_0^t G_x(\tau) d\tau$, $k_y(t) = \gamma \int_0^t G_y(\tau) d\tau$ and $k_z(t) = \gamma \int_0^t G_z(\tau) d\tau$, with γ denoting the gyromagnetic ratio of the NMR active nucleus. Via the basic relationship $\omega = \gamma |\boldsymbol{B}|$, where $\boldsymbol{B}$ denotes the magnetic field, Eq. [1.1] becomes

$$s(\boldsymbol{k}) = \int_V \boldsymbol{m}(\boldsymbol{r})\, \boldsymbol{c}(\boldsymbol{r})\, e^{-i\boldsymbol{k}\boldsymbol{r}}\, d^3r \qquad [1.2]$$

where the time dependence is now implicit in $\boldsymbol{k} = \left[k_x(t), k_y(t), k_z(t)\right]^T$. In practice, many such readouts are acquired successively such that different values of $\boldsymbol{k}$ are sampled, which can be controlled by the applied gradient fields. The goal is to obtain sufficient coverage of k-space, so that an inverse Fourier transform can be used to determine the image content associated with $\boldsymbol{m}(\boldsymbol{r})$. Note that the above equation usually covers a rather short time period, typically up to several tens of milliseconds, since the transverse magnetization decays exponentially. Changes of $\boldsymbol{r}$ on this time scale are rather small for the case of head motion. However, it is the sequential collection of data from Eq. [1.2] which spans the time scale of minutes on which significant head motion occurs, causing inconsistencies in the acquired signals and being the reason why head motion is a confound in practice. This difference in time scales is sometimes conceptualized by the terms “intra-view” and “inter-

view". Rigid-body motion is usually described by $\boldsymbol{r}' = \boldsymbol{R}\boldsymbol{r} + \boldsymbol{t}$, using a rotation matrix $\boldsymbol{R} \in SO(3)$ and a translation vector $\boldsymbol{t}$.

The inconsistencies are induced via different mechanisms that are reflected in the individual terms in Eq. [1.2], which all depend on $\boldsymbol{r}$**.** The method employed for the correction of head motion in this thesis will address two of these mechanisms. First, changes in $\boldsymbol{r}$ from one readout to the next cause inconsistencies in the phase accrual $\boldsymbol{k}\,\boldsymbol{r}$ in the individual readouts. Specifically, translation of the object causes a phase shift of the acquired samples, while a rotation of the object causes a corresponding rotation of k-space. Second, the transverse magnetization $\boldsymbol{m}(\boldsymbol{r})$, which is generated during the excitation process, is affected by motion in that a mismatch between the defined excitation volume and the actually excited volume is caused. The consequence is signal acquired from false volumes and alteration of spin history.

The general strategy to solve these issues is to ensure a fixed geometric relationship between the imaged object and the scan geometry to guarantee consistent image encoding and volumes of excitation. This is achieved through run-time updates of scan geometry in accordance with the current head pose and is referred to as prospective motion correction (PMC), which will be detailed in chapter 1.3.

There are some mechanisms related to head motion that cause additional inconsistencies in the image acquisition process, which tend to manifest to a lesser extent though, and will not be addressed by the method for motion correction employed in this thesis. There is the spatial non-uniformness of the coil sensitivity profile $\boldsymbol{c}(\boldsymbol{r})$ as well as of the transmit RF field $\boldsymbol{B}_1^{transmit}(\boldsymbol{r}, t)$ used for spin excitation, which is

implicitly contained in $\boldsymbol{m}(\boldsymbol{r})$. Moreover, a spatially dependent profile of gradient non-linearity causes inconsistent encoding as tissue moves through different areas within the imaging volume. Furthermore, the head moves through spatially dependent field inhomogeneities resulting in static off-resonances $\Delta\omega(\boldsymbol{r})$, that alter the precession frequency and can be formalized using an additional term $e^{\mathrm{i}\Delta\omega(\boldsymbol{r})t}$ in the integrand of Eq. [1.1]. Field inhomogeneities also emerge as a consequence of the head's susceptibility distribution and can change if the head orientation changes with respect to the main magnetic field.

Finally, motion of other body parts than the head also induces field changes in the head volume and thus perturbs the image acquisition process. Such susceptibility induced field changes are proportional to the main magnetic field and are therefore more pronounced at higher field strengths. A prominent source of such fluctuations in the head volume are breathing induced field variations, that superimpose a temporally varying field modulation of low spatial complexity, which tends to be stronger in caudal regions of the brain[2]. Shoulder or limb motion are also contributing factors as well as hardware imperfections. Field variations not only modify the effective encoding fields, but spatial variation of the field across a voxel also results in faster decay of transverse magnetization and thus potential signal loss. T2* weighted imaging is particularly sensitive to field fluctuations due to its long echo times.

Field variations stemming from outside of the imaging volume will be addressed in this thesis by employing a technique called "real-time feedback for spatiotemporal field stabilization" developed by Duerst et

al[3] that seeks to counter such field fluctuations by real-time actuation of up to third-order shims.

1.2 Head motion compensation techniques in brain MRI

Preventing or reducing head motion is a straightforward way of minimizing the motion problem in MRI and is undoubtedly an important means in any scan. This can be achieved by subject instruction and immobilization through pads or even customized head moulds[4]. Reducing the extent of motion can also be achieved with shorter scan times, e.g. through undersampling in k-space[5,6].

Finally, a range of motion correction techniques has been developed to address the motion problem directly. As mentioned in the previous section, the effect of motion on the image encoding process in the Fourier domain is well defined. This motivates different techniques to retrospectively correct for corrupted data. If the occurred motion is known, the acquired raw data can be corrected by adjusting the k-space samples for translation and rotation effects, i.e. by applying phase corrections[7] and interpolating rotated k-space samples[8]. If motion is unknown, retrospective correction based on image quality metrics can be performed, that iteratively estimates patient motion by minimizing a cost function in image space. Examples of such methods are autofocus methods relying on image entropy[9,10]. A general framework for retrospective correction that can also handle non-rigid motion has been proposed by Batchelor et al.[11]

The drawbacks of retrospective correction methods arise from the fact that they are generally of limited efficacy in the case of through-plane motion that alters the excitation volume and they tend to be

computationally expensive. Moreover, since rotational motion between k-space lines causes corresponding rotation between these lines, Nyquist violations may occur. These limitations can be overcome by prospective correction methods that perform a very thorough correction by means of real-time geometry updates based on head tracking data. Prospective motion correction is introduced and reviewed in the following section.

1.3 Prospective motion correction

Prospective motion correction (PMC) is a strategy to address rigid-body head motion by maintaining a constant geometric relationship between the scan geometry and the head pose. To this end, head tracking data is obtained during the scan and fed into a real-time control loop that adjusts the field-of-view during image acquisition. It accounts for translational motion by adapting the frequency of transmit RF pulses and the receiver frequency and phase. Rotations are compensated by corresponding rotation of gradient waveforms, which is accomplished by multiplication with the associated rotation matrix. As opposed to retrospective correction approaches, the corrected image is usually available directly upon scan completion. PMC is a general strategy and specific implementations differ with respect to how head tracking data is obtained. A review is provided by Maclaren et al[12] and Godenschweger et al[13]. Note that while real-time head tracking is necessary for the PMC principle, it can also be used for retrospective correction of the acquired data.

Ideally, a method for head tracking should have a high tracking rate, provide high precision and accuracy and exhibit a high degree of practicality. The latter includes aspects such as subject comfort, minimal

effect on workflows and reliability of the tracking data. A method that excels at every aspect has not been developed until the present day. However, several methods have been proposed that offer partial coverage of desirable properties and a considerable effort is governed by addressing the respective remaining issues and developing new tracking modalities in quest of an optimal solution. Most methods can be categorized into one of the following three classes[12]: MR navigators, optical methods and field detection methods with NMR markers.

MR navigators do not require additional hardware and derive head tracking data from partial sampling of k-space or from acquisition of low-resolution images. Different strategies for k-space traversal have been proposed (e.g. spherical navigator[14], cloverleaf navigator[15]) along with several techniques to acquire auxiliary images (e.g. volumetric navigator[16], fat image navigator[17]). Navigators usually involve a trade-off between tracking performance and a decrease in scan efficiency since the navigator pulse sequence needs to be interleaved with the imaging sequence.

Higher tracking performance along with a fast update rate can be obtained using dedicated hardware. Optical methods use in-bore cameras that track head-mounted markers, e.g. a moiré phase pattern[18] or a checkerboard pattern[19]. Apart from very good tracking performance, the appeal of optical methods lies in that they perform head tracking independently from the executed MR sequence and thus sequence considerations are not an issue. However, this entails a cross-calibration step to align the coordinate system of the camera to the scanner coordinate system[20]. Optical methods do require a line of sight between the camera and the marker which may be challenging in the high-field

regime where tightly fitting receiver arrays tend to be used. Recent approaches seek to perform head tracking without dedicated markers by using a structured light approach[21] or stereo-vision[22].

Field detection methods localize a set of markers containing an NMR active sample whose FID (free induction decay) signal is obtained in the presence of field gradients. Marker excitation and signal reception can be performed using either components of the MR system via inductive coupling[23] or dedicated transmit and receive electronics[24]. Such methods are convenient as they do not require a line-of-sight, nor do they require cross-calibration since the markers are localized inherently in the scanner coordinate system. However, sequence considerations are necessary to localize the markers. For instance, dedicated tracking modules can be interleaved with the sequence[25,26] or sinusoidal gradients can be superimposed onto the sequence[24]. In the present work, a method for marker tracking will be presented that does not require sequence modifications[27].

Apart from these three categories, even more head tracking methods exist and are emerging, which rely on different technologies. Notably, pick-up coils can be localized through voltages induced by gradient switching and have been utilized jointly with hall sensors and accelerometers[28,29]. Recently, tracking based on the transmission of short-wave radiofrequency and reflection by a wireless marker has been proposed[30].

1.4 NMR field probes

NMR field probes[31,32] are sensors that measure the magnetic field. They do so by performing NMR of a suitable sample, such as 1-H or 19-F,

which is doped to achieve desired relaxation times. Such probes are designed using tailored geometry and magnetostatics to achieve excellent field homogeneity across the sample such that long-lived FID signals can be acquired. Upon excitation, the accrued phase of an NMR field probe reflects the time integral over the magnetic field magnitude experienced by the probe.

A schematic of a field probe is shown in Figure 1.1. The probe head consists of an NMR active sample confined in a glass capillary. For signal excitation and detection, a solenoid coil is wound around the capillary. The capillary and coil are encapsulated by an epoxy polymer whose susceptibility is matched to that of the solenoid coil. The probe head is connected to tuning and matching electronics via an air-matched neck.

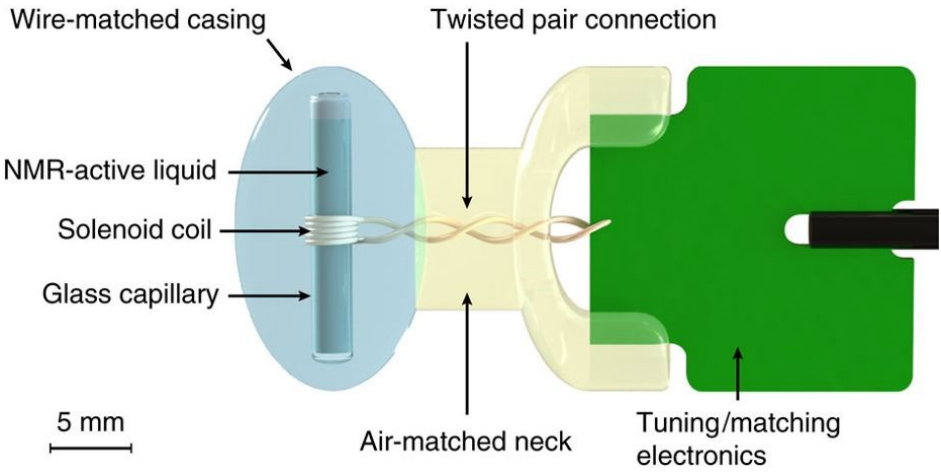

Figure 1.1: Schematic of the employed NMR field probe. The probe head consists of a glass capillary filled with an NMR active liquid and a solenoid coil is used for spin excitation and signal detection. The capillary is confined in an epoxy polymer with a wire-matched

susceptibility. An air-matched neck made of epoxy polymer connects the probe head to the tuning and matching electronics. Figure from Gross et al, Nature Communications (2016).

Relying on an NMR active sample other than hydrogen, e.g. 19-Flourine, allows to run the probes concurrently with the scan. The field probes are operated using a stand-alone system that comprises receive and excitation electronics and a block for digitization and digital signal processing[33]. T/R switches and amplifiers are placed in proximity of the field probe array inside the scanner bore. Digitization and digital signal processing are based on National Instruments hardware (Austin, TX, USA) and include an analog-to-digital-converter (ADC) and field programmable gate arrays (FPGA). Higher-level signal processing, such as extraction and unwrapping of phase from the probe signals, are performed on a CPU. Synchronization to sequence execution on the MR system can be achieved via programmable trigger signals emitted from the MR system.

One application of field probes in MRI is spatiotemporal magnetic field monitoring[34] which measures the field evolution in the scanner bore. When the probe positions are known, a set of spatial basis functions can be used to determine the dynamic field coefficients from the measured probe phases and such data can be used for image reconstruction.

In this thesis, motion detection is accomplished by tracking head-mounted NMR field probes. In principle, this pursues an approach converse to spatiotemporal magnetic field monitoring in that knowledge of the field evolution is used to calculate the probe position from its accrued phase. Suitable methods and signal processing for tracking NMR field probes are presented in chapter 2 and 3 of this thesis.

1.5 Thesis outline

Chapter 2 introduces a novel method for tracking NMR field probes. State-of-the-art methods require additions to the MR pulse sequence for the purpose of marker tracking (e.g. interleaving dedicated tracking modules[25,35] or superposition of sinusoidal gradients[24]) which constitutes one of the major drawbacks of NMR marker based PMC. Here, a new method is developed that relies on high-frequency signal content natively present in pulse sequences due to gradient switching events. The key idea is to harvest sufficiently diverse tracking signals from one or multiple TR of the sequence such that joint evaluation of the acquired phase snippets results in a mathematically well-conditioned problem. The presented method is characterized and validated in PMC of high-resolution scans both on a phantom and in vivo.

Chapter 3 presents an advanced approach to tracking NMR markers which leverages previously developed tracking methods by obviating the associated calibration procedures and providing an enhanced tracking performance. Instead of calibrating the relevant field dynamics in a preceding scan, a second set of field probes is placed in the laboratory frame that serves to calculate the field dynamics needed for localizing a set of moving markers. An in-depth analysis of tracking performance is performed by juxtaposition of the presented approach to calibration-based approaches along with in vivo demonstration in challenging scan scenarios characterized by high resolution and extended scan duration.

Chapter 4 describes a dual correction approach for prospective correction of both head motion and field fluctuations. The latter can be caused by breathing or limb motion and this effect is increased at high field. A method is developed to jointly operate PMC and real-time

feedback for spatiotemporal field stabilization, both based on NMR field probes. The stability of these two real-time control systems deriving their inputs from the fields they actuate is analyzed and the impact of the combined correction approach is evaluated systematically in phantom and in vivo measurements for the case of T2* weighted imaging. In vivo measurements include normal scenarios as well as situations with increased motion and field perturbation.

Chapter 5 builds on the ability of the dual control method developed in the previous chapter to counter field perturbations and to control the problem of head motion simultaneously. This allows to depict subcortical brain regions with T2* weighting at very high spatial resolution. Within the applications of UHF imaging such scans are of increasing interest for detecting and characterizing neurologic disorders[36]. The feasibility and quality of such scans with a duration of one hour and a resolution of 0.25 x 0.25 x 1 mm³ is explored in this chapter.

Chapter 2

Prospective motion correction with NMR markers using only native sequence elements

Published in:

Aranovitch A., Haeberlin M., Gross S., Dietrich B.E., Wilm B., Brunner D.O., Schmid T., Luechinger R. and Pruessmann K.P. Prospective motion correction with NMR markers using only native sequence elements. *Magnetic Resonance in Medicine*. 2018;79(4):2046-2056. doi:10.1002/mrm.26877

Awarded the 2018 ISMRM Young Investigator Award: I.I Rabi award

2.1 Introduction

Head motion is a frequent problem in MRI of the brain, causing various image artefacts[37]. A range of methods have been devised to tackle this issue. Retrospective techniques[9,11,38,39] address motion-related perturbations purely by means of data processing and image reconstruction. This approach is attractive in that it does not require run-time intervention at the console level. However, it faces limitations when motion alters volumes of excitation and spin history in intractable ways, e.g., upon through-plane motion in 2D scans. Prospective motion correction (PMC) solves this issue by continuous updates of sequence geometry based on run-time tracking of head motion[12]. Current tracking modalities include optical methods, MR navigators and NMR markers, and will be briefly surveyed in the following.

Established optical methods[18–20,40,41] use a camera to track one or several markers attached to the subject's head. Their key advantages are independence from the MR sequence and good tracking performance. Precisions (RMSE) of 1-50 µm and 0.005°-0.1° have been reported for the detection of translations and rotations, respectively. Optical methods require lines of sight between the camera and the markers and cross-calibration to align the coordinate systems of the camera and the MR system. Recent developments explore the intriguing prospect of optical head tracking even without markers[22,42].

MR navigators obtain motion tracking data interleaved with image acquisition segments by either acquiring auxiliary low resolution images[16,17,43] or partially sampling k-space in one, two or three dimensions[14,15]. No additional hardware is required for their operation, which is a key advantage in a practical setting. However, MR navigators

usually add to the scan duration, require additional RF pulses, and complicate sequence design by altering spin evolution.

NMR-marker methods derive the position of head-mounted NMR samples from FIDs acquired in the presence of field gradients. They do not require lines of sight and inherently operate in the scanner coordinate system. However, like navigators, the use of NMR markers is closely linked with gradient operation and thus with sequence considerations. Most implementations so far have relied on dedicated tracking modules interleaved with each given imaging sequence and thus adding to the scan duration[25,35,44]. The tracking modules commonly consist of successive intervals of constant gradient strength along each axis. Tracking precision thus achieved has been on the order of 10 µm.

To avoid the time overhead for tracking NMR markers it has recently been proposed to perform position encoding simultaneously with the actual sequence by superimposed gradient tones[24]. Operating such tones at high frequencies additionally avoids errors induced by field drift and field fluctuations of physiological origin. However, the insertion of gradient tones still requires sequence modification and may not always be possible without impairing the initial sequence design. In echo-planar imaging (EPI), in-plane marker tracking has been achieved without additions to the sequence, relying on marker acquisition during the EPI readout[45]. However, this approach has been limited to moderate image resolution such that the markers do not dephase during readouts. It is also hardly applicable to standard spin-warp sequences whose gradient waveforms exhibit much less high-frequency content and associated tracking sensitivity.

The goal of the present work is to overcome these limitations and accomplish PMC based on NMR markers in standard imaging techniques and without sequence modification. The main idea to this end is to render marker signals deliberately short-lived and aggregate position information from sets of complementary signal snippets (Figure 2.1Figure 1.1a). Complementarity renders partial dephasing tolerable, which in turn permits increasing the marker diameter to boost tracking sensitivity. We explore this approach for PMC in 2D T2*-weighted and 3D MPRAGE imaging as sample cases. It is first assessed in terms of marker tracking precision and consistency as well as imaging performance in the absence of motion. The applied scenario of PMC in vivo is then demonstrated with involuntary and instructed movement.

2.2 Methods

2.2.1 Concept

Localization of each NMR marker is based on a set of short FID snippets acquired at selected times during the given sequence (Figure 2.1). The marker position is computed by joint processing of the FID phase time courses, involving calibration data obtained with fixed markers. For head tracking and prospective motion correction a set of markers is mounted on a headset worn by the subject.

2.2.2 Phase model and signal processing

As described in Ref. (34), the magnetic field in the scanner bore can be decomposed into static and dynamic components such that the phase accrual of an NMR marker at position $\boldsymbol{r} = [x, y, z]$ is given by

$$\phi(\boldsymbol{r},t) = \gamma \int_0^t \big(\boldsymbol{g}(\tau)\cdot \boldsymbol{r} + g_0(\tau)\big)d\tau + \omega_0(\boldsymbol{r})t + \eta(t) \qquad [2.1]$$

where γ denotes the gyromagnetic ratio of the marker droplet, the vector $\boldsymbol{g}(t) = [g_x(t), g_y(t), g_z(t)]$ contains the gradient waveforms, $g_0(t)$ describes any dynamics of the spatially uniform field component, and $\omega_0(\boldsymbol{r})$ is the marker's baseline Larmor frequency arising from the main magnetic field and any non-uniformities that originate from nearby magnetized matter including the marker itself. $\eta(t)$ denotes detection noise as analyzed in more depth in ([31]). It is of Gaussian zero-mean statistics with standard deviation inversely proportional to the FID's signal-to-noise ratio at time t. Considering M snippets, $\phi_i(t)$ shall denote the phase of the i-th snippet, acquired under $\boldsymbol{g}_i(t)$ and $g_{0,i}(t)$.

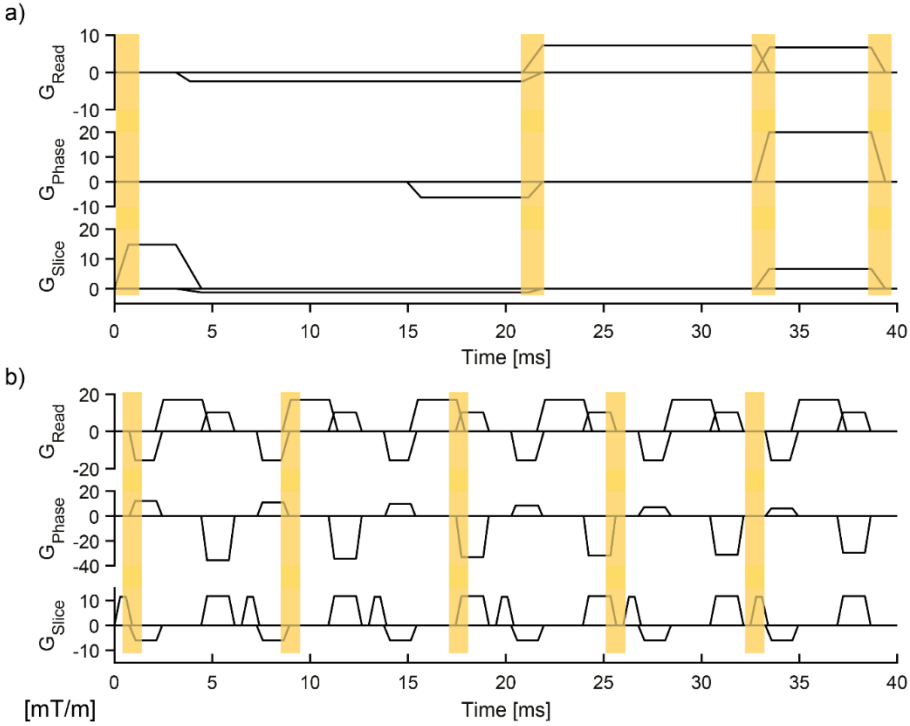

Figure 2.1: Diagrams of the sequences used in this work. The orange rectangles indicate snippets of marker acquisition. a) T2-weighted gradient-echo sequence with four complementary snippets spread across one TR. Marker signals were cropped to remove dephased parts, resulting in effective snippet durations of 540, 911, 869, and 901 µs (left to right). b) Imaging section of a 3D MPRAGE sequence with five complementary snippets spread across five consecutive TR. Cropping yielded snippet durations of 445, 511, 400, 403, and 300 µs (left to right). Each snippet pattern was repeated throughout the respective scan.*

In practice, the phase observations are obtained as discrete samples reflecting a time-discretized form of Eq. [2.1]. The snippets are cropped such that dephased parts of the signals are excluded. As a result, the snippets are of variable length. The next processing step is temporal differentiation to map the unknown ω_0 to DC, which will later be excluded from position fitting. On the discrete data, the temporal derivative is carried out by a first-order difference operator of corresponding size ($\boldsymbol{D}_i$):

$$\boldsymbol{D}_i\boldsymbol{\phi}_i = \gamma\boldsymbol{G}_i\boldsymbol{r} + \gamma\boldsymbol{g}_{0,i} + \omega_0(\boldsymbol{r})\cdot\mathbf{1} + \boldsymbol{D}_i\boldsymbol{\eta}_i \qquad [2.2]$$

where the vector $\boldsymbol{\phi}_i$ contains the sampled phase values, $\boldsymbol{G}_i$ is a matrix of three columns containing the discretized gradient waveforms $\boldsymbol{g}_i(t)$, $\boldsymbol{g}_{0,i}$ and $\boldsymbol{\eta}_i$ are discretizations of $g_{0,i}(t)$, $\eta_i(t)$ in vector form, and $\mathbf{1} = (1,1,\dots,1)^{\mathrm{T}}$.

The next step is frequency-selective filtering, which serves two purposes. To eliminate field drift and potential physiological field perturbation relative to the calibration state, low-frequency field change is discarded along with DC. High frequencies above a suitable threshold are equally eliminated since they carry mostly noise. Formally the filter operation amounts to a projection operator $\boldsymbol{F}_i$ that projects Eq. [2.2] onto the subspace of oscillations at specified pass-band frequencies. For convenience, the latter are chosen to be harmonics of the inverse snippet duration such that $\boldsymbol{F}_i\cdot\mathbf{1} = 0$ and the dependence on $\omega_0(\boldsymbol{r})$ vanishes:

$$\boldsymbol{F}_i\boldsymbol{D}_i\boldsymbol{\phi}_i = \gamma\boldsymbol{F}_i\boldsymbol{G}_i\cdot\boldsymbol{r} + \gamma\boldsymbol{F}_i\boldsymbol{g}_{0,i} + \boldsymbol{F}_i\boldsymbol{D}_i\boldsymbol{\eta}_i\ . \qquad [2.3]$$

Each snippet yields one such equation with $\boldsymbol{r}$ as the unknown and noise contamination $\boldsymbol{\eta}_i$. For joint solving the snippet equations are concatenated by stacking the $\boldsymbol{\phi}_i$, $\boldsymbol{G}_i$, $\boldsymbol{g}_{0,i}$ along the time dimension to

form $\boldsymbol{\phi}$, $\boldsymbol{G}$, $\boldsymbol{g}_0$. The aggregate operators $\boldsymbol{D}, \boldsymbol{F}$ are constructed by arranging the $\boldsymbol{D}_i, \boldsymbol{F}_i$ in block-diagonal form. Figure 2.2 illustrates the aggregate equation for the case of $M = 4$ snippets and three selected frequencies. Neglecting noise statistics, the best solution for $\boldsymbol{r}$ is the least-squares estimate

$$\boldsymbol{r} = (\boldsymbol{F}\boldsymbol{G})^{+}\boldsymbol{F}(\gamma^{-1}\boldsymbol{D}\boldsymbol{\phi} - \boldsymbol{g}_0) \quad [2.4]$$

with $(\cdot)^{+}$ denoting the Moore-Penrose pseudoinverse. This solution was used in the experimental part of this work. An SNR-optimal estimate accounting for noise propagation is outlined in the appendix.

Evaluating Eq. [2.4] requires knowledge of $\boldsymbol{F}(\boldsymbol{G}|\boldsymbol{g}_0)$, i.e., of the relevant spectral components of 0th- and 1st-order magnetic fields during selected snippets. In this work, $\boldsymbol{F}(\boldsymbol{G}|\boldsymbol{g}_0)$ is determined by calibration and will be referred to as the calibration matrix. In the calibration measurement the sequence in question and snippet acquisition are performed with four NMR markers at reference positions $\boldsymbol{r}_{I-IV}$ determined by preceding FID frequency measurement under constant gradients. Concatenating the resulting phase snippets results in four overall phase time courses $\boldsymbol{\phi}_{I-IV}$. $\boldsymbol{F}(\boldsymbol{G}|\boldsymbol{g}_0)$ is then calculated by solving Eq. [2.3], neglecting noise:

$$\boldsymbol{F}(\boldsymbol{G}|\boldsymbol{g}_0) = \gamma^{-1}\boldsymbol{F}\boldsymbol{D}(\boldsymbol{\phi}_I \quad \boldsymbol{\phi}_{II} \quad \boldsymbol{\phi}_{III} \quad \boldsymbol{\phi}_{IV})\begin{pmatrix} \boldsymbol{r}_I & \boldsymbol{r}_{II} & \boldsymbol{r}_{III} & \boldsymbol{r}_{IV} \\ 1 & 1 & 1 & 1 \end{pmatrix}^{-1}. \quad [2.5]$$

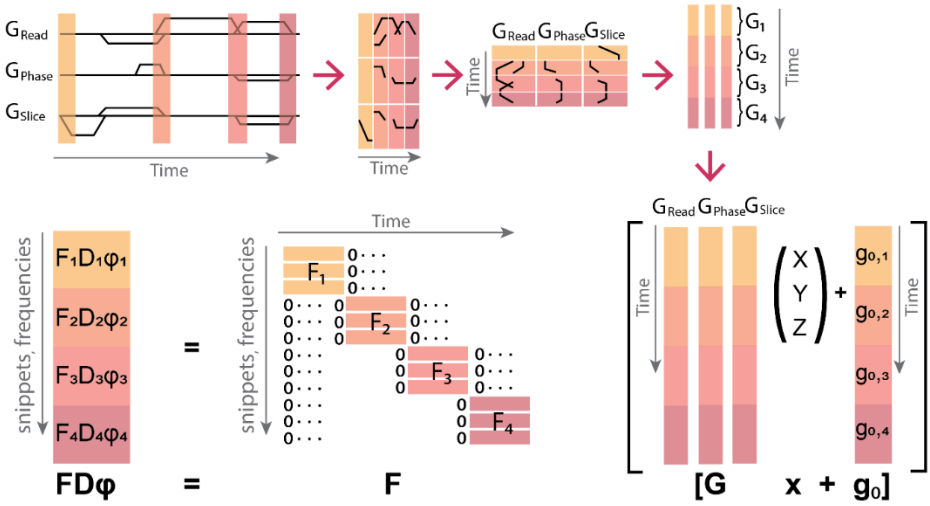

Figure 2.2: Graphical representation of Eq. [2.3] for the sample case of four snippets and three projection frequencies. Top: The gradient waveforms during snippet acquisition form the columns of the matrix $\boldsymbol{G}$. Bottom: Eq. [2.3]. The blocks $\boldsymbol{F}_i$ of the block-diagonal matrix $\boldsymbol{F}$ each contain three rows, one per projection frequency.

2.2.3 Snippet timing and marker design

Snippet timing and marker design choices are governed by the goal to determine marker positions with maximum sensitivity. The sensitivity is determined by the SNR of marker FIDs as well as the power and conditioning of $\boldsymbol{FG}$. Therefore, the three columns of $\boldsymbol{FG}$ must be optimized in terms of power and linear independence.

To capture high-frequency waveform content, snippets should generally coincide with gradient switching. For position tracking at high rate, sufficient sets of such snippets need to be accommodated within short time, requiring rapid re-excitation of the markers. To this end, the markers' relaxation time T1 must be suitably short. The markers' T2 must

be sufficiently long to cover switching events of typically 0.1-1 ms in length but not much longer to prevent spurious echoes upon re-excitation. Under strong gradients, dephasing may dominate T2 relaxation as a mechanism of signal decay, causing the usable snippet duration to vary.

The snippet duration determines the frequency resolution of acquired phase time courses. The shorter a snippet is, the higher the first harmonic frequency that can be inspected without DC contamination. This is important to consider because gradients are typically switched following ramp functions whose spectral content declines quickly with frequency. The tracking precision thus drops quickly as the observation time decreases.

Conveniently, a full set of snippets for position determination is accommodated within each sequence TR (Figure 2.1a). When suitable snippets are too closely spaced for individual excitation within a single sequence TR, their acquisition may be distributed over multiple TR (Figure 2.1b).

Regarding marker construction, the key design parameter is the diameter of the NMR-active droplet. Increasing the diameter boosts the volume of the droplet and thus the marker's primary SNR. At the same time the diameter must be kept sufficiently small to limit dephasing and the associated loss of effective snippet duration.

2.2.4 Hardware

All experiments were performed on a 7T Philips Achieva system (Philips Healthcare, Best, The Netherlands) with a 32-channel head receive array (Nova Medical, Wilmington, MA, USA). Four 19F NMR markers[31]

(sample diameter = 1.3 mm, T1 = 2.1 ms, T2 = 1.2 ms) were attached to a 3D-printed headset (Figure 2.3). The markers were connected by thin, flexible cables (static bend radius = 15 mm) to minimize forces exerted by the cables on the markers. The headset design was guided by the main objective to establish a stable rigid-body relationship with the skull. For robustness against facial expressions, a suitable support point was identified between the eye-brows on the nasion.

The markers were operated independently of the scanner, using a stand-alone console[33]. It performed marker excitation and acquisition controlled by programmable trigger signals from the MRI system. All signal processing was programmed in LabVIEW (National Instruments, Houston, TX, USA) and resulting geometry updates were transmitted over an Ethernet connection to the MRI console using an external data interface[46] (Philips Healthcare, Best, The Netherlands).

2.2.5 MRI sequences and snippet distribution

To demonstrate the proposed approach it was used for PMC in structural brain imaging. High-resolution scans of long duration were chosen, because they are particularly sensitive to motion and best reveal the effectiveness of PMC.

A first set of experiments used a T2*-weighted 2D gradient-echo sequence (resolution: 0.3 mm x 0.3 mm x 2 mm, FOV: 230 mm x 230 mm x 58 mm, TE: 25 ms, TR: 48 ms, flip-angle: 45°, slices: 15, flow compensation, duration: 9:13 min). Four 1.2 ms snippets were collected within each TR as indicated in Figure 2.1a.

Figure 2.3: Four NMR markers were attached to a 3D-printed headset. The support points of the headset are above the ears and between the eyebrows on the nasion.

Secondly, a 3D MPRAGE sequence was performed (resolution: 0.7 mm x 0.7 mm x 1.4 mm, FOV: 220 mm x 220 mm x 80 mm, TE: 2.9 ms, TR: 6.5 ms, flip-angle: 7°, TI: 1200 ms, 2 averages, duration: 9:42 min). Five 1 ms snippets were distributed over five consecutive TR in a pattern repeated throughout the readout train (Figure 2.1b). At the beginning of each readout train, initial position information was available from start-up cycles present in the sequence.

Both sequences included gradient spoiling on the phase encoding axis such that in every TR either the phase encoding gradient, the crusher gradient, or both were non-zero and thus yielding tracking information.

2.2.6 Prospective motion correction

Rotations and translations were considered relative to the head position at the beginning of each scan. To this end the marker positions in this state were stored as references. For subsequent sets of marker positions the rotation matrix and translation vector relative to the reference set were computed according to Umeyama[47].

Image reconstruction was performed on the scanner using the system's regular procedures such that results were available immediately after scan completion.

2.2.7 Calibration

For calibration, each sequence was first carried out without the subject and the markers mounted in a fixed tetrahedral arrangement to ensure good conditioning of the matrix inversion in Eq. [2.5]. The reference positions $\boldsymbol{r}_{I-IV}$ of the four markers were obtained by determining the FID frequency changes induced by static gradients $(2.5\ mT/m)$ along the three axes. $\boldsymbol{F}(\boldsymbol{G}|\boldsymbol{g}_0)$ was calculated via Eq. [2.5].

2.2.8 Assessment of precision, consistency and latency

To assess tracking precision a time series of marker positions and derived rigid-body motion parameters were collected with the four markers at fixed positions. The tracking precision was determined as the standard deviation of the respective parameter series.

The phase model (Eq. [2.1]) assumes that spatial field variation is limited to zeroth and first order, an assumption that must generally be made for PMC via just the gradient system and RF chains. Slight violations of this model occur, however, when residual eddy currents give rise to higher-order field perturbations. To estimate the scale of resulting

inconsistency, position measurement with dynamic and static gradient fields was compared. The four markers were fixed in places emulating typical positioning on the headset in vivo. Time series of marker positions were then obtained with the proposed tracking approach, followed by measurement of reference positions with static gradients as described above for calibration. The differences between the latter and the temporal means of the former were taken as a measure of inconsistency.

The latency of the PMC system is the time by which the scanner geometry settings lag behind the actual head position. Part of this lag is due to data acquisition, processing, and transfer to the scanner. Another contribution is the time that elapses between the arrival of a geometry update at the scanner host and the execution of the correspondingly updated waveforms and RF frequencies. The latter was accessed by run-time logging of scan parameters. The duration of data processing was measured using timers in the computation loops. The duration of data acquisition for one tracking step is given by the snippet distribution. Half of this duration adds to the net lag. Data transfer speed via TCP was not amenable to measurement but considered negligible compared to the other delays.

2.2.9 Phantom experiment

The T2*-weighted imaging experiment was performed on a spherical fBIRN phantom[48] (Agar/NiCl2, diameter = 18cm) to verify identical image quality with and without motion correction in a static setting. Differences caused by PMC indicate finite tracking precision or systematic error in the correction loop. Suitable image structure was present due to stationary air bubbles emphasized by T2* contrast.

2.2.10 In vivo experiments

Both sequences were used for brain imaging in healthy volunteers according to the applicable ethics regulations. Two motion scenarios were studied with and without motion correction. In the first scenario the subject was asked to remain as still as possible. In the second scenario the subject was asked to perform slight head rotation about the z-axis and later to return to the initial position. Instructions for the two movements were given at 3:30min/5min and 3min/5min into the T2*-weighted and MPRAGE sequences, respectively.

2.3 Results

2.3.1 Calibration

The phase snippets were cropped according to dephasing, resulting in effective durations of 540-901 µs and 300-511 µs, respectively, in the T2* and MPRAGE cases (Figure 2.1, caption).

The projection operator $\boldsymbol{F}$ included harmonics 1-5 of the respective inverse snippet duration, resulting in an approximate frequency range of 1.1-16.7 kHz.

2.3.2 Precision, consistency, and latency

Figure 2.4 (rows 1-6) shows the time series of rigid-body parameters acquired with both sequences to measure tracking precision. The two distinct episodes in the MPRAGE results reflect the two averages performed with this sequence. Standard deviation of rigid-body parameters and individual marker positions are displayed in Table 2.1a. At 5-30 µm the standard deviations of rigid-body translations are smaller than the respective image resolutions by factors between 50 and 200.

As evident from Figure 2.4, the precision of motion parameters changes with phase encoding. This is a consequence of changes in the respective matrices $\boldsymbol{FG}$, which alter noise propagation. Underlying changes in eigenvalue distribution are also reflected in the condition number of $\boldsymbol{FG}$ plotted at the bottom of the figure. In the T2*-weighted case this effect can be observed in the x and y translation time-series, for instance. In the MPRAGE sequence the condition number is modulated periodically because there are two phase encoding directions.

The results of the consistency experiment are shown in Table 2.1b. Discrepancy between measurements with dynamic and static gradients ranged between few tens of μm and just under 200 μm and tended to be largest in the z direction.

A full set of snippets was acquired within 40 ms for the T2* sequence and 32.5 ms for the MPRAGE sequence, contributing 20 ms and 16.25 ms to the latency, respectively. Signal processing was clocked at 12 ms. The console lag amounted to 96 ms for the T2*-weighted sequence and 45.5 ms for the MPRAGE sequence, respectively. The total latency thus amounted to 128 ms for the T2*-weighted sequence and 73.75 ms for the MPRAGE sequence, at update intervals of 48 ms and 39 ms, respectively.

a) Precision							
Sequence		**Translation [µm]**			**Rotation [mdeg]**		
		X	**Y**	**Z**	**X**	**Y**	**Z**
T2*w	marker 1	8.9	8.1	14.5	-	-	-
	marker 2	8.0	7.4	13.2	-	-	-
	marker 3	8.9	7.9	14.2	-	-	-
	marker 4	7.6	7.0	12.6	-	-	-
	rigid-body	6.1	6.3	10.5	3	4	4
MPRAGE	marker 1	9.3	9.6	32.0	-	-	-
	marker 2	6.6	6.0	19.6	-	-	-
	marker 3	12.0	13.6	46.9	-	-	-
	marker 4	6.9	6.9	23.0	-	-	-
	rigid-body	5.5	8.2	27.4	5	10	6

b) Inconsistency				
	Marker	**X [µm]**	**Y [µm]**	**Z [µm]**
T2*w	1	55	-12	153
	2	-26	73	188
	3	-118	134	115
	4	26	75	130
MPRAGE	1	-21	-81	68
	2	-82	-29	171
	3	-155	28	111
	4	13	-16	88

Table 2.1: a) Tracking precision for individual markers and rigid-body motion parameters, determined in the absence of motion. Standard deviation shown. b) Inconsistency of position determination with dynamic and static gradients.

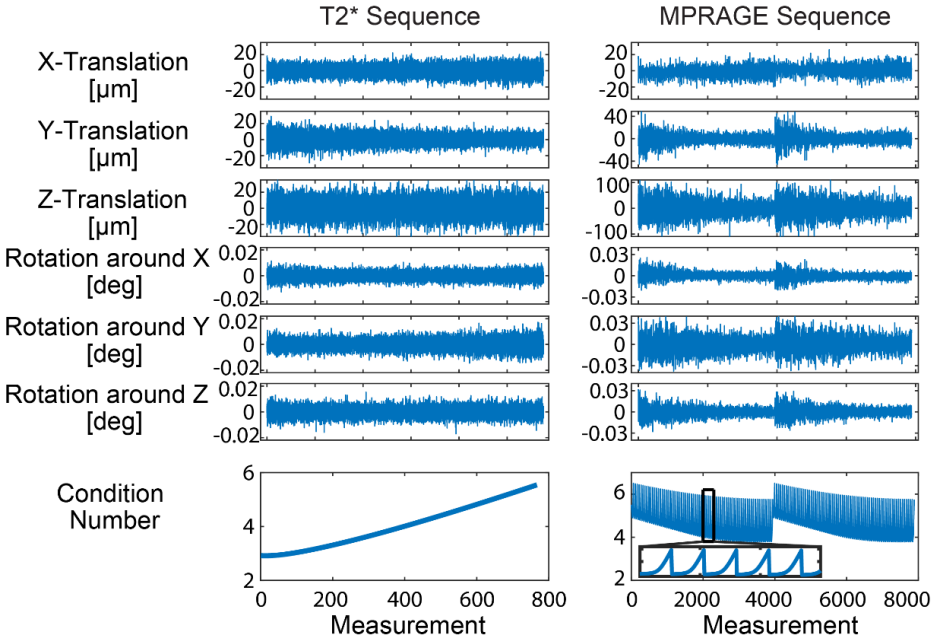

Figure 2.4: Rows 1-6: Time-series of measured rigid-body parameters in the absence of motion. These time-series were used to estimate tracking precision. Row 7: Condition numbers of the corresponding calibration matrices $\boldsymbol{F}(\boldsymbol{G}|\boldsymbol{g}_0)$. a) T2 sequence: the drift in the condition number is caused by change in the phase encoding gradient and leads to a slight change in the precision of rigid-body parameters over time. b) 3D MPRAGE sequence: phase encoding in the slice and phase directions causes periodic modulation of the condition number (zoomed detail on the bottom right).*

2.3.3 Phantom experiment

Figure 2.5a/b shows the results of phantom imaging without and with PMC including close-up views. No conspicuous differences can be seen at this level. To highlight subtle discrepancies, difference images were computed. Since motion correction was applied with respect to the first

TR of a sequence, the two images are systematically shifted and rotated with respect to each other to the degree that the respective first acquisitions differed due to noise. To counteract this effect, co-registration was performed. The difference image before co-registration (Figure 2.5c) exhibits distinct dark and bright edge enhancements in the order of 5-10 percent that reflect the mentioned effect. Upon co-registration these patterns vanish (Figure 2.5d). The residual differences are yet subtler and vary regionally. In one of the zoomed areas in Figure 2.5d circular edges at a level of a few percent can still be discerned, reflecting minute differences in effective resolution. These are a general consequence of finite tracking precision, which, at several µm, amounted to a few percent of the voxel size.

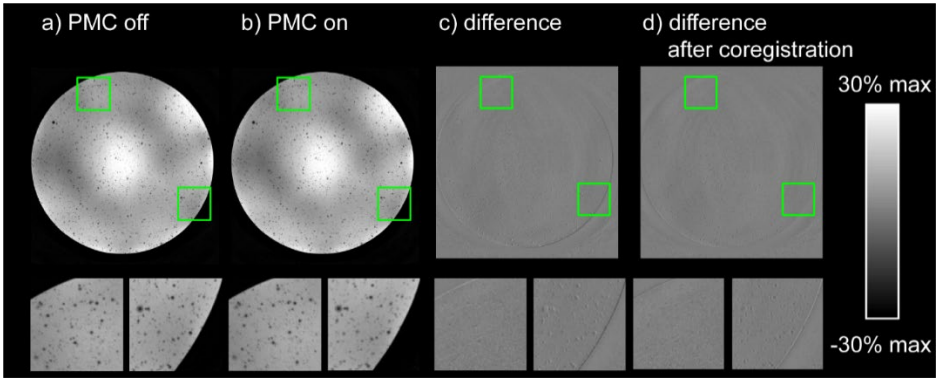

Figure 2.5: T2-weighted imaging (0.3 x 0.3 x 2 mm^3) in the phantom. In the absence of motion, scans without (a) and with (b) motion correction yield virtually identical images. Residual tracking errors at the micron level result in very small differences (c) that further decrease upon co-registration (d). The difference images are scaled to +/- 30 % of the maximum image intensity of the uncorrected image.*

2.3.4 In vivo experiments

T2-weighted imaging*

Figure 2.6 shows two representative slices from the data acquired without deliberate motion along with the corresponding head tracking data. The latter indicates a similar extent of motion during both scans, permitting a fair comparison. Moreover, zoomed views of translation along FH are shown, illustrating high tracking sensitivity by details of breathing-related and cardio-ballistic head movement. Due to motion during and between scans the shown slices do not fully match. However, they permit juxtaposition of corresponding structures. Significant motion artefacts resulted from involuntary head motion (Figure 2.6a-c). The strongest artefacts are seen frontally where rolling motion about the back of the head causes the largest excursions. PMC removed these to a large degree (Figure 2.6d-f) and achieved better depiction particularly of grey-white-matter boundaries and cortical veins.

Instructed subtle head motion caused further degradation of image quality in the uncorrected experiment (Figure 2.7a-c). Again, PMC based on head tracking as proposed here achieved substantially better image quality (Figure 2.7d-f) at a level similar to the correction result with only involuntary motion. The motion pattern was similar in the two experiments (Figure 2.7, right) with net tissue displacements of a few millimeters in the frontal region.

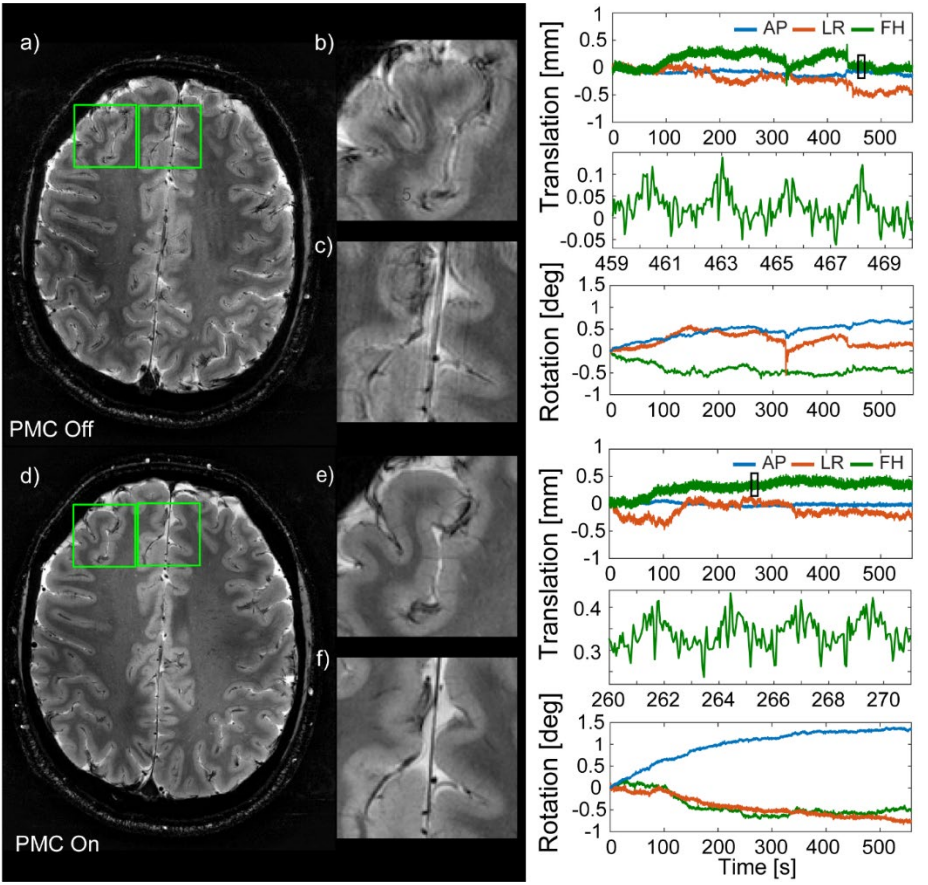

Figure 2.6: Left: T2-weighted imaging in vivo without deliberate motion. At an in-plane resolution of 0.3 mm even small involuntary head motion notably degrades image quality in the uncorrected case (a-c). With motion correction, image quality is significantly improved (d-f). Right: corresponding motion parameters. Zoomed details of translation in the FH direction reveal minute head motion due to breathing and pulsatile blood flow.*

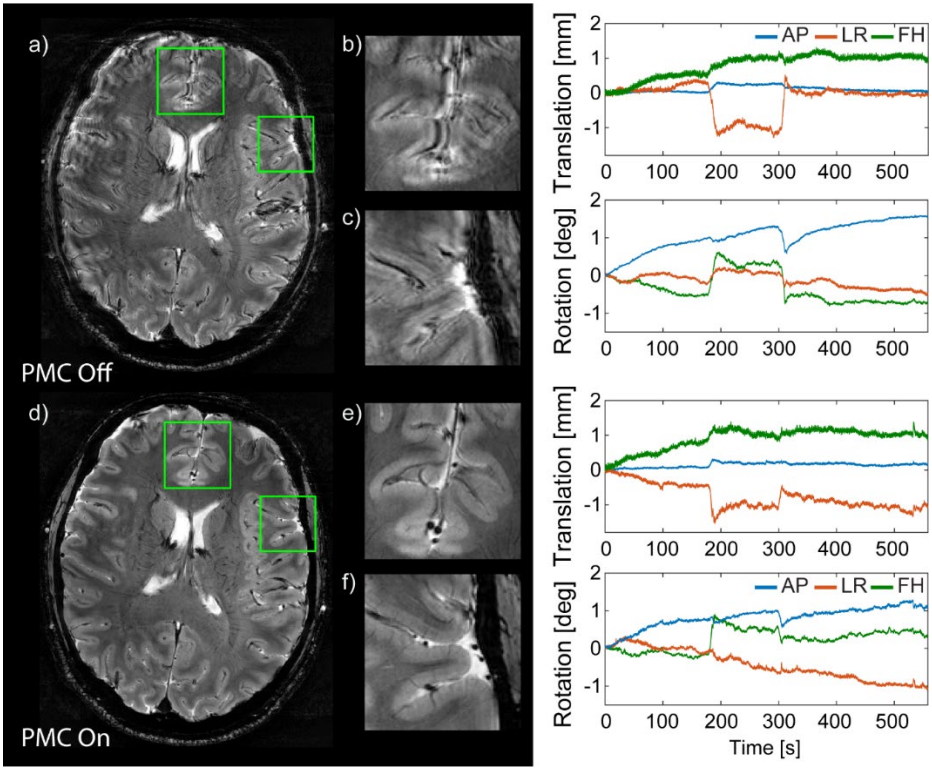

Figure 2.7: Left: T2-weighted imaging in vivo with subtle instructed head rotation about the FH axis. Significant motion artefacts (a-c) were virtually eliminated by PMC (d-f), resulting in image quality comparable to the PMC results without intentional motion. Right: corresponding rigid-body motion parameters.*

MPRAGE

Figure 2.8 shows a selected slice and the tracking data obtained with MPRAGE and the subject lying still. The degree of inadvertent head motion was again very similar in the corrected and uncorrected case. The uncorrected image alone (Figure 2.8a/b) does not exhibit obvious image artefacts. However, close inspection does reveal noticeable

improvement by PMC (Figure 2.8c/d). It rendered grey-white-matter boundaries sharper and enhanced the contrast of small structures, such as vessels, by reducing motion-related blurring.

With instructed subtle motion the uncorrected scan yielded clearly degraded image quality (Figure 2.9a/e). The contours of grey and white matter are blurred particularly in the frontal region. PMC recovered the cortex boundary and improved the depiction of small or thin features like vessels and meninges (Figure 2.9b/f). Decreased image quality can be observed already in the first average of this scan (Figure 2.9c) and the degree of consistency between the two averages is illustrated by computing the respective difference image (Figure 2.9d/h). The two uncorrected images exhibit significant differences (Figure 2.9d) while the two consecutively motion-corrected images are not only individually sharper (Figure 2.9g) but also coincide very well (Figure 2.9h).

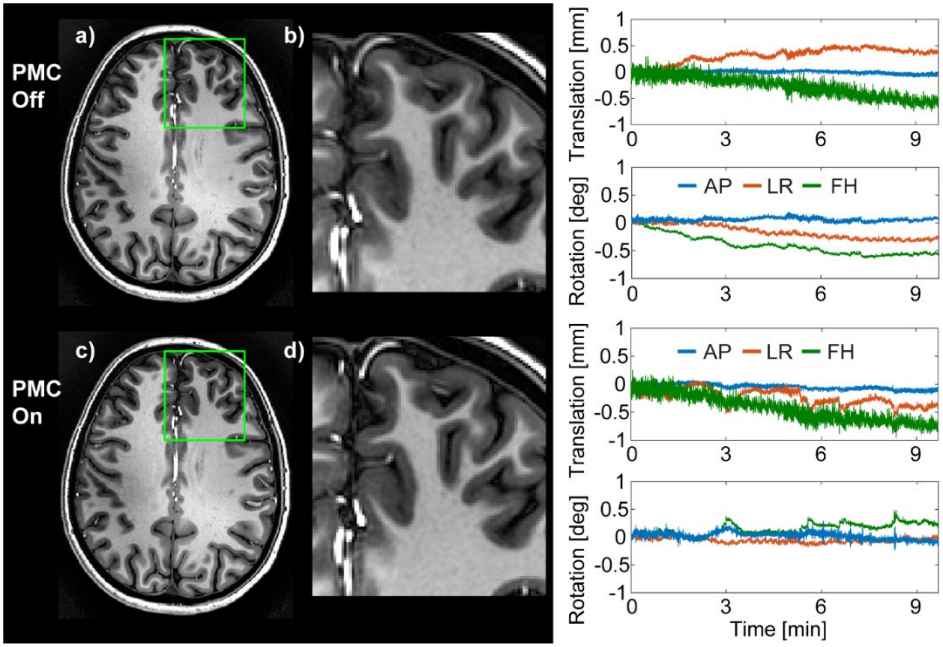

Figure 2.8: Left: 3D MPRAGE imaging in the presence of minimal, involuntary motion. The uncorrected image does not suffer from obvious motion artefacts (a,b). Nonetheless, the image obtained with PMC still proves slightly sharper upon close inspection (d). Right: corresponding motion parameters.

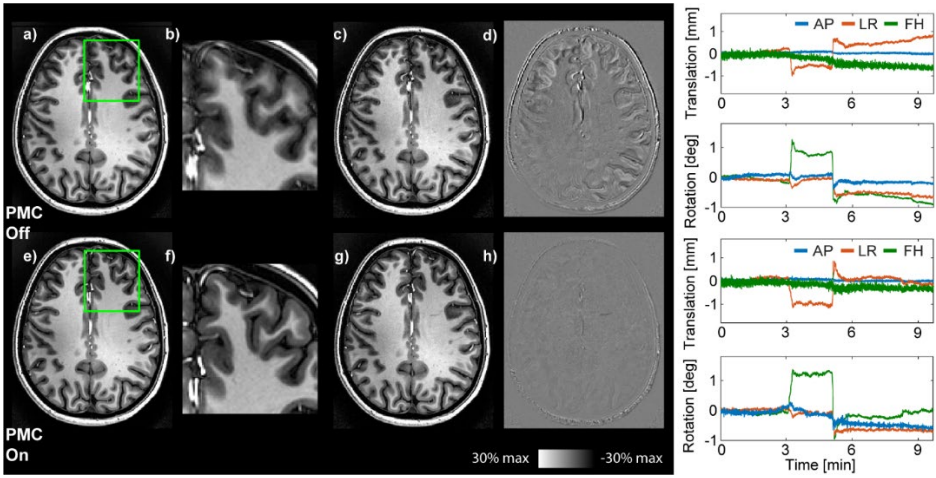

Figure 2.9: In the uncorrected 3D MPRAGE case, subtle intentional motion resulted in visibly reduced image quality (a,b). Decreased quality is also visible in the first partial image of the two-NSA scan (c). The difference between the two consecutive partial results is shown in d). PMC prevented motion artefact in the partial (g) and compound images (e,f), and largely eliminated the difference between the two partial images (h). The difference images are scaled to +/- 30% of the maximum image intensity of the first partial image. Right: Motion parameters. Intentional motion was of similar magnitude in the two scans.

2.4 Discussion

The results of this work indicate that the transition to sets of brief observations in rapid succession enables tracking of NMR markers with unaltered standard imaging sequences. High tracking precision was confirmed in phantom measurements and is also reflected by the observation of minute head motion related to breathing and pulsatile blood flow, as previously accomplished with cameras[18,40]. Used for PMC, the proposed approach has been successfully deployed for imaging at

spatial resolution on an order previously unattained with NMR marker approaches.

Compared to navigators and other NMR-marker approaches the presented method is particularly useful when sequences do not offer suitable periods for inserting navigators or tracking modules. In other cases, too, it is arguably more convenient in that it removes the need for sequence modification and saves scan time otherwise spent on tracking-specific sequence elements. The method thus offers advantages similar to those of optical motion tracking. Compared to the latter, its key advantage consists in remaining feasible when dense head arrays or accessories such as mirrors or goggles obstruct lines of sight.

The presented tracking method can be used with basically all types of MRI sequences. To obtain a well-posed inverse problem and ensure sufficient high-frequency dynamics, snippets are best placed capturing gradient switching events as outlined in the methods section. For the large class of spin-warp sequences this can be done by snippet choices similar to those used in this work, among others. Sequences containing many gradient switching events, such as EPI or spiral readouts, are even better suited. In EPI, for instance, sets of snippets can be spread across the readout covering the slopes of the read gradient along with the phase-encoding blips. In spiral imaging, the oscillations in quadrature of the two readout gradients perform highly efficient in-plane position encoding, especially during earlier revolutions when markers are still far from dephasing. Through-plane tracking can generally be achieved by placing a snippet on a slope of the slice-excitation gradient. On all axes, fast gradient switching with high slew rate is generally favorable as it tends to shift waveform power to higher frequencies. Marker dephasing

depends rather on gradient moments and is generally unfavorable but not critical as long as the set of snippets defines a well-posed inverse problem overall.

Relying on the sequence itself for marker localization requires some gradients to be present on each axis, which is generally true for common MR techniques. In spin-warp sequences, however, the phase-encoding axis can require closer consideration since the phase encoder vanishes at the center of k-space. This is not a problem in common spoiled sequences with a crusher gradient on the phase-encoding axis. In fully balanced sequences, however, the phase encoding gradient and its rephaser do vanish in the same repetition. In this case, for maximum tracking capability a minor sequence modification will again be necessary, e.g., the introduction of a bipolar crusher gradient or a brief gradient tone. A simpler alternative is to tolerate a brief period without motion updates. Since balanced sequences typically use very short TR to contain banding artifacts the tracking outage will generally be rather short.

Longer periods without gradient activity occur in sequences with extensive intervals for spin evolution such as MPRAGE. During such breaks geometry updates are not required. However, they are needed as soon as gradient activity resumes. To account for motion during the break, up-to-date tracking data can be readily obtained by common start-up cycles as done in this work. An alternative, albeit at the expense of slight sequence alteration, is inserting a set of gradient tones during the break[24]. Another special situation is an extended period that does exhibit gradient activity but not on all axes. For instance, during the labeling period of ASL sequences, which form an important case for motion

correction[49], the proposed method could acquire tracking data only along the slice dimension. To obtain full tracking information in time, startup cycles or gradient tones could again be used.

In this work, head tracking was performed at 20-25 Hz. The proposed approach limits the potential for increasing the tracking rate in that several snippets will usually be required and the NMR probes need to recover in between. In the sequences reported here the number of snippets could be reduced by one or two, albeit at the expense of tracking sensitivity. The current tracking rate of 20-25 Hz is less than typical rates achieved with optical systems. However, it may be expected to capture a large part of actual head dynamics. An earlier investigation in three volunteers found involuntary head motion with significant spectral content up to about 12 Hz[50]. Even at higher tracking rates the bandwidth of PMC will be limited by how quickly the MRI system reacts to geometry updates. In the present work, sequence adaptation was performed on a per-TR basis, i.e., at most newly for every k-space line. Extremely fast motion or large latency could additionally be addressed by Kalman filtering[51] or reacquisition of k-space lines affected by motion beyond a given threshold.

The successful PMC experiments with high-resolution sequences performed in this work suggest that tracking performance was sufficient both in terms of precision and accuracy. If needed, there are several ways to further improve tracking performance. A higher-order spherical harmonic field model could be adopted to compute the marker position. Carrying out a higher-order field calibration would require either more than four markers, or repeating the calibration with the set of four markers and placing them at different locations each time. Further

improving the tracking precision could be achieved by SNR optimal signal processing, as indicated in the appendix, and by a matched-filter version of the frequency selective approach, weighting the Fourier components according to their power in the spectrum. Instead of projecting on a subset of frequencies, every phase signal could also simply be demeaned, thus removing just the DC signal content. In this case, very high frequency signal components, which are mostly contaminated by noise, would be included in the computations. However, there can be situations where this would already result in sufficient tracking precision.

The calibration procedure chosen in this work requires to run the entire sequence at least once before MR experiments with PMC can be performed. Once a calibration is obtained for a given sequence and snippet distribution, it can be used with any subject. Even though the calibration is required only once, it may be considered cumbersome if it consumes a large amount of time, such as in cases of long MR sequences. Acquiring only a fraction of phase encoding steps and appropriate interpolation for the rest could reduce the calibration time by at least one order of magnitude. The underlying assumption would be linearity of the phase encoder's gradient stepping, or some low dimensional polynomial behavior. Another approach to reduce calibration time would be using gradient input response functions (GIRFs) resulting from a gradient system characterization[52]. Assuming a linear time-invariant system, the responses of the gradient coils could be predicted and this would serve as a calibration for marker tracking. Both approaches would require a careful analysis of potential localization errors caused by the underlying assumptions. Ultimately, obtaining a calibration prior to the scan could be avoided by concurrent field

measurements, performed by an additional set of field probes in the laboratory frame.

Like other methods of NMR-marker tracking the strategy proposed in this work requires mounting the markers on the anatomy of interest. Here this was achieved with a dedicated headset, which established a sufficiently robust rigid-body relationship with the skull in the experiments reported. Nonetheless, marker fixation and the design of the markers themselves remain key challenges. One caveat in the current prototype setup is that the subject must not move so much that the headset hits obstacles such as foam pads or the inside of the receiver array. With cooperative subjects this issue has been effectively solved by suitable instructions. For subjects with more difficulty lying still, coil arrays with larger inner diameter are one option. A robust if less comfortable alternative are custom-made bite-bars that have been successfully used for optical tracking during long high-resolution scans[53,54]. Regarding the markers one appealing perspective is the transition to wireless operation as demonstrated with inductive coupling[23]. For tracking with just native sequence elements, wireless implementations will need to be optimized particularly for SNR yield.

PMC corrects for rigid-body head motion but head motion may cause secondary effects which are not corrected for by PMC and result in residual image artefacts. The quality of the shim can degrade and the spatial variation of coil sensitivities has to be accounted for, if parallel imaging is performed[55]. Recent work addressed susceptibility-induced local field changes, e.g. occurring due to displacement of tissue-air interfaces in the brain[56]. Many parameters determine the extent to which these secondary motion effects will manifest in the prospectively motion

corrected images, e.g. field strength, intensity of motion, contrast and resolution of the sequence.

In conclusion, we developed a general method that enables precise tracking of active NMR markers using only sequence elements naturally present in the sequence. This removes a limitation that is shared by virtually all existing techniques for tracking NMR markers, namely the need to interfere with standard sequence design by inserting signals dedicated to marker tracking.

2.5 Appendix

An SNR optimal solution for $\boldsymbol{r}$ in Eq. [2.3] can be obtained by considering the covariance matrix $\boldsymbol{\psi_\phi}$ of the marker's phase noise, which contains the time dependent variances $\sigma_\phi^2(t)$ on its diagonal. These values can be obtained during an initial noise measurement of the marker signal. They can be determined by $\sigma_\phi(t) = \sqrt{0.5} \cdot \sigma_s \cdot |s(t)|^{-1}$ where $s(t)$ denotes the complex-valued probe signal and σ_s is its standard deviation[31]. The SNR optimal solution reads

$$\boldsymbol{r} = \left(\boldsymbol{G^H F^H \psi_{FD\phi}^{-1} F G}\right)^{-1} \boldsymbol{G^H F^H \psi_{FD\phi}^{-1} F}(\gamma^{-1}\boldsymbol{D\phi} - \boldsymbol{g}_0) \qquad [2.6]$$

with $\boldsymbol{\psi_{FD\phi}} = \boldsymbol{FD\psi_\phi D^H F^H}$. The noise covariance matrix of $\boldsymbol{r}$ is given by

$$\boldsymbol{\psi_r} = \gamma^{-2}\left(\boldsymbol{G^H F^H \psi_{FD\phi}^{-1} F G}\right)^{-1} . \qquad [2.7]$$

Obtaining the noise-optimal solution is computationally more demanding than the linear solution (Eq. [2.4]). This may be challenging in PMC with high update rate.

Chapter 3

Motion detection with NMR markers using real-time field tracking in the laboratory frame

Published in:

Aranovitch A., Haeberlin M., Gross S., Dietrich B.E., Reber J., Schmid T., Pruessmann K.P. Motion detection with NMR markers using real-time field tracking in the laboratory frame. *Magnetic Resonance in Medicine*. doi: 10.1002/mrm.28094

3.1 Introduction

Head motion is a key confound in brain MRI, causing various types of image artifacts[37]. Motion-related problems are particularly prominent in high-resolution imaging, with long scans, and in subjects with difficulty to cooperate. In the clinical realm, head motion is a frequent cause of limited diagnostic quality and re-scans, leading to substantial additional cost[1].

Strategies for correcting head motion are typically categorized into retrospective and prospective approaches. Retrospective techniques[10,11,39] rely on data processing alone and thus tend to face limitations in the presence of through-plane motion, upon motion-related spin-history effects, or when motion causes partial undersampling of k-space in the head frame of reference. Prospective motion correction (PMC) addresses the problem more completely by real-time update of the scan geometry based on head tracking data[12]. In addition to being quite effective at mitigating artefacts, PMC is also convenient in that it requires only minimal changes to image reconstruction and thus is readily compatible with standard operation of clinical MRI systems.

Towards routine use, PMC should rely on suitably fast and precise motion detection, function robustly in all patients, and not slow down or complicate workflows. In the following, the most common means of motion tracking shall be briefly reviewed with respect to these challenges.

Navigator methods estimate motion based on MR data from the head itself, obtained with repeated additional readouts that sample dedicated k-space trajectories or acquire low-resolution images[14–17]. Navigator methods are convenient in that they do not require additional hardware

and related preparation such as the mounting of markers. However, the additional readouts can be difficult to reconcile with preferred sequence and parameter choices and they generally come at the expense of scan time. The precision and temporal resolution of navigator-based tracking are subject to a trade-off between tracking performance and overall scan speed.

Higher tracking rates and precision tend to be achieved with optical methods and NMR marker approaches, which both rely on specific additional hardware. Most optical methods use in-bore camera systems that track optical markers attached to the subject's head[18,19,40]. Recent developments pursue head tracking also without specific markers, using structured light[21,57] or stereo vision[22]. Towards routine use of optical tracking, one challenge is to guarantee a line-of-sight between the camera and the markers or the head, which is not always available. Marker visibility has recently been improved by use of multiple cameras[40] or multiple markers[58]. However, dense coil arrays still tend to force optical markers to reach outside the array, requiring very robust mounting, e.g., with the help of bite bars or dental braces[53]. In addition, optical approaches require a step of cross-calibration that establishes the coordinate transform between the camera and the MRI system. This aspect, too, is a target of ongoing improvements such as recently reported in Ref. (59) for the case of coil-mounted cameras.

Tracking of head-mounted NMR markers relies on observing the MRI system's own gradient fields and thus intrinsically yields positions in the scanner coordinate system[25,24,35,60]. It does not require a line-of-sight because the gradient fields permeate the radiofrequency setup and the body virtually unhindered. One drawback, shared with navigators, has

been the need to interleave dedicated tracking modules with each host sequence[25,35]. To address this issue, NMR marker tracking has recently been modified to work with superimposed gradient tones[24] and even without any sequence modification at all[27]. Eliminating sequence overhead this step has brought NMR tracking closer to routine utility. However, it still faces another challenge, which is the need for accurate knowledge of gradient field dynamics. In practice, gradient fields deviate from nominal behavior for a variety of reasons, including eddy currents, amplifier and coil characteristics, concomitant fields, and system heating. So far, gradient field dynamics used for NMR tracking have been determined by calibration measurements prior to in vivo scanning. Such calibration must typically be redone for different sequence parameters and scan geometries, making it rather time demanding. This time overhead is arguably the chief remaining obstacle to routine use of NMR marker tracking. In addition, pre-calibration is somewhat inaccurate when thermal hardware changes, other drifts, or external perturbations cause field dynamics to differ between scan repetitions.

The goal of the present work is to advance NMR-based motion tracking by overcoming the limitations associated with pre-calibration. To this end, head-mounted NMR markers are complemented by field tracking in the laboratory frame, using a second, stationary set of NMR markers. Simultaneous recordings in the two frames of reference are then used to track motion during actual imaging. The tracking performance achieved in this way is compared with current calibration approaches. The utility of the proposed approach is illustrated by prospective motion correction in examples of high-resolution brain imaging.

3.2 Methods

3.2.1 Concept

Translation and rotation of the head are viewed as a rigid-body coordinate transform between the head and laboratory frames of reference. The transform is found by observing magnetic field evolution in the scanner bore with two sets of NMR markers simultaneously, one stationary in the lab frame and one head-mounted (Figure 3.1). First, the output of the lab-frame markers is used to calculate an expansion of the magnetic field in laboratory coordinates. The field expansion then serves to calculate the lab-frame coordinates of the head-frame markers, which determine the desired coordinate transform.

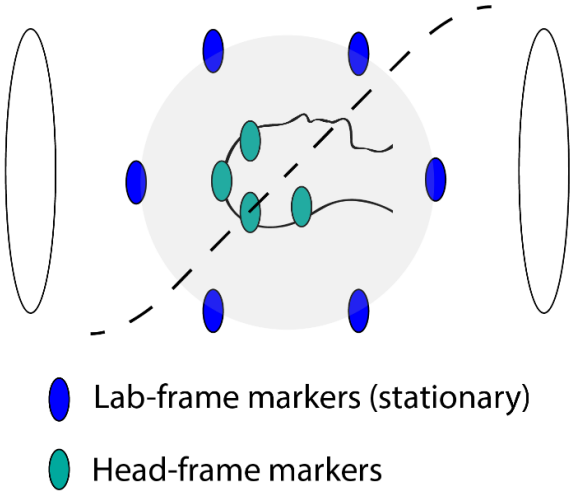

Figure 3.1: Marker localization using real-time field tracking. Two sets of NMR markers observe the same magnetic field evolution. The set of stationary markers at known positions is used to determine a time-resolved field expansion, which then serves to translate the recordings

of the head-frame markers into their coordinates and the implied coordinate transform.

3.2.2 Localization of NMR markers using real-time field tracking in the laboratory frame

An NMR marker at position $\mathbf{r} = [x, y, z]^T$ in laboratory coordinates yields an FID signal with phase

$$\phi(t) = \gamma \int_0^t |\mathbf{B}(\mathbf{r}, \tau)| \, d\tau \qquad [3.1]$$

where $\mathbf{B}(\mathbf{r}, \tau)$ denotes the magnetic field evolution in the scanner bore and γ is the gyromagnetic ratio of the marker droplet. Due to the different roles of lab-frame and head-frame markers, related symbols and expressions will be distinguished by sub- and superscripts L and H in the following. Taking the time derivative of marker phase yields

$$\dot{\phi}_i^{\mathrm{L}}(t) = \gamma_{\mathrm{L}} \left| \mathbf{B}\left(\mathbf{r}_i^{\mathrm{L}}, t\right) \right| \qquad [3.2a]$$

$$\dot{\phi}_j^{\mathrm{H}}(t) = \gamma_{\mathrm{H}} \left| \mathbf{B}\left(\mathbf{r}_j^{\mathrm{H}}, t\right) \right| \qquad [3.2b]$$

where the indices i, j count the lab-frame and head-frame markers, respectively. To relate the two systems of equations, $|\mathbf{B}(\mathbf{r}, t)|$ is expanded into $|\mathbf{B}(\mathbf{r}, t)| = B_0(\mathbf{r}) + \sum g_l(t) f_l(\mathbf{r})$, where the sum accounts for dynamic field contributions generated by gradients, using a suitable set of basis functions, $f_l(\mathbf{r})$, along with the coefficients $g_l(t)$. In the present work, a first-order basis is chosen, comprising the four terms $f_0(\mathbf{r}) = 1$, $f_1(\mathbf{r}) = x$, $f_2(\mathbf{r}) = y$, $f_3(\mathbf{r}) = z$. $B_0(\mathbf{r})$ includes the static background field and all field contributions that change slowly relative to the millisecond time scale of marker signal acquisition. These include, particularly, susceptibility effects related to breathing and other motion, and magnet drift.

Inserting the field expansion into Eqs. [2a,b] yields

$$\dot{\phi}_i^{\mathrm{L}}(t) = \gamma_{\mathrm{L}}\left(B_0(\mathbf{r}_i^{\mathrm{L}}) + \sum f_l(\mathbf{r}_i^{\mathrm{L}})g_l(t)\right) \quad [3.3a]$$

$$\dot{\phi}_j^{\mathrm{H}}(t) = \gamma_{\mathrm{H}}\left(B_0(\mathbf{r}_j^{\mathrm{H}}) + \sum f_l(\mathbf{r}_j^{\mathrm{H}})g_l(t)\right). \quad [3.3b]$$

Since the two sets of markers are subject to the same field evolution, the positions of the head-frame markers can be determined from those of the lab-frame markers. The strategy of doing so is to solve Eq. 3.3a for $g_l(t)$, substitute the results into Eq. 3.3b, and then solve for $\mathbf{r}_j^{\mathrm{H}}$.

Practically, the phase time courses of the markers are obtained as discrete time samples and stored in vectors $\boldsymbol{\phi}_i^{\mathrm{L}}$ and $\boldsymbol{\phi}_j^{\mathrm{H}}$, respectively. Arranging the phase time courses of n lab-frame markers and m head-frame markers in matrices yields $\boldsymbol{\Phi}_{\mathrm{L}} = [\boldsymbol{\phi}_1^{\mathrm{L}} \ldots \boldsymbol{\phi}_n^{\mathrm{L}}]$ and $\boldsymbol{\Phi}_{\mathrm{H}} = [\boldsymbol{\phi}_1^{\mathrm{H}} \ldots \boldsymbol{\phi}_m^{\mathrm{H}}]$. The positions of the markers are assembled in $\mathbf{R}_{\mathrm{L}} = [\mathbf{r}_1^{\mathrm{L}} \ldots \mathbf{r}_n^{\mathrm{L}}]$ and $\mathbf{R}_{\mathrm{H}} = [\mathbf{r}_1^{\mathrm{H}} \ldots \mathbf{r}_m^{\mathrm{H}}]$. Let $\mathbf{1}_n$, $\mathbf{1}_m$ denote row vectors of length n and m, respectively, filled with ones. Using a first-order difference operator $\mathbf{D}$, the discretized form of Eq. 3.3b can then be written as

$$\mathbf{D}\boldsymbol{\Phi}_{\mathrm{H}} = \gamma_{\mathrm{H}}[\mathbf{B}_0 + \mathbf{g}_0\mathbf{1}_m + \mathbf{G}\mathbf{R}_{\mathrm{H}}] \quad [3.4]$$

where $\mathbf{B}_0$ denotes a matrix formed by stacked copies of the row vector $[B_0(\mathbf{r}_1) \ldots B_0(\mathbf{r}_m)]$, one per time point, $\mathbf{g}_0$ is a column vector with the discretized zeroth-order field component, and $\mathbf{G} = [\mathbf{g}_1, \mathbf{g}_2, \mathbf{g}_3]$ contains the discretized gradient time courses.

To prevent confound by slow field perturbations, which will not generally permit mere first-order expansion, the discrete data is filtered by an operator $\mathbf{F}$ that eliminates the DC and low-frequency components represented by $\mathbf{B}_0$. In addition, $\mathbf{F}$ can be used to suppress other

frequency bands that could be affected by higher-order perturbation or for spectral selection when certain frequencies are explicitly used for position encoding such as with gradient tones[24]. Application of the filter gives

$$\mathbf{FD\Phi}_{\mathrm{H}} = \gamma_{\mathrm{H}}\mathbf{Fg}_0\mathbf{1}_m + \gamma_{\mathrm{H}}\mathbf{FGR}_{\mathrm{H}} \,. \qquad [3.5]$$

Least-squares solving for $\mathbf{R}_{\mathrm{H}}$ yields

$$\mathbf{R}_{\mathrm{H}} = (\mathbf{FG})^{+}\mathbf{F}(\gamma_{\mathrm{H}}^{-1}\mathbf{D\Phi}_{\mathrm{H}} - \mathbf{g}_0\mathbf{1}_m) \qquad [3.6]$$

where the superscript + denotes the Moore-Penrose pseudoinverse.

To obtain $\mathbf{R}_{\mathrm{H}}$ via Eq. [3.6], $\mathbf{FG}$ and $\mathbf{Fg}_0$ must first be derived from the lab-frame marker data. To this end, Eq. 3.3a is equally discretized and subject to the same filter, yielding

$$\mathbf{FD\Phi}_{\mathrm{L}} = \gamma_{\mathrm{L}}\mathbf{Fg}_0\mathbf{1}_n + \gamma_{\mathrm{L}}\mathbf{FGR}_{\mathrm{L}}, \qquad [3.7]$$

which can be rearranged as

$$\mathbf{FD\Phi}_{\mathrm{L}} = \gamma_{\mathrm{L}}\mathbf{F}[\mathbf{g}_0|\mathbf{G}]\begin{pmatrix}\mathbf{1}_n\\ \mathbf{R}_{\mathrm{L}}\end{pmatrix}. \qquad [3.8]$$

Least-squares solving for $\mathbf{F}[\mathbf{g}_0|\mathbf{G}]$ yields

$$\mathbf{F}[\mathbf{g_0}|\,\mathbf{G}] = \gamma_{\mathrm{L}}^{-1}\mathbf{FD\Phi}_{\mathrm{L}}\begin{pmatrix}\mathbf{1}_n\\ \mathbf{R}_{\mathrm{L}}\end{pmatrix}^{+}. \qquad [3.9]$$

To perform this calculation, the positions of the lab-frame markers, $\mathbf{R}_{\mathrm{L}}$, need to be known. In this study, they were determined by measurement of FID frequency shift under constant gradients on each axis.

Carrying out Eq. [3.6] yields the head marker positions. Changes in these positions relative to the beginning of the scan are interpreted as

reflecting rigid-body motion. The related coordinate transform is described by a rotation matrix and a translation vector, which are calculated as described by Umeyama[47] and form the typical input for motion correction.

3.2.3 Gradient tones

For robust, high-frequency position encoding, sinusoidal gradient tones were introduced in the imaging sequences used. Unlike the original implementation of this approach[24], the tones were superimposed not on readout gradients but on spoiler gradients[50] (Figure 3.2). Position encoding during spoiling requires high-sensitivity markers of suitably small droplet diameter. In turn, it avoids alteration of readout trajectories and thus the need for any changes at the level of image reconstruction. The operator $\mathbf{F}$ was chosen such as to not only suppress DC and low frequencies but select the tone frequencies.

3.2.4 Hardware

All experiments were performed on a 7T Philips Achieva system (Philips Healthcare, Best, The Netherlands), equipped with a 32-channel head receive array (Nova Medical, Wilmington, Massachusetts, USA). All NMR markers[31] were based on ^{19}F and operated with a custom console and receiver[33]. 16 stationary markers (T1 = 86 ms, diameter = 0.8 mm) were mounted with the help of a laser-sintered support placed between the RF transmitter and the receiver array (Figure 3.3). Four head-frame markers (T1 = 2.1 ms, diameter = 1.3 mm) were mounted on a 3D-printed headset (Figure 3.3).

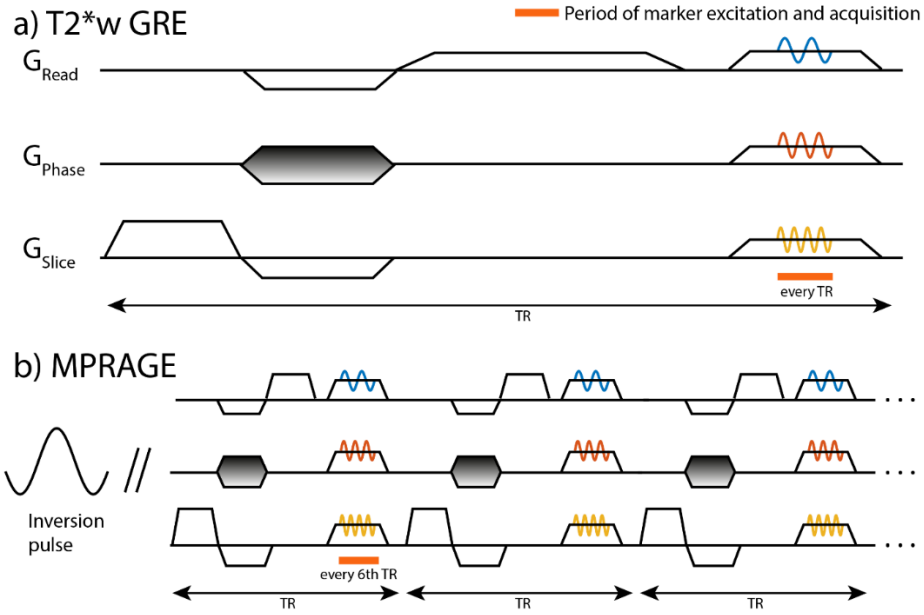

Figure 3.2: Sequence diagrams of the sequences used in this work, demonstrating the superposition of sinusoidal gradients for marker tracking. They were superimposed on the spoiler gradients in each TR of the T2-weighted GRE sequence and in each TR of the readout train following the inversion period in the MPRAGE sequence. Marker excitation and signal acquisition was performed every TR in the T2*-weighted sequence and every sixth TR in the MPRAGE sequence.*

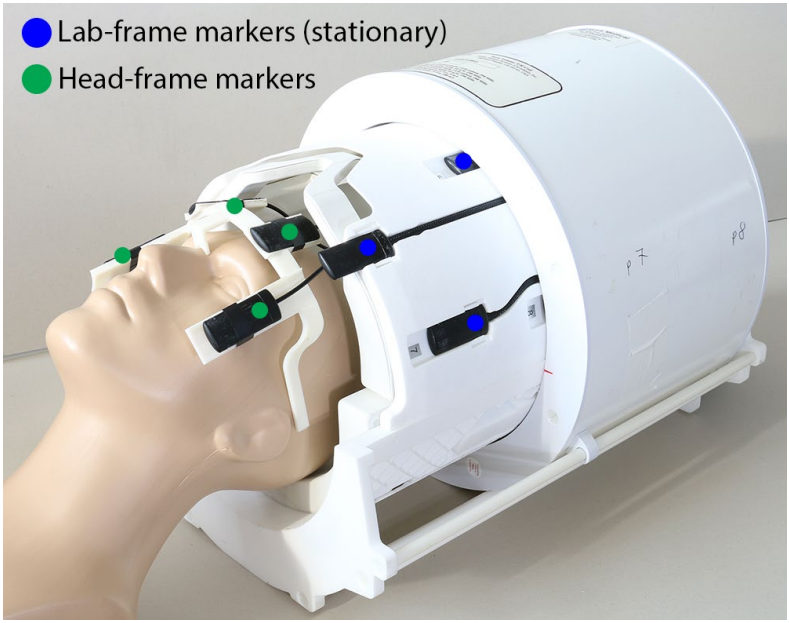

Figure 3.3: The stationary markers are positioned within a laser-sintered frame inserted between the receiver and transmit arrays. For in vivo imaging, markers were attached to a 3D-printed headset worn by the subject.

3.2.5 Prospective motion correction

All processing of marker signals was performed on the custom console. Based on resulting rigid-body motion parameters, geometry updates were sent via TCP connection to a run-time interface of the MRI system[46].

3.2.6 Sequences and timing

Experiments were carried out using a 2D T2*-weighted GRE sequence (resolution: 0.3 mm x 0.3 mm x 1.2 mm, FOV: 231 mm x 231 mm x 30 mm, TE: 25 ms, TR: 41.7 ms, flip angle: 45°, slices: 18, flow compensation, 2 averages, duration: 19:15 min) and a 3D MPRAGE

sequence (resolution: 0.75 mm³ isotropic, FOV: 220 mm x 220 mm x 150 mm, TE: 2.9 ms, TR: 7 ms, flip angle: 7°, TI: 1200 ms, duration: 27:58 min).

In the T2*-weighted sequence, sinusoidal gradient tones of 1 ms duration were superimposed on the spoiler gradients (frequencies: 2 kHz, 3 kHz, 4 kHz, amplitude: 7 mT/m). Marker excitation and acquisition were performed in every TR of the sequence (Figure 3.2a).

In the MPRAGE sequence, tones of 0.6 ms duration were superimposed on the spoiler gradients of the readout train (frequencies and amplitudes: 1.68 kHz / 7 mT/m, 3.36 kHz / 7 mT/m, 5.04 kHz / 6 mT/m). Marker excitation and acquisition were performed in every sixth TR, resulting in a tracking interval of 42 ms.

3.2.7 Assessment of tracking performance and comparison with calibration-based tracking

To evaluate the tracking precision and to further explore the performance of the presented method, motion tracking was first performed in a static setting, where the markers were rigidly attached in a geometry similar to their positioning on the headset. Resulting data was analyzed with regard to systematic tracking error, the role of magnetic field noise in the scanner bore, propagation of detection noise incurred by field tracking, and noise propagation upon the computation of rigid-body parameters.

*3.2.7.1 T2*w sequence*

Real-time field tracking was juxtaposed with three options for pre-calibration. The first, most basic calibration consisted in averaging $\mathbf{F}[\mathbf{g_0}|\,\mathbf{G}]$ over the first 200 TR of the sequence, assuming that spectral

field content at the tone frequencies is immune to gradient steps related to phase encoding. This relatively convenient and fast approach is most commonly used to-date. In the second mode, full calibration was performed by measurement over the entire scan duration, yielding an individual calibration matrix $\mathbf{F}[\mathbf{g_0}|\,\mathbf{G}]$ for every TR. Both of these conventional calibrations were implemented with a setup as described in Ref. (24), using four head-frame markers arranged as a tetrahedron of roughly 10 cm diameter, mounted inside the receiver array (in-coil markers). Thirdly, full calibration was repeated with the same setup as used for real-time field tracking, i.e., with lab-frame markers mounted around the receiver array (on-coil markers).

Time series of rigid-body parameters in the absence of motion were reconstructed using all four approaches and compared with respect to systematic error and tracking precision. To quantify systematic drift, a moving-average filter (width = 10 sec) was used and the peak-to-peak range of the resulting curves was computed. Precision was assessed as the standard deviation after subtraction of the filter output.

3.2.7.2 MPRAGE sequence

In the MPRAGE sequence, 3D encoding is associated with a second phase-encoding loop. Potential effects of this additional gradient variation were studied by comparing real-time field tracking with basic calibration. The latter was mimicked in this case by taking the real-time field tracking result obtained in the first TR.

Again, time series of rigid-body parameters in the absence of motion were reconstructed using both approaches. The range of potential fast modulations caused by the inner phase-encoding loop was estimated by averaging over the peak-to-peak values obtained for each cycle of this

loop and the modulations were subsequently removed using a band stop filter. Remaining slow drifts and tracking precision were assessed as in the 2D case.

3.2.7.3 Assessment of consistency differences

Tracking accuracy cannot be straightforwardly determined in the absence of known ground truth or a gold-standard measurement technique. Instead, accuracy was estimated in a separate experiment studying the consistency between marker positions obtained with high-frequency tones and with static gradients. Comparing these two options effectively tests the validity of the signal model [3.3a,b] and the propagation of model error into tracking results. In particular, it should reveal whether real-time field tracking incurs greater error than conventional calibration by relying on a probe setup of larger diameter and thus greater sensitivity to higher-order fields not captured by the first-order model.

In this experiment, tones-based tracking was performed in a static setup with a sequence consisting exclusively of repeated intervals of concurrent sinusoidal gradients (frequencies: 2 kHz, 3 kHz, 4 kHz, amplitude: 7 mT/m, duration: 1 ms, 500 repetitions). Marker positions were determined once based on calibration and once based on real-time tracking. The temporal means of the resulting coordinate time series were then compared with reference coordinates obtained via static gradients.

3.2.8 Effect of thermal drift on tracking stability

To study the robustness of real-time field tracking in the presence of system drift, four NMR markers mounted statically inside the receiver

array were tracked during an EPI scan intended to cause thermal changes in gradient system response[61]. Gradient tones (frequencies: 2 kHz, 3 kHz, 4 kHz, amplitude: 7 mT/m, duration: 1 ms) inserted in an interval without other gradient activity were used to encode the marker positions[50]. The oscillation frequencies did not coincide with mechanical resonance frequencies of the gradient coils[52]. Calibration data was collected in the cold state, using the tetrahedral four-probe setup. Time series of rigid-body parameters were computed based on real-time field tracking and based on calibration. Drift and precision were determined in the same way as described above for the T2*-weighted sequence. Concurrently with EPI and motion tracking, a temperature sensor mounted on the gradient coils was read out every 2 seconds. For every time step, real-time field tracking yielded a matrix $\mathbf{G}$ containing the determined gradient dynamics, so that the magnitudes of the Fourier components associated with the corresponding tone frequencies and axes could be used to inspect the effect of system heating.

3.2.9 In vivo imaging

For in vivo validation, challenging scan scenarios characterized by high spatial resolution and long scan duration were chosen. A healthy volunteer was scanned according to the applicable ethics regulation and instructed to hold as still as possible throughout. Both the T2*-weighted and the MPRAGE sequence were carried out with and without PMC. In the case of T2*-weighted imaging without PMC, the two acquired averages were realigned using a routine provided in Matlab (MathWorks, Natick, MA, USA). For quantitative comparison, image entropy was calculated. Entropy relates to sharpness and has previously been used as a guiding criterion in retrospective correction of motion artefacts[9].

3.3 Results

3.3.1 Assessment of tracking performance and comparison with calibration-based tracking

*3.3.1.1 T2*w sequence*

The resulting rigid-body parameter time series are shown in Figure 3.4 along with drift and precision values. Basic calibration resulted in systematic error of more than 0.5 mm in RL translation (Figure 3.4a). The RL axis is the phase encoding direction, indicating that the drift is a consequence of gradient stepping. The absence of similar patterns in the rotation results illustrates that this drift relates to purely translational drifts also in the individual marker positions. According to Eq. 3.6 such an error can be caused by changes in $\mathbf{g}_0$, which includes zeroth-order fields but also potential contamination from higher-order contributions not accounted for by the field expansion. This is likely due to eddy-currents and concomitant fields that change with gradient stepping on the phase encoding axis. Smaller variation occurs around the middle of the time series where $k_y = 0$. This is most likely related to subtle differences in amplifier behavior for different gradient polarities, which basic calibration does not capture. These systematic errors are virtually eliminated by the three other approaches (Figure 3.4b-d), most so with the real-time field tracking, which reduced the drifts to under 40 µm and 30 mdeg.

Since all measurements rely on the same marker encoding strategy, differences in tracking precision reflect primarily different propagation and superposition of detection noise of the markers and noise present in the magnetic field that they probe. While basic calibration assumes fixed $\mathbf{FG}$ and $\mathbf{Fg}_0$ for all TR, the other approaches are subject to detection

noise in the variable $\mathbf{FG}$ and $\mathbf{Fg}_0$, which propagates into the motion parameters. In the case of full calibration with in-coil markers (Figure 3.4b), this mechanism deteriorates precision by more than 50% relative to basic calibration. In contrast, full calibration with on-coil markers (Figure 3.4c) resulted in precision comparable to that obtained with basic calibration. This is a consequence of the larger number of contributing NMR markers and their positions at a greater distance from the isocenter where gradient fields are stronger in absolute terms and hence give rise to higher SNR of phase time courses. The tracking precision is further improved by real-time field tracking (Figure 3.4d). This indicates that it captures some degree of field noise that calibration necessarily misses. Presumably for the reason, the precision thus achieved is also better than with basic calibration, by up to 10%. The obtained tracking precision of below 25 µm is appropriate with respect to the targeted imaging resolution of 0.3 mm in-plane.

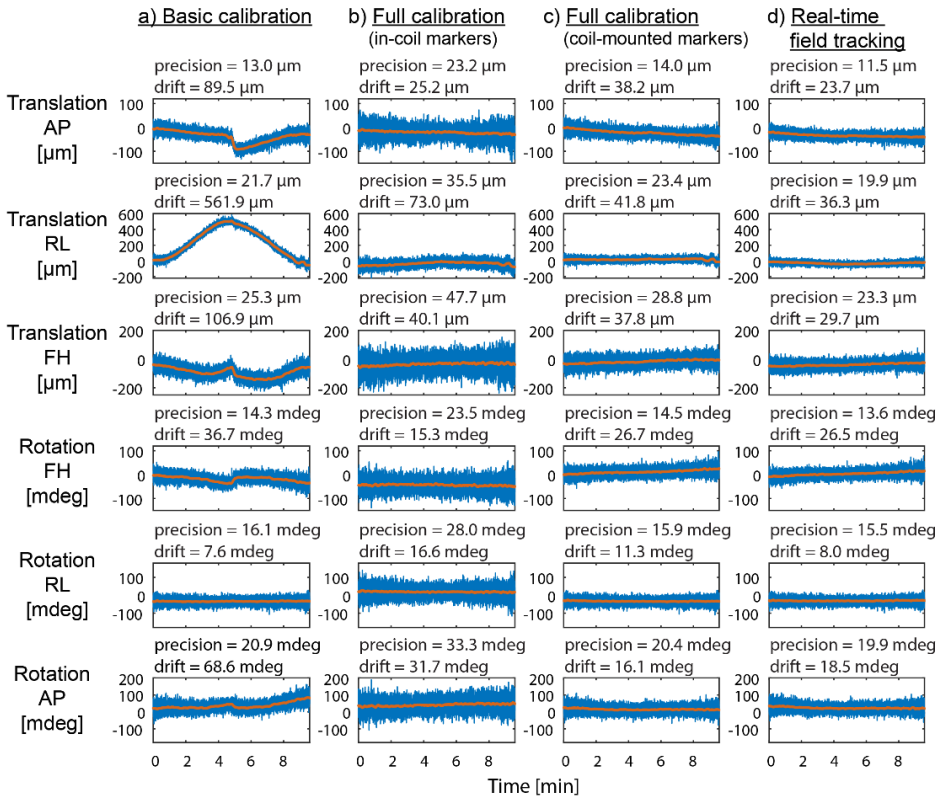

Figure 3.4: Comparison of rigid-body parameters obtained in a static setting using different calibration-based approaches (a-c) and the real-time field tracking approach (d). Systematic drifts (red) are determined using a moving-average filter and quantified via their peak-to-peak value. The precision is obtained by computing the standard deviation of the difference between the filter output and the time series. The real-time field tracking approach yields the lowest drifts and best precision values.

3.3.1.2 MPRAGE case

Figure 3.5 shows the rigid-body time series along with the filtered curves resulting from applying a moving average filter to the rigid-body time

series after removal of high-frequency modulations. These high-frequency modulations caused by the inner phase encoding loop are particularly prominent in the case where no real-time field tracking was applied, with amplitudes exceeding 0.5 mm, as seen in the zoomed view (Figure 3.5a, second row). Real-time field tracking, however, reduced these excursions to below 50 µm (Figure 3.5b, second row) and significant reductions in the range of these high-frequency modulations were observed in all coordinates. Long-term drifts were either significantly improved by real-time field tracking or remained at a similar level. Precision was 10-20% better with real-time field tracking, achieving values of below 35 µm and below 37 mdeg, respectively. This can be attributed in part to the incorporation of field noise as observed in the T2*w case, but may also be slightly emphasized by residual imperfections in the removal of the strong high-frequency oscillations. The obtained tracking precision is sufficient to carry out imaging at a resolution of 0.75 mm.

3.3.1.3 Consistency of the signal model

The discrepancies between tracking based on tones and marker coordinates obtained with static gradients are listed in Table 3.1 (supplementary material). They range up to a maximum of 225 µm, which occurred with calibration, while discrepancies reached 182 µm with real-time tracking. The mean discrepancies across all markers were in the range of 78 µm to 133 µm, with only minor differences between the two approaches.

	Calibration			Real-time field tracking		
	X	Y	Z	X	Y	Z
Marker 1	157	147	-129	99	-111	116
Marker 2	79	156	10	47	-61	63
Marker 3	225	13	-157	182	-115	66
Marker 4	72	-32	-93	74	23	-90
Mean absolute value	133	87	97	100	78	84

Table 3.1 (supplementary material): Discrepancies between marker localization based on tones and static gradients shown for all markers along with the mean absolute value for each coordinate. Tones-based localization was performed using either calibration or real-time field tracking. The comparison revealed only minor differences between the two approaches.

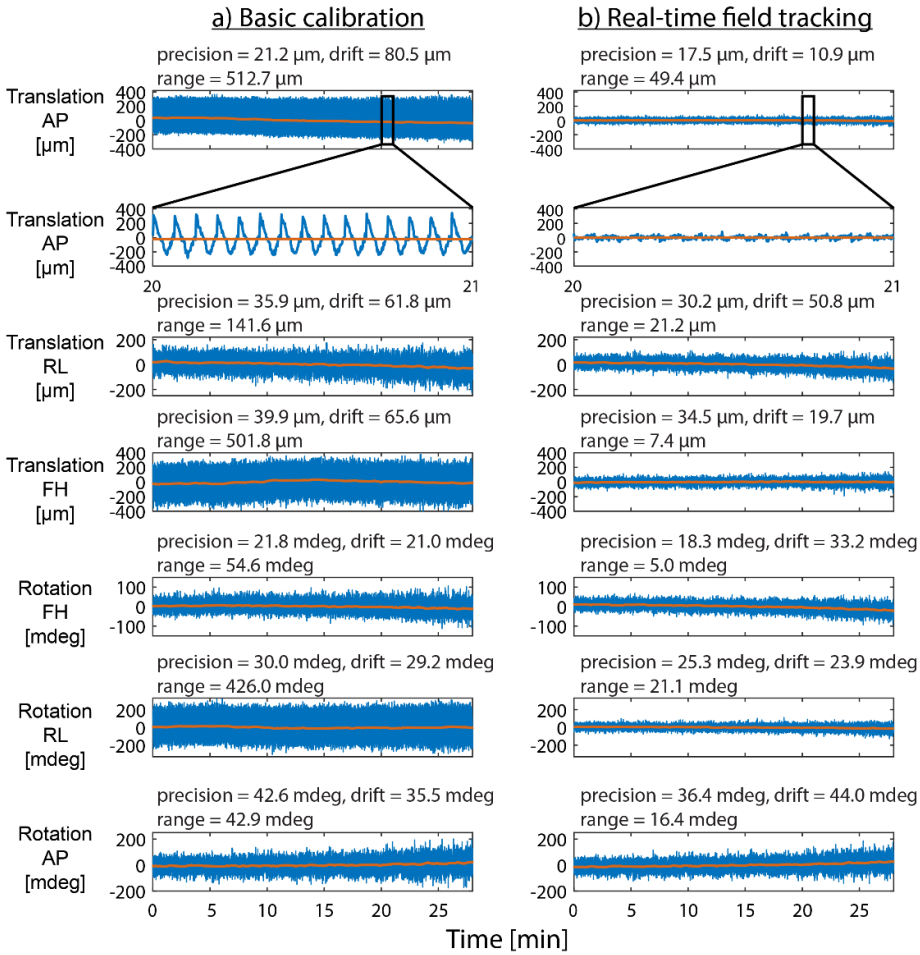

Figure 3.5: Comparison of rigid-body parameters obtained in a static setting during the execution of the MPRAGE sequence. In the case of a basic calibration, the inner phase encoding loop caused distinct high-frequency modulations with up to 0.5 mm in range (second row: close-up view) which were significantly reduced by real-time field tracking.

Long-term drifts (red) are also substantially reduced by real-time field tracking.

3.3.2 Effect of thermal drift on tracking stability

An increase of gradient temperature by approximately 22 degrees was recorded over about nine minutes of EPI scanning (Figure 3.6a). The time courses of the Fourier components belonging to the respective coil and tone frequency used for tracking exhibit a drift of about 0.2% in the magnitudes at 2 kHz and 3 kHz on the x and y coil, respectively (Figure 3.6b). The magnitude of the 4 kHz gradient oscillation on the z axis drifted by about 0.1 %. The difference is likely due to differences between the gradient coils with respect to energy dissipation and cooling.

In the calibration case, the resulting rigid-body tracking parameters suffer from pronounced temperature-induced drifts, exceeding 0.1 mm (Figure 3.6c). The peak-to-peak values indicate that, in five out of six parameters, real-time field tracking reduced the drift by a factor of five to ten and in the remaining parameter (translation in y) still by a factor of two, thereby essentially eliminating temperature-induced drift (Figure 3.6d). The tracking precision is very similar for both cases.

3.3.3 T2* imaging

The head tracking data recorded during the T2*-weighted sequence shows a similar extent of motion during the scans with and without PMC. The most pronounced motion is slow rotation about the back of the head, amounting to rotation about the FH axis by just below two degrees along with RL translation by 2-3 mm (Figure 3.7). In the uncorrected case, this caused substantial image degradation in a single acquisition (Figure

3.8a) and with straightforward averaging (Figure 3.8b). Realignment prior to averaging had a mitigating effect on motion artefacts, but did still incur visible loss of detail (Figure 3.8c). Motion correction resulted in clearly higher image quality with sharper depiction of small structures such as cortical veins (Figure 3.8d). This is the result of both better image quality of individual acquisitions and geometric consistency between the two averages, which is also a consequence of PMC. Across the dataset, PMC reduced image entropy by 1.3 % +/- 0.3 % relative to using just realignment instead.

3.3.4 MPRAGE imaging

Significant unintentional head motion of up to 3 mm occurred over the extended duration of the MPRAGE scan of almost 30 minutes (Figure 3.9). Note that local tissue displacement may even be larger, particularly in the frontal lobe region. Clear motion artefacts are visible in the uncorrected case (Figure 3.10), particularly blurring at gray-white matter boundaries. PMC again proved effective, resulting in improved image quality throughout the 3D data set, both in posterior and anterior regions (Figure 3.10, transversal and sagittal slices). The reduction of mean image entropy by PMC amounted to 3.1 % +/- 2.4 %.

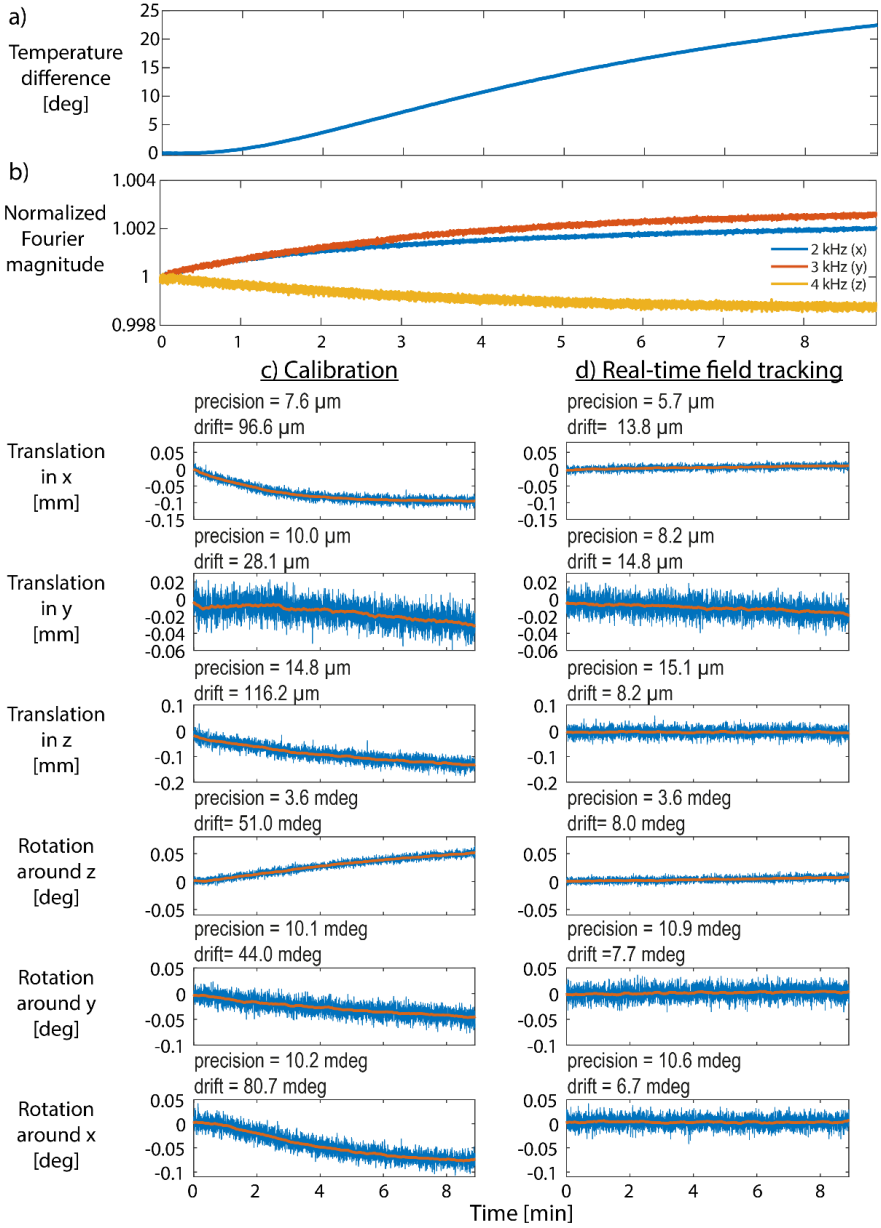
a)
Temperature difference [deg]
b)
Normalized Fourier magnitude
2 kHz (x)
3 kHz (y)
4 kHz (z)
c) Calibration
d) Real-time field tracking
Translation in x [mm]
precision = 7.6 µm
drift= 96.6 µm
precision = 5.7 µm
drift= 13.8 µm
Translation in y [mm]
precision = 10.0 µm
drift = 28.1 µm
precision = 8.2 µm
drift = 14.8 µm
Translation in z [mm]
precision = 14.8 µm
drift = 116.2 µm
precision = 15.1 µm
drift = 8.2 µm
Rotation around z [deg]
precision = 3.6 mdeg
drift= 51.0 mdeg
precision = 3.6 mdeg
drift= 8.0 mdeg
Rotation around y [deg]
precision = 10.1 mdeg
drift= 44.0 mdeg
precision = 10.9 mdeg
drift =7.7 mdeg
Rotation around x [deg]
precision = 10.2 mdeg
drift = 80.7 mdeg
precision = 10.6 mdeg
drift = 6.7 mdeg
Time [min]

Figure 3.6: a) Recorded temperature increase during the execution of an EPI sequence. b) Time evolution of the Fourier magnitudes associated with the respective gradient coil and tone frequency. A temperature-induced drift of 0.1-0.2 % is visible. c) The rigid-body parameters obtained using the basic calibration exhibit a drift of up to about 100 µm. d) Rigid-body parameters reconstructed with real-time field tracking demonstrate high tracking stability even in the presence of thermal system drift.

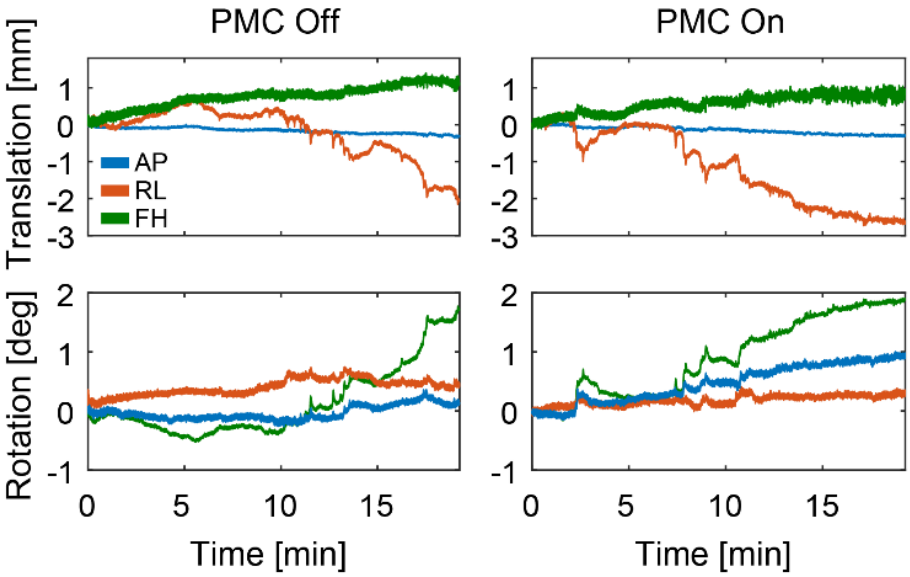

Figure 3.7: Rigid-body head tracking parameters obtained during the T2 weighted scan with and without PMC. They are comparable in intensity and during both scans a slight head rotation about the FH axis occurred.*

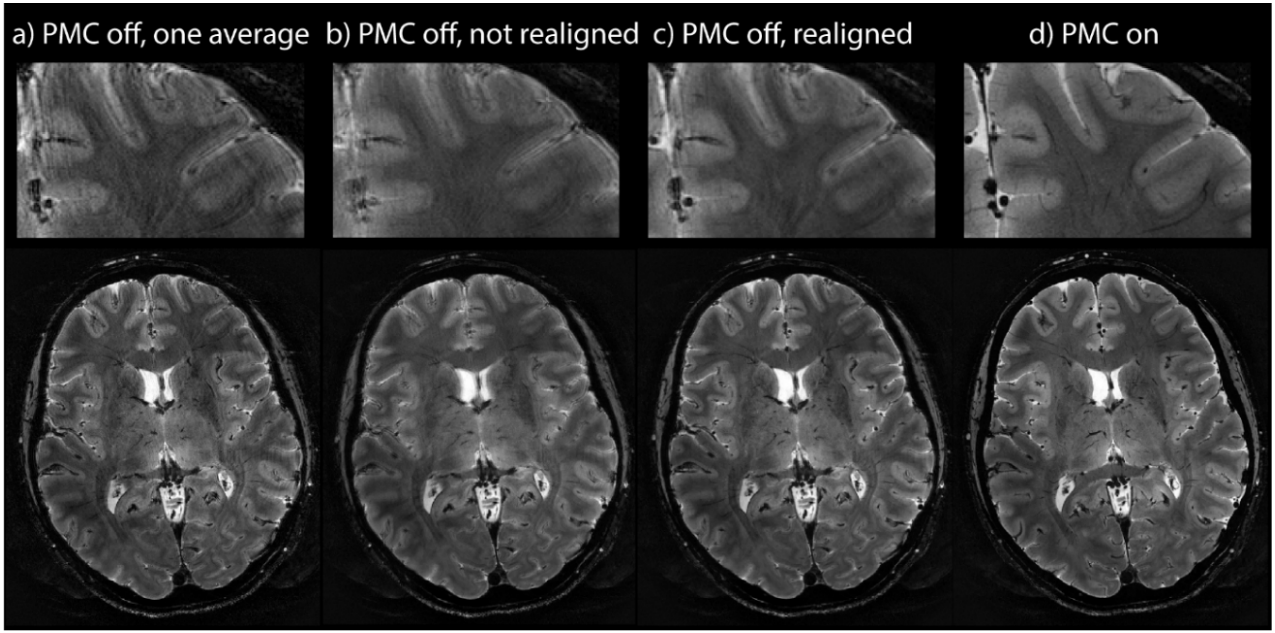

Figure 3.8: In vivo T2-weighted imaging. a) A single average without PMC suffers from strong motion artefacts resulting from head motion as presented in Figure 3.7. b) Averaging of non-realigned slices acquired without PMC results in strongly blurred image quality. c) Realignment and averaging increases robustness to motion artefacts, but a significant loss of detail remains. d) High image quality is obtained in the motion corrected case, with a sharp depiction of vessels and tiny cortical structures.*

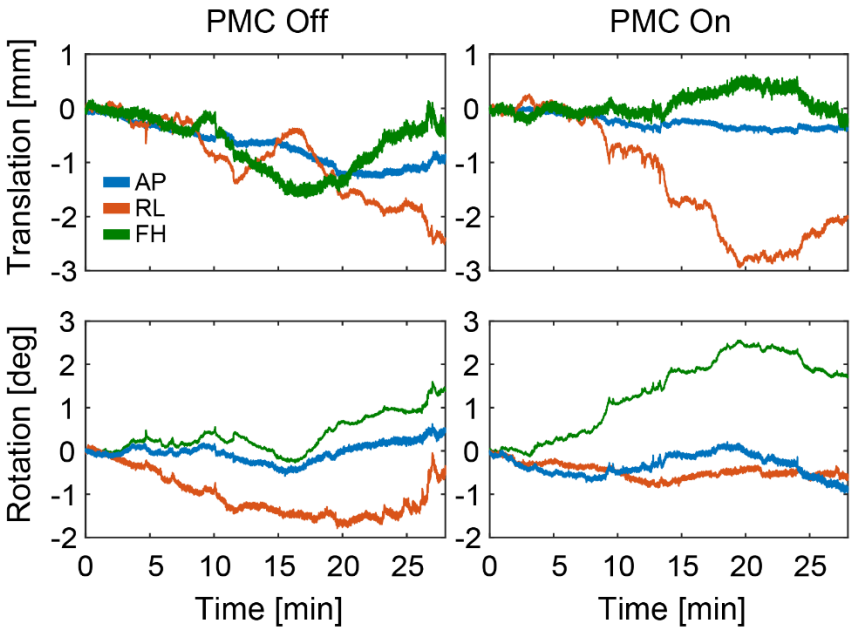

Figure 3.9: Recorded head tracking parameters during the MPRAGE scans with and without PMC. Unintentional head motion of up to 3 mm and 2-3 degrees occurred and was mainly comprised of a slow head rotation about the FH axis and a slight pitch movement about the RL axis.

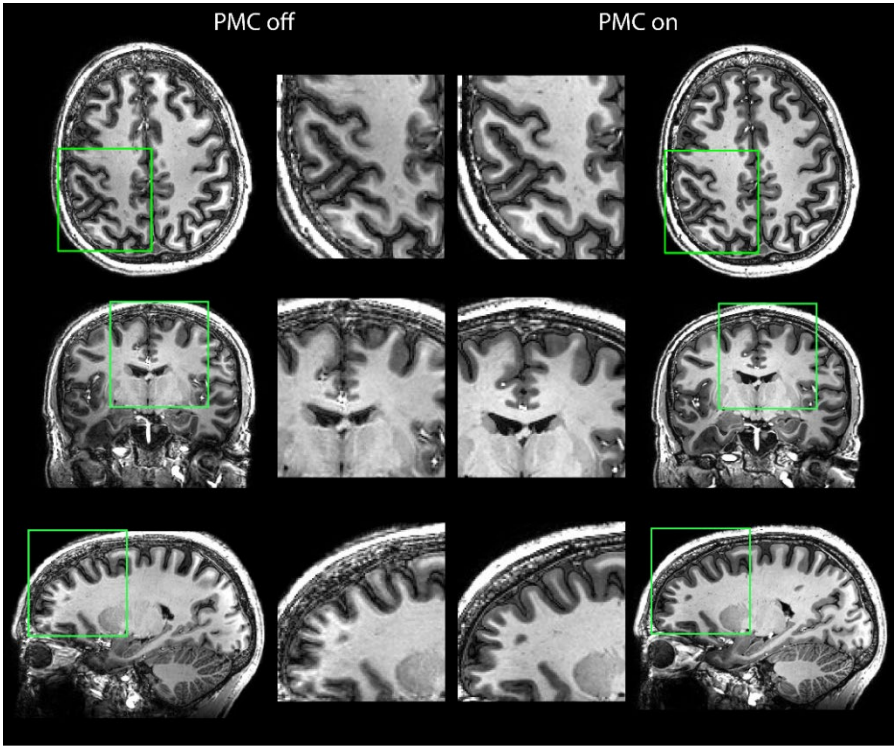

Figure 3.10: Representative transversal, sagittal and coronal slices of the MPRAGE scan with and without PMC. The uncorrected images (left) suffer from strong blurring, particularly at the gray-white matter boundaries. PMC consistently provides a sharp image quality and achieves a clear depiction of small structures such as vessels or the meninges.

3.4 Discussion

According to the preceding results, real-time field measurement in the laboratory frame obviates time-consuming calibration in NMR marker tracking without compromising tracking performance. It has even been found to outperform calibration-based approaches in terms of tracking precision and robustness against systematic error. Basic calibration

incurred systematic tracking error related to gradient variation between TR intervals, particularly to the step changes in phase encoding gradients and spoilers. Real-time field tracking eliminated these errors by capturing the relevant field dynamics more fully. Gradient stepping and associated changes in eddy currents and concomitant fields induced the largest errors (0.5 mm) in the case of a basic calibration, which appeared to scale with the range of gradient stepping. Full calibration reduced such systematic errors but is very time consuming and would need to be repeated upon most changes of sequence parameters and geometry. In addition to solving this issue, real-time field tracking also removed drifts in motion parameters due to changes in hardware temperature. This is valuable not only for gradient-intensive scans but also for other exams when performed while the system cools down after such a scan.

The tracking precision achieved in this study was amply sufficient with respect to the targeted imaging resolutions, at 10-25 µm and 10-20 mdeg in the T2*-weighted case and 17-35 µm and 18-37 mdeg in the MPRAGE case. Relative to basic calibration, the tracking precision was not impaired by additional detection noise incurred by real-time field measurements. The obtained results indicate that the additional detection noise was largely or even more than compensated for by the fact that real-time field measurements capture field noise, which is wrongly reflected in pre-calibration. Additional precision could be gained by accounting for decreasing SNR due to marker dephasing via a weighted least-squares solution. This may improve precision particularly when significant marker dephasing occurs, e.g., during spoiler gradients.

The implementation reported in this study relied entirely on a first-order field model, which led to successful motion correction. Limiting the model to first order is convenient because it renders the calculation of head marker coordinates a linear and thus numerically efficient procedure that is readily feasible in the real-time framework. The first-order model is most justified for the head-frame markers because of their proximity to the isocenter. It is worth noting that the readings from the lab-frame markers, which are at greater radii, could also be interpreted in terms of a higher-order model, which will yield more accurate estimates of the first-order components. This option would still be very benign numerically because fitting a higher-order field model is still a linear problem as opposed to computing marker coordinates within such a model. The consistency experiment performed in the present study showed that the chosen first-order field expansion was adequate since marker localization with real-time field tracking did not result in an accuracy trade-off relative to traditional calibration performed closer to the isocenter.

The employed headset provided marker placement close to the head and although head motion was significant with respect to image resolution, it was in the range of millimeters and thus small relative to the linear range of the gradient system. For larger marker displacement and when markers are positioned further from the isocenter, gradient non-linearity correction could be necessary, as recently shown for NMR marker tracking using a motion stage[62].

In the present study, sinusoidal gradient tones were used for marker encoding. Superposition of sinusoidal gradients on parts of the sequence other than the readout section reconciles zero sequence

overhead with unaltered image reconstruction on clinical equipment. When sequence changes are not possible or desirable, NMR marker tracking can also rely on the gradient elements already present in any given sequence[27]. This option, too, requires accurate knowledge of actual gradient dynamics and will likewise benefit from simultaneous field tracking. To this end, the formal framework used in the present work can be readily expanded by the concept of merging multiple signal snippets in one system of equations[27]. As discussed in Ref. (27), this approach demands very short T1 and T2 of head markers, a requirement that will equally apply to lab-frame counterparts.

The relaxation time T1 of the lab-frame markers employed in the present study was larger than that of the head-frame markers, which required to limit marker signal acquisition to every sixth TR in the MPRAGE sequence. This resulted in a tracking rate of about 23 Hz, which is sufficient to capture the dynamics of head motion (26). However, head-frame markers and lab-frame markers can generally have the same specifications in terms of droplet diameter and relaxation times.

The chief purpose of frequency-selective signal processing is to filter out confounding field dynamics, particularly of physiological origin. Doing so is most critical with pre-calibration because field perturbations related to physiology are not reproducible. Real-time field tracking could be argued to obviate this issue by recording lab-frame and head-frame marker data at the same time, effectively handling any field perturbations as part of the net encoding field. On this basis, it is tempting to involve low-frequency fields in the data analysis, which could improve the tracking precision by deploying additional encoding power. However, this approach will incur systematic error in the presence of low-frequency

fields that do not conform to the chosen spatial field expansion. One source of such field variations is head motion itself because it alters the magnetic field created by the head's own magnetic susceptibility. Emanating from sources within the volume of interest, this field contribution can be neither fully detected with markers outside the head nor properly expanded with few basis functions. Slowly varying field not conforming to the field expansion can also occur due to temperature drift in the NMR markers, which gives rise to extremely local field changes due to temperature dependence of magnetic susceptibility and chemical shift.

In summary, real-time field measurement in the laboratory frame advances NMR marker tracking by eliminating the need for calibration and improving tracking accuracy. Doing away with calibration removes a key obstacle to routine use of NMR-based motion detection and correction, which is now feasible not only without sequence alteration but also without scan time overhead.

Chapter 4

Simultaneous prospective motion correction and feedback field control

Parts of this work were published in:

Vionnet L.*, Aranovitch A.*, Duerst Y., Haeberlin M., Dietrich B.E., Gross S., Kasper L., Schmid T., Pruessmann K.P. Simultaneous prospective motion correction and feedback field control: T2* weighted imaging at high field. *ISMRM 25th Annual Meeting*, Honolulu, HI, USA, 2017.

*authors with equal contribution

Manuscript in preparation

4.1 Introduction

Gradient-recalled echo (GRE) sequences count among the basic and most widely used MRI techniques. They yield particularly rich contrast and detail when performed with long echo time for T2* weighting. In addition to T2 decay, T2* contrast reflects spatial variation of the static magnetic field, including distortion by susceptibility effects. Microscopic field non-uniformity causes intra-voxel dephasing and thus affects the magnitude of image values while longer-range field variation is encoded in the phase of T2*-weighted images. Using these properties, the T2*-weighted data can be used to derive further types of contrasts. In susceptibility-weighted imaging (SWI), the two types of information are fused by real-valued combination of image magnitude and phase[63,64] while quantitative susceptibility mapping (QSM) relies on the image phase to reconstruct the distribution of magnetic susceptibility in the sample[65,66].

T2* weighting is most widely used in neuroimaging, both clinically and for research. Magnitude data are used, e.g., to study imaging small lesions, iron deposition, microbleeds, tumors[67], and intracranial infection[68]. The ability of SWI to reveal microbleeds and differentiate between hemorrhagic lesions and calcifications makes it a method of choice in the fields of brain injury[69–78], seizures[79–84], infectious brain diseases such as abcesses[85–87] and other intracranial infections[88], brain neoplasms[89–92], stroke[93–99], multiple sclerosis[100], and vascular malformation[101–105]. QSM is frequently used to probe certain biological markers and to study inflammatory diseases that involve iron accumulation. These include Alzheimer's Disease[106–108], Parkinson Disease[109,110], Huntington Disease[106,111], and Multiple Sclerosis[112,113].

QSM also enables differentiation between microbleeds[114] and calcifications in the brain[115–117] and in tumors[118,119].

Contrast related to susceptibility effects scales with B_0 and is rich in structural detail. Therefore, T2*-weighted imaging is particularly promising at high field, which both boosts T2* contrast and enhances baseline sensitivity in favor of spatial resolution. However, boosting sensitivity to susceptibility effects and pushing resolution come with inherent challenges. In combination with motion, susceptibility effects cause field fluctuations and related artefacts when unaddressed[2,3,120,121]. In brain imaging, this problem arises particularly from breathing motion and movement of shoulders and arms. Besides moving body parts, field fluctuation and drift can also arise from hardware imperfections and thermal effects[52,122–129]. High-resolution brain imaging, on the other hand, is particularly vulnerable to motion of the head itself. The long scan times involved increase the range of motion that occurs while small voxel size exacerbates its impact in terms of artefacts and resolution loss.

The first challenge, field fluctuation, is often addressed by retrospective data correction based on signal phase[130] or dedicated navigator acquisition[2,131–134], detecting only global field changes or also first-order terms[2,15,60,135]. The navigator approach has the advantage that it does not require additional hardware. However, it tends to increase the overall scan time and requires added care in sequence design to prevent detrimental spin-history effects. Retrospective correction of field fluctuation has also been demonstrated based on field sensing with NMR probes[31]. This approach permits higher-order correction[136,137] and avoids sequence overhead, albeit at the expense of added

instrumentation. The main limitation of retrospective approaches is that they can recover image information only as far as it is still encoded in the perturbed data. For instance, they cannot undo through-plane dephasing or potential k-space undersampling upon bias in linear field terms.

These problems are overcome by prospective field correction. Online correction for global field changes is a long-standing practice in laboratory NMR and known as frequency locking[138,139]. In MRI, prospective correction of zeroth-order field fluctuation was first based on navigator echoes[125]. Later, real-time correction of breathing effects up to second order in space was accomplished with readings from a breathing belt and preceding calibration[121]. Prospective correction has also been based on NMR probes for field detection, enabling run-time B_0 update[140] as well as spatiotemporal control using dynamic actuation of gradient and shim fields[3]. Besides avoiding information loss, real-time field control also obviates the need for specific correction efforts at the reconstruction level, which can be computationally demanding. It has been found to be effective countering respiratory field perturbations in T2*-weighted imaging, T2* mapping and QSM at high field[141–143].

The second challenge, head motion, can also be addressed retrospectively as well as prospectively. Retrospective approaches counter motion effects by data correction and means of image reconstruction once data acquisition is completed[9,38]. Similar to the case of field fluctuation, this strategy is limited by motion effects that cannot be reversed at the data level, including misalignment of excited volumes and local undersampling of k-space. In contrast, prospective motion

correction performs continuous updates of the sequence geometry based on motion tracking during the scan. Tracking strategies fall broadly into three categories: navigators, optical means, and NMR markers. Navigators collect spatially encoded MR signal from the head itself, typically in the form of low resolution images[17,43] or selected parts of k-space[14,15]. As a consequence, they generally require a certain degree of sequence alteration and scan time overhead. Optical methods use cameras to track head-mounted markers[18,20] or the head itself[22,42]. They come at no expense in terms of scan time but require a robust line of sight, which can be a challenge, especially through dense receiver arrays. Head-mounted NMR markers, finally, capture motion by observation of gradient fields, which permeate the setup virtually unhindered[24,26,31,144–147]. Localization of NMR markers has been achieved with dedicated sequence modules interleaved with imaging[26], superimposed high-frequency gradient tones[24], and also with unaltered imaging sequences[27].

As argued initially, certain imaging scenarios call for combined field and motion correction. This goal has been pursued in only a few contributions so far, relying mostly on navigator strategies. Retrospective correction of global B_0 change and head motion was reported in Ref. (60) combining navigators with passive NMR markers. The joint retrospective approach has recently been expanded to first-order field correction[134], using fat navigators. Dual prospective correction with first-order field actuation has been achieved with cloverleaf navigators[15], reaching a high tracking rate at relatively large expense of scan time (30%) for navigation. More recently, similar functionality has been reported based on 3D EPI navigators[148]. In this implementation, sparser tracking at

intervals of about 10 s is accomplished with less scan time overhead of approximately 10%.

The goal of the present work is to advance joint field and motion correction with a view to the demanding scenario discussed initially, i.e., high-resolution T2*-weighted imaging at high field. For this case, dual correction should be prospective and deploy high-sensitivity, high-rate field and motion detection without adding to already long scan times. For use at high field it should also address higher-order field perturbation and be compatible with dense receiver arrays. To this end, we propose to combine higher-order field control based on NMR sensing[3] with motion correction equally based on NMR markers[24].

In combining the two correction techniques, it is important to consider that both are based on repeated sensing and adjustment of magnetic fields in the same volume of interest. They effectively form two simultaneous control loops operating on partly shared physical quantities and thus bear potential for mutual interference and instability. To address this aspect, the proposed strategy is described and analyzed from a control perspective with particular attention to pathways and effects of interference.

We report an implementation for head imaging at 7T. Along with technical performance assessment, dual control is demonstrated by T2* imaging in vivo, including scenarios with pronounced motion and field perturbation and motion.

4.2 Methods

The proposed system combines two control loops, one for field stabilization and one for motion correction (Figure 4.1).

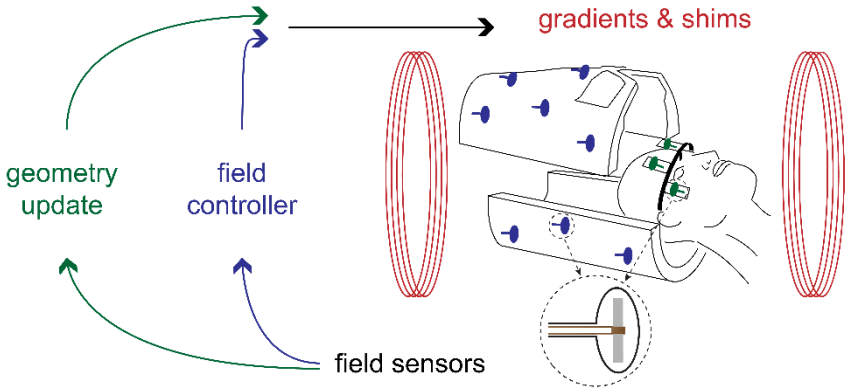

Figure 4.1: Diagram of the two correction loops. Field control and prospective motion correction rely on two different sets of field sensors. The sensors used for field control (blue) are rigidly mounted around the receiver array and perform field measurements during the scan. A proportional integral controller determines the necessary shim and gradient inputs to compensate for the measured field deviation. Gradients and higher-order shims are actuated accordingly (path in blue). The sensors used for prospective motion correction (green) are mounted on a headset worn by the subject. They are localized during the scan to obtain head tracking data. The sequence geometry is updated accordingly (path in green).

4.2.1 Field control

The task of the field control loop is to suppress changes in magnitude and spatial variation of the background magnetic field within the imaging volume. In this work, it is implemented in the fashion previously

described in Ref. (3). A set of field sensors around the volume of interest (Figure 4.1) measure the background magnetic field at regular intervals. Deviations from the target field distribution are translated into field corrections by a proportional-integral (PI) controller. The corresponding field actuation is performed by real-time 3rd-order shim adjustment.

4.2.2 Prospective motion correction

Motion correction is performed prospectively, i.e., by continuous re-alignment of the sequence geometry with the head. Motion detection for this purpose is performed by tracking NMR sensors, acting as markers, mounted on a headset worn by the subject[27]. Marker positions are derived from the phase time courses of marker FIDs acquired during short intervals of high-frequency gradient oscillations as detailed in Ref. (24). Joint processing of the marker positions yields rigid-body motion parameters that describe translation and rotation of the head relative to the initial pose. The motion parameters are forwarded to the console for corresponding update of gradient orientations as well as RF pulse and signal demodulation frequencies.

4.2.3 Control perspective

Automatic control generally seeks to keep certain process variables stable at given set points. To this end, each process variable is continuously measured and compared with its set point, yielding the

$$error(t) = set\ point - process\ variable(t),$$

which is then countered by changes to system inputs.

In the field control loop, the process variables are the values of the background magnetic field at the sensor positions. The set points are the

field strengths observed in an initial reference state. The proportional-integral controller translates observed field errors at t_k into field corrections according to

$$correction(t_k) = K_p \left(error(t_k) + \frac{1}{T_i} \int_{t_k - T_i}^{t_k} error(t_k) dt \right) + correction(t_{k-1})$$

with proportional gain $K_p < 1$ and integration time T_i. Compared to mere proportional feedback, PI control offers better blocking of measurement noise at the expense of control bandwidth. This is the approach of choice here because noise in field measurements is significant, perturbations of the background field are relatively slow, and the overall control bandwidth is limited irrespectively by eddy currents induced by higher-order shim switching.

In the PMC loop, the process variables are the parameters describing rotation and translation of the imaging volume relative to the head. The set points reflect the scan geometry chosen in the initial head pose. Unlike field correction, realignment of the imaging volume is done fully in each cycle and based only on the latest motion detection data, i.e.,

$$correction(t) = -error(t)$$

for each of the rotation and translation parameters. In control terms, this amounts to pure proportional control with full gain ($K_p = 1$), which achieves fast correction at the expense of susceptibility to measurement noise. This is adequate because head motion can be relatively fast and sequence geometry update is effectively instantaneous while detection noise in motion parameters is less prominent than in field measurements.

4.2.4 Potential interferences

When operated simultaneously, the two loops are subject to mutual interference and thus potential instability because both sense and manipulate magnetic field in a shared volume of interest. They also overlap in terms of the targeted frequency bands, which range from DC to fractions of Hz for the background field and to approximately 10 Hz for motion.

The first kind of interference is any change in detected motion caused by field actuation. This pathway is inhibited by exploiting the fact that the gradient dynamics used for motion detection do not need to be in the same spectral range as the motion itself. Instead, motion detection is based on high-frequency field dynamics, using short gradient tones in the kHz range and high-pass filtering of marker observations. In addition, motion detection and field updates are well separated in time to prevent the high-frequency content of shim switching from contaminating motion readouts. For most sequences, separation by at least several ms is straightforward. This alone may not suffice, however, in the presence of mechanical resonances of gradient coils, which may have lifetimes in the same order of magnitude or longer[52]. Mechanical resonances are also subject to change in amplitude and lifetime upon heating of gradient coils. Therefore, as an additional precaution, the tone frequencies are chosen well clear of the mechanical resonances of the gradient system.

Interference in the reverse direction, i.e., influence of geometry update on the measurement of background field, must equally be avoided. Geometry updates slightly alter the relative contributions of the three physical gradient chains to each gradient object in a sequence. Therefore, they also cause subtle differences in eddy currents and

mechanical resonance behavior after gradient switching. To limit cross-talk of these effects into the field control loop, the field measurement should not be performed immediately after the switching of gradients that are subject to update. For similar reasons, it should not closely follow phase encoding gradients, whose amplitude and thus eddy current effects change from repetition to repetition. In steady-state and balanced sequences, the same holds for spoilers and rephasers, respectively, in the phase-encoding direction. In principle, these considerations can be circumvented by performing the field measurement at the echo time during the readout gradient. In this case, capturing eddy current and resonance effects is actually welcome because they affect image acquisition in the same way, so countering them by field control will be beneficial. However, in the presence of geometry updates the field control loop would need to be informed of the current gradient demand on every axis, relying on a known and perfectly reproducible latency of the PMC loop, which can be challenging due to small jitter in the time interval until a requested geometry update is executed.

4.2.5 Hardware and implementation

4.2.5.1 Scanner & operation of field sensors

The experiments were performed on a 7T Philips Achieva system equipped with a third order shim system (Philips Healthcare, Best, The Netherlands) and a 32-channel head receive array (Nova Medical, Wilmington, Massachusetts, USA).

All NMR field sensors[31] were based on 19F and operated with a custom stand-alone console and receiver[33].

4.2.5.2 Imaging sequence

All experiments were performed with a 2D T2*-weighted GRE sequence (resolution: 0.4 x 0.4 x 1.5 mm³, echo time (TE): 25 ms, excitation repetition time (TRexc): 50 ms, bandwidth: 144 Hz, duration: 8 min 23 sec). The sequence timing is illustrated in Figure 4.2. A trigger (TTL pulse) was added 0.3341 ms after the readout gradient to trigger signal excitation and acquisition of the field sensors. Subsequently, a position and field sensing module were inserted, that consisted of three sinusoidal gradients for marker encoding (frequencies: 2 kHz, 3 kHz, and 4 kHz, amplitudes: 7 mT/m, duration: 1 ms) and a brief period of 3 ms without gradient activity used for field measurement. The spoiler gradient was shifted accordingly (Figure 4.2). These settings reflect the considerations presented in the previous section and were governed by the goal to minimize potential interferences between the two loops.

4.2.5.3 Field Control

Sixteen long-lived field sensors (T1 ~ 86ms) were mounted on a laser-sintered frame inserted between the transmit and receive arrays. Signal acquisition was performed upon every other TTL pulse trigger. NMR sensor data was acquired over 4.51 ms. The signal from 1.5 ms to 4.5 ms was used to compute the field values. The gain of the proportional integral controller was $K_p = 0.27$ and the integration time $T_i = 0.07\ s$.

The static field responses to unit input demand were successively calibrated for each shim coil and stored in a matrix $\boldsymbol{C}$ with C_{ij} being the static field response at the position of the i-th field sensor under actuation of the shim j with a unit voltage. The error in the field was translated into shim input errors and the shim updates were given by the

controller. The measurement and correction rate was 10 Hz. The latency of the field control loop, i.e. the time between reception of the field value and shim actuation, was between 3 and 9 ms.

The target field values were determined during a calibration run of 10 seconds just before the imaging experiment. They accounted for the shim settings and the sequence's eddy currents and oscillatory fields at sensing time under the reference geometry.

4.2.5.4 Prospective motion correction

Throughout all scans, the positions of four short-lived NMR markers (T1 ~ 2.1 ms) were computed based on an initial calibration[24].

Signal acquisition was performed upon each pulse trigger received from the scanner. The first 1.2 ms of the signal were used to compute the sensor positions (Figure 4.2). The sequence update was determined by computing the rigid body transformation between the current sensor positions and a set of reference positions using the method of Umeyama[47]. The set of reference positions was kept fixed between successive in vivo scans, such that the scan planning was consistent, which facilitated comparing the acquired image data.

The geometry update was sent to the scanner host via a TCP connection using an external data interface[46]. The measurement and correction rate was 20 Hz with a latency of 50 to 100 ms.

The images were reconstructed using standard Fast Fourier Transform reconstruction.

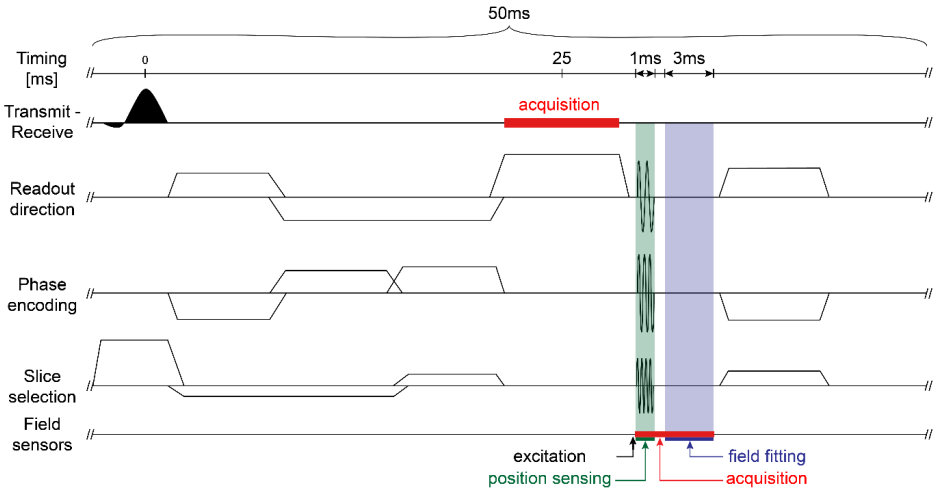

Figure 4.2: Schematic of the flow compensated gradient recalled echo sequence. To perform field control, the static field situation in the scanner bore is assessed by measuring the field over several milliseconds. For prospective motion correction, sinusoidal gradients were used to encode the marker positions.

4.2.6 Characterization experiments

The following experiments were designed to study the double control loop system. This was done through evaluating potential interactions by operating each loop with controlled stepped inputs. By analyzing both the field and the rigid-body parameters that are measured throughout all scans, potential interaction between the control loops can be detected. In case of no interaction between the loops, input on either loop should not affect the measurements in the respective other loop.

For all characterization experiments the markers used for PMC were mounted in a static, non-collinear geometry on a phantom. In these characterization experiments, where no imaging was performed, the

duration of the sequence was doubled by increasing the number of slices and TR.

To assess the effectiveness of the field control loop, the average root-mean-square deviation (RMSD) of the measured field with respect to the target field value was computed across the sixteen sensors. A large average RMSD would indicate that the field was instable and / or that the field was off of the specified target. As those two phenomena should be prevented by using field control, it is expected that, in case of successful field stabilization, average RMSD should be small. Hence, the field RMSD is a good indicator to the performance of the field control loop.

Conversely, motion parameters are reported in terms of standard deviation (STD) since this yields a direct estimate for tracking precision in a static setting and quantifies the prevalence of motion in vivo. The effectiveness and quality of the PMC loop is to be assessed in the image directly and this is done, in the imaging experiments, by inspecting difference images.

4.2.6.1 Effects of field actuation

The field control loop was replaced by artificial input to the gradient and shim coils, that consisted of stepped demands. Stepping through the demanded shim inputs should result in measurable field changes, but should not affect the determined rigid-body parameters.

To describe the effect of the shim field, the unit “Hertz Maximum 20cm”, abbreviated [HzMax20], is used. It corresponds to the maximum field deviation occurring over a sphere of 20 cm centered at the isocenter.

The amplitude of input steps ranged from a couple of [HzMax20] reflecting typical physiological disturbances, to dozen of [HzMax20] to assess the system behavior under extreme field fluctuations. All shim terms were actuated successively over a duration of 6 seconds per input, interleaved by phases of zero input equally lasting 6 seconds. Zeroth and first-order shims were actuated with input steps of 2, 6, and 20 [HzMax20]. Second and third-order shims were actuated with decreased input steps of 1, 3, and 10 [HzMax20] to maintain a level corresponding to physiological effects.

This experiment was performed without and with geometry updates in the PMC loop.

4.2.6.2 Effects of motion updates

Since PMC modifies the gradient fields only via rotation of scan geometry, input steps corresponding to rotations about the various axes were used to inspect robustness of the field control loop in the presence motion updates. If there was no interaction between the two loops, no field changes should be visible during the period of field sensing in the field control loop. Rigid-body parameters should not be affected by rotation of the applied gradient waveforms.

To carry out these experiments, the PMC loop was replaced by artificial updates of the gradient waveforms. Geometry updates were held constant during 6 seconds, before returning to zero for another 6 seconds. Rotations about every axis with amplitudes of ±1°, ±3°, ±10°, and ±30° were applied. Field values and rigid body motion parameters were tracked without and with shim actuation.

4.2.6.3 *Simultaneous field and motion control*

The simultaneous operation of the two loops can potentially lead to instabilities and divergent behavior, resulting in possible damage to the hardware. As certain frequency bands might be more sensitive than others, it is necessary to test whether the system has such sensitivities using a wide range of input frequencies on either loop. One intrinsically broadband input is noise naturally present in the scanner. In this experiment, the two control loops were run simultaneously without specific input other than detection noise.

All four modes of control were carried out, i.e. both loops being inactive, only one of the loops being active at a time, and both loops being active. Field values and rigid body motion parameters were recorded during all conditions.

4.2.7 Phantom imaging

Imaging of a spherical phantom was carried out under four conditions: without correction, with one correction at a time, and with both corrections. For the purpose of comparison, data without any correction was acquired twice and used as reference for difference images. The markers used in the PMC loop were rigidly attached to the phantom in non-collinear geometry.

Field values and rigid-body motion parameters were tracked under those four conditions. The standard deviation of rigid-body motion parameters and the fields measured by each sensor is reported.

4.2.8 In vivo imaging

For in vivo imaging, the markers used for tracking were attached to a 3D-printed headset worn by the subject, as illustrated in Figure 4.1.

Imaging was performed in healthy volunteers who gave written informed consent. The measurements were performed according to the applicable ethics regulations. The field, rigid-body parameters and the correction traces were recorded for all experiments. Imaging was performed in a normal scenario as well in scenarios of increased perturbation. To assess the results, difference images of each dataset to the corresponding case with both corrections were computed. The tracked field is reported in terms of the shim basis to provide insights into the spatial complexity of field disturbances.

4.2.8.1 Normal breathing

A healthy volunteer with normal BMI (21) was scanned. Image data was acquired for the different combinations of PMC and field control, i.e. without correction, with one correction at a time, and with both corrections. The volunteer was instructed to lie still throughout all measurements.

4.2.8.2 Increased field perturbation

The second dataset was acquired in a healthy volunteer with a high BMI (28), naturally resulting in increased field perturbations. Increased field perturbations were reported to occur in the clinic with Alzheimer patients[2]. The volunteer was instructed to lie still during the measurement. Imaging was performed without any correction and with both corrections.

4.2.8.3 Instructed motion

To mimic conditions of a subject with difficulties in lying still, a healthy volunteer with normal BMI (21) was instructed to repeatedly change the leg position by either parallel or crossed positioning of the legs.

Necessary safety measures were taken to prevent skin contact. To ensure consistent conditions in repeated scans, an acoustic signal was emitted every 1:15 min notifying the subject to change the leg position. Again, the measurement was performed without any correction and with both corrections. The volunteer was the same person as for the normal breathing experiments.

4.3 Results

4.3.1 Effects of field actuation

Figure 4.3 shows field sensor traces and time series of rigid-body parameters acquired in the presence of boxcar inputs of varying amplitude to the shim channels. The field traces reflect the shim switching with varying excursion depending on the sensor position. For certain shim terms, the field response closely follows the boxcar demand while others show transient overshoots and delayed settling. This expected behavior reflects cryostat eddy currents induced by the unshielded higher-order shim coils as detailed in Ref. (149). The important finding from this data is that changes in shim fields did not affect the concurrently acquired series of motion parameters (Figure 4.3c), which fluctuated only stochastically with standard deviations in the order of 10 µm and 0.01 deg (Figure 4.3f). Robustness of motion detection against shim switching is confirmed by the same behavior after closing the motion control loop, i.e., with continuous geometry updates (Figure 4.3e/g).

4.3.2 Effects of motion updates

Figure 4.4 shows rigid-body parameters and field traces acquired in the presence of forced geometry update, mimicking rotations by 1-30° about

the Anterior-Posterior (AP) (a-e), Left-Right (LR) (f-j), and Foot-Head (FH) (k-o) axes. The geometry changes cause slight bias in motion parameters, up to about 50 μm of translation, which occur upon large FH rotations. The biases occur only with one sign of rotation, which may relate to a slight polarity dependence of gradient amplifier behavior.

Geometry updates also perturb the background magnetic field (Figure 4.4b,g,l). These effects are small for rotations in the typical range of patient head motion (±1° and ±3°) but reach more significant field offsets upon large rotations (±10° and ±30°). They are likely caused by alteration of eddy current patterns upon rotation of the imaging sequence, as discussed in the Methods section (Concern 5). The field perturbations are automatically countered when closing the field control loop (Figure 4.4e,j,o). Brief residual field excursions are still caused by large, sudden rotations (Figure 4.4o), reflecting finite control bandwidth.

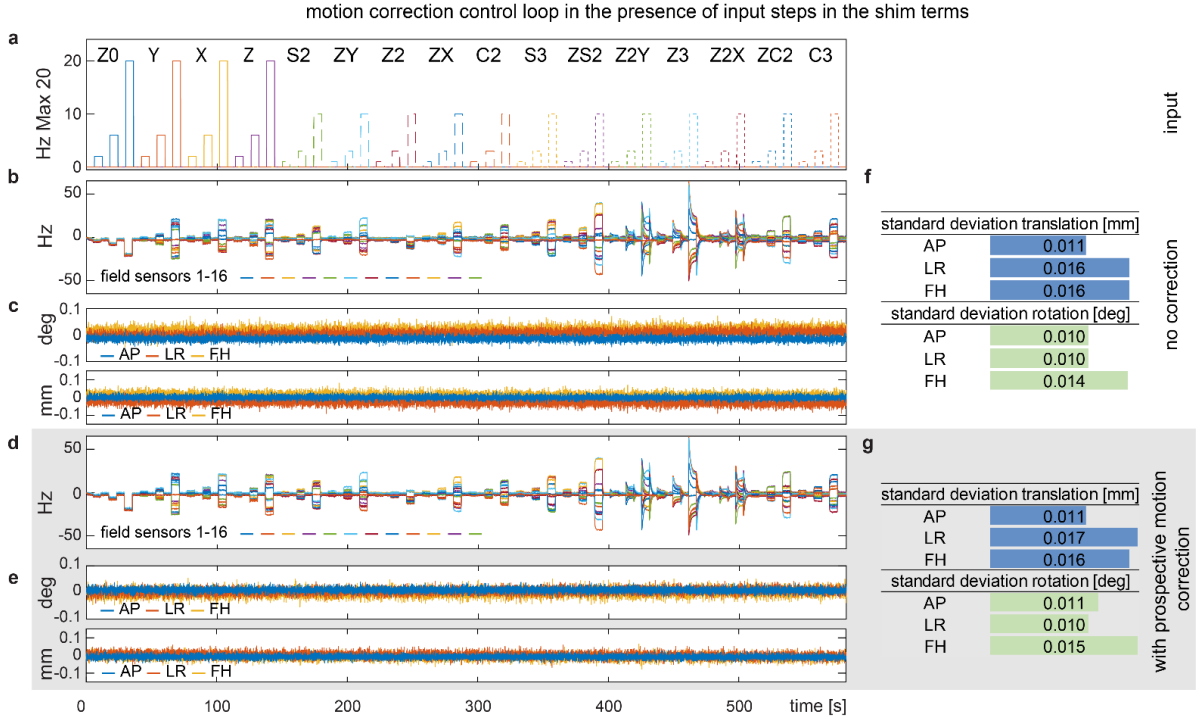

Figure 4.3: Field sensor outputs (b) and detected motion parameters (c,f) in the presence of boxcar shim inputs (a), without motion correction. The motion parameters show no sign of interference by shim switching. Repetition with prospective motion correction (d,e,g) yields the same results.

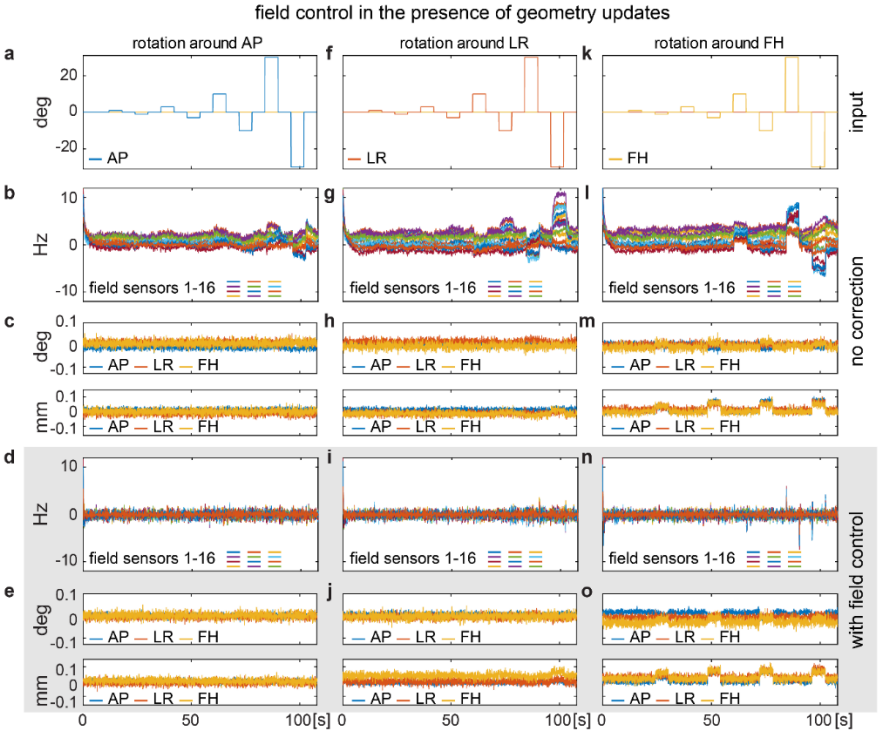

p

	rotation around AP		rotation around LR		rotation around FH	
	no correction	with field control	no correction	with field control	no correction	with field control
	average root mean square [Hz]					
field sensors	1.509	0.687	2.012	0.708	2.457	0.730
	standard deviation translation [mm]					
AP	0.011	0.010	0.010	0.010	0.028	0.029
LR	0.016	0.016	0.014	0.017	0.021	0.024
FH	0.017	0.016	0.016	0.018	0.026	0.027
	standard deviation rotation [deg]					
AP	0.008	0.008	0.007	0.008	0.010	0.011
LR	0.011	0.010	0.011	0.010	0.010	0.010
FH	0.013	0.013	0.012	0.013	0.014	0.015

Figure 4.4: Motion parameters (c,e,h,j,m,o) and field traces (b,d,g,i,l,n) recorded in the presence of gradient waveforms rotated about different axes between 1° and 30° (a,f,k). Large rotations cause slight bias in translation parameters. By altering eddy currents they also introduce

field excursions (b,g,l), which are largely eliminated by field control (d,l,n). (p) Average root-mean-square values and standard deviations of field readouts and motion parameters, respectively.

4.3.3 Simultaneous field and motion control

Figure 4.5 shows measured field and motion parameter traces obtained without any actuation, with field control only, with motion control only, and with simultaneous control. The root mean square of the field, averaged over the sensors (aRMS) and the standard deviation (STD) of the motion parameters are given in the adjacent tables (Figure 4.5e,f,k,l). They were taken only over the second half of the experiment to exclude the initial transition of long-lived eddy currents into steady-state, which is visible in the field traces (a) and (g).

The observed motion parameters show the same range of fluctuation in all four cases. At STD of 10-17 um for translation and 0.008-0.015° for rotation they exhibit the same levels of stability as previously with field actuation only. However, the field behavior differs between the different control modes. Prospective motion correction increases field fluctuation as may be expected based on the results shown in Figure 4.4. This effect is most prominent without field control where it roughly doubles the field STD. Field control, by itself, increases the noise level slightly (Figure 4.5a,c), reflecting amplification of noise outside the control bandwidth, which is common in proportional-integral control systems[3]. In combination with motion correction, the effect of field control is dominated by its ability to reduce field perturbation caused by geometry updates (Figure 4.5g,i), achieving a net reduction of the field aRMS.

Besides these details, Figure 4.5 shows the key result that simultaneous operation of the two control loops is stable at virtually no expense in

terms of either field or motion sensitivity. This indicates that the residual coupling between them is sufficiently small to prevent feedback from escalating detection noise and direct mutual perturbation in a detrimental fashion.

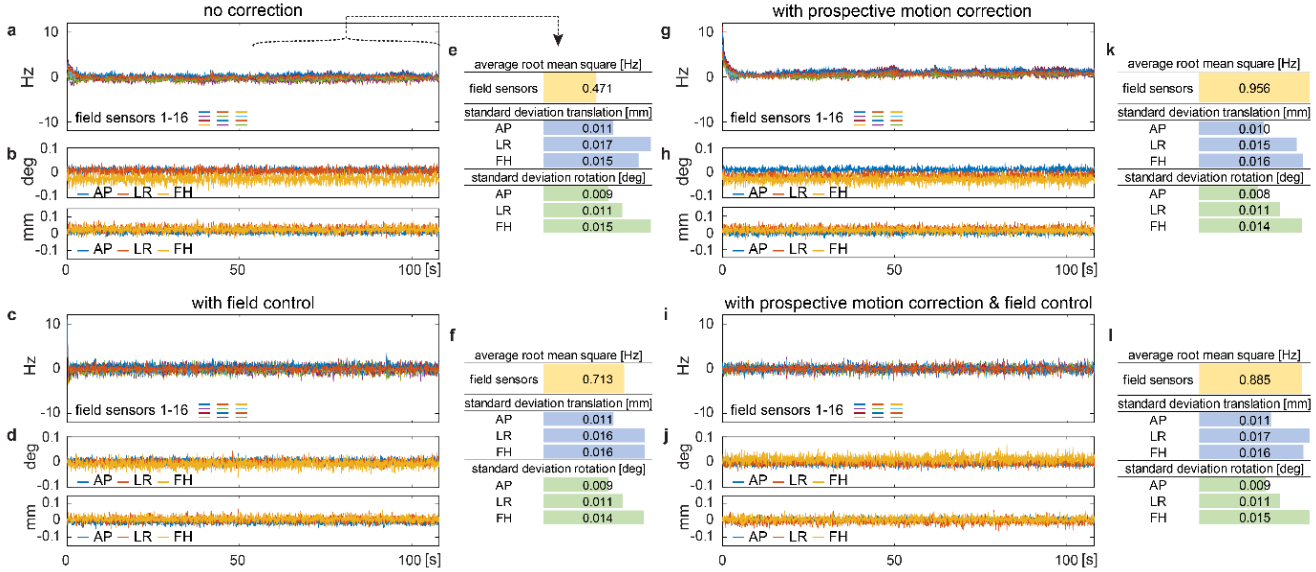

Figure 4.5: Field traces and motion parameters acquired without correction (a-b), with field control only (c-d), with prospective motion correction only (g-h), and with joint prospective motion correction and field control (i-j). (e,f,k,l) average root-mean-square deviation (RMSD) and standard deviation (STD) of field readouts and motion parameters, respectively.

4.3.4 Phantom imaging

Figure 4.6 shows one slice of the phantom imaging results, which serve to verify that joint control does not have detrimental side effects at the imaging level. To highlight subtle features, zoomed details are provided as well as differences from a reference image acquired without any control. The difference images are scaled to +/- 30% of the maximum intensity of the reference dataset. With all modes of control, resulting images match the reference very closely.

The difference between the two no-control results (Figure 4.6, third column, first row) reflects the general reproducibility of the imaging procedure. It shows subtle discrepancies of uncertain origin, which may include slight changes in background and shim fields as well as the common stability limits of RF chains and clocking. The images obtained with different modes of control differ more, albeit very slightly. With prospective motion correction only, edges of the phantom and enclosed bubbles are slightly pronounced in the difference image, which is to be expected due to finite precision of motion detection in the order of 10-20 µm[27]. Measurement noise involved in initializing motion control could be an additional cause. With field control only, somewhat more pronounced internal features and subtle ghosting in the difference image likely relate to the slight elevation in field noise observed earlier. The result obtained with joint control arguably combines these effects, albeit still at so subtle a level that they are hard to attribute. Overall, these results confirm that simultaneous control was stable and its finite sensitivity did not impair imaging in the absence of motion and significant field perturbation.

Figure 4.7 shows the field and motion parameters recorded during the phantom imaging experiments. The data illustrates that field control

removed long-term field drift whereas the motion parameters exhibit a transition at half the scan time. The latter does not reflect actual motion but is an artefact related to the phase-encoding gradient changing polarity. It is likely of the same nature as the similar effect observed in Figure 4.4, which was equally on the order of 50 um. The fluctuation ranges of the field and motion recordings are reported in Table 4.1 and Table 4.2.

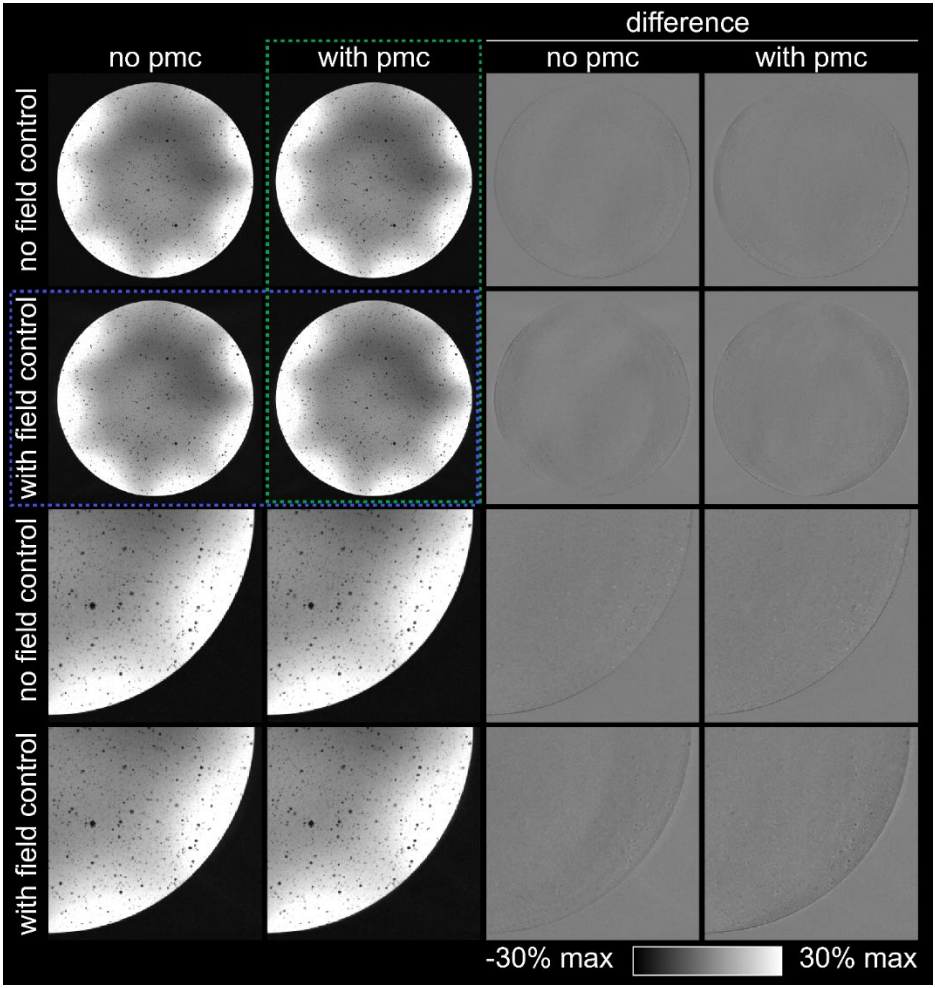

Figure 4.6: High-resolution T2-weighted imaging of a gel phantom with fine bubbles for structural contrast. Imaging was performed in four ways: without any control, with prospective motion correction only, with field control only, and with joint control. Subtraction from a second image without control emphasizes subtle differences (right).*

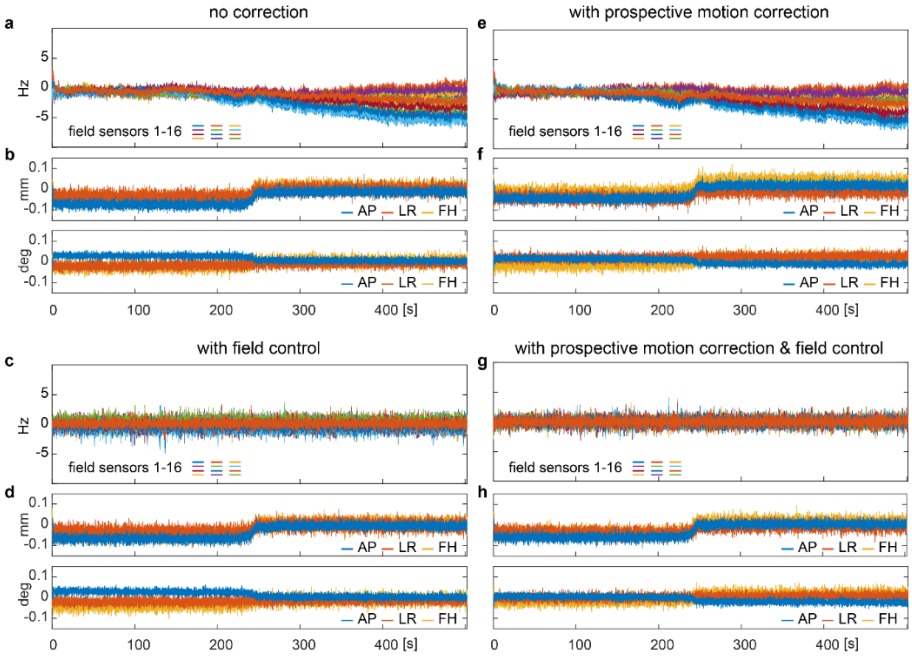

Figure 4.7: Field traces and rigid-body parameters from four phantom imaging experiments: without control (a,b), with field control only (c,d), with prospective motion correction only (e,f), and with joint control (g,h).

4.3.5 In vivo imaging

Figure 4.8 shows two slices of a set of brain images, again obtained without correction, with prospective motion correction only, with field control only, and with joint control. Differences from the fully corrected case are scaled to ±30% of maximum intensity. Without field control (1st and 3th rows), the images suffer from intensity modulations mostly in the right posterior region and the anterior part of the lower slice. Without motion correction (1st column), motion artefacts are visible in the anterior parts of both slices. Blurring and ringing due to motion are visible at the

interhemispheric fissure. Field control (2nd and 4th row) removed the intensity modulations whereas motion correction (2nd and 6th column) removed blurring and ringing. Both types of artefacts are eliminated by simultaneous correction. For example, small vessels near ventricle in the lower slice are sharply depicted only with dual control.

Tissue motion and related artefacts are greatest in the anterior part of the brain because it is the farthest from the occipital pivot point. Conversely, field perturbations are strongest in the posterior inferior part of the brain due its greater proximity to the lungs and the limbs[141]. Figure 4.9 shows the tracked field and the motion parameters corresponding to Figure 4.8. Without field control, the field traces exhibit regular breathing patterns up to 6 Hz peak-to-peak and a slow drift similar to that observed in the phantom experiment (Figure 4.7a,e). In Figure 4.9e, at about 140 sec a sudden field change occurs that is likely due to limb motion. With field control, the background field is kept stable throughout. The motion parameters are of comparable range across the four experiments. Breathing-related motion is conspicuous as regular translation along FH and rotation around RL. Figure 4.9b and Figure 4.9f include sudden motion events, after which the head returns approximately to its previous position within a few seconds. These dynamics are likely associated with swallowing. The statistics of the recordings and derived shim inputs are reported in Table 4.1 and Table 4.2, respectively.

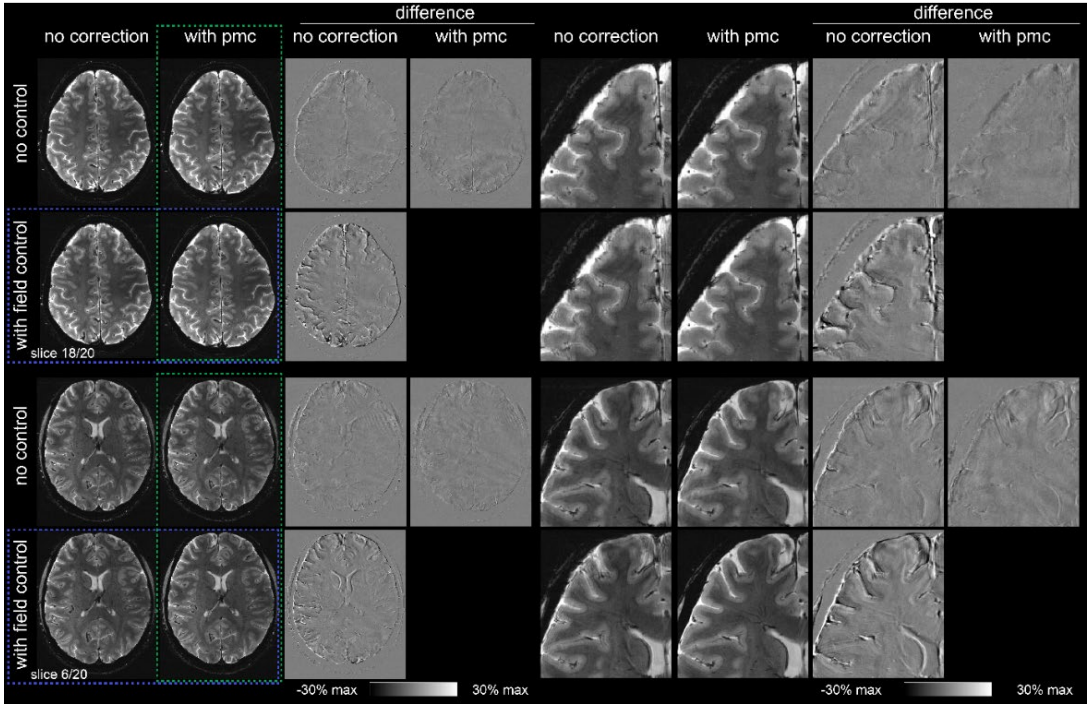

Figure 4.8: In vivo brain imaging performed without correction, with prospective motion correction only, with field control only, and with joint control. Difference images to the fully corrected case show that characteristic artefacts, such as intensity modulations provoked by field fluctuations, or blurring and ringing provoked by motion, are eliminated by simultaneous correction.

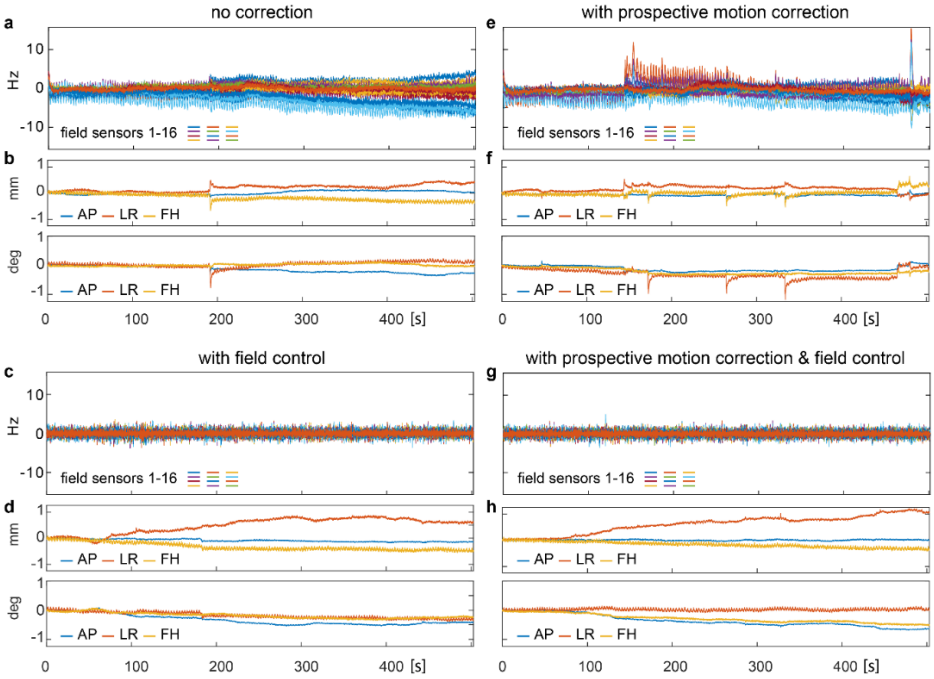

Figure 4.9: Field traces and rigid-body motion parameters of four in vivo measurements: without control (a,b), with field control only (c,d), with prospective motion correction only (e,f), and with joint control (g,h)

4.3.6 Increased perturbations

Figure 4.10 shows imaging results obtained in the presence of increased field perturbations related to higher BMI. Without either correction, this more challenging scenario led to significantly impaired image quality, with blurring, regional shading effects, and motion artefacts. With simultaneous control, these problems are strongly mitigated, recovering features such as vessels and grey-white-matter boundaries.

Figure 4.11 shows field traces and rigid-body parameters of the in vivo experiments with increased field perturbations. Field traces in Figure 4.11a show that peak-to-peak breathing amplitude varied over time and is about 10 Hz at max, larger than in the normal breathing case (Figure 4.9a,e). Field drift during the acquisition is, as in Figure 4.7 and Figure 4.9(a,e), present. In the corrected case, the field is stabilized to baseline. One event occurred at about 410 sec for which the controller needed one second to stabilize the field. Such behavior is expected for field perturbations with frequency content beyond the controller bandwidth. Motion was moderate in both experiments within expected amplitudes for a cooperative subject. As in

Figure 4.9, translation in FH and rotation around RL follow breathing dynamics. The corresponding field aRMS and rigid-body parameters STD of the four experiments are reported in Table 4.1, and the STD of the field translated in shim terms are reported in Table 4.2.

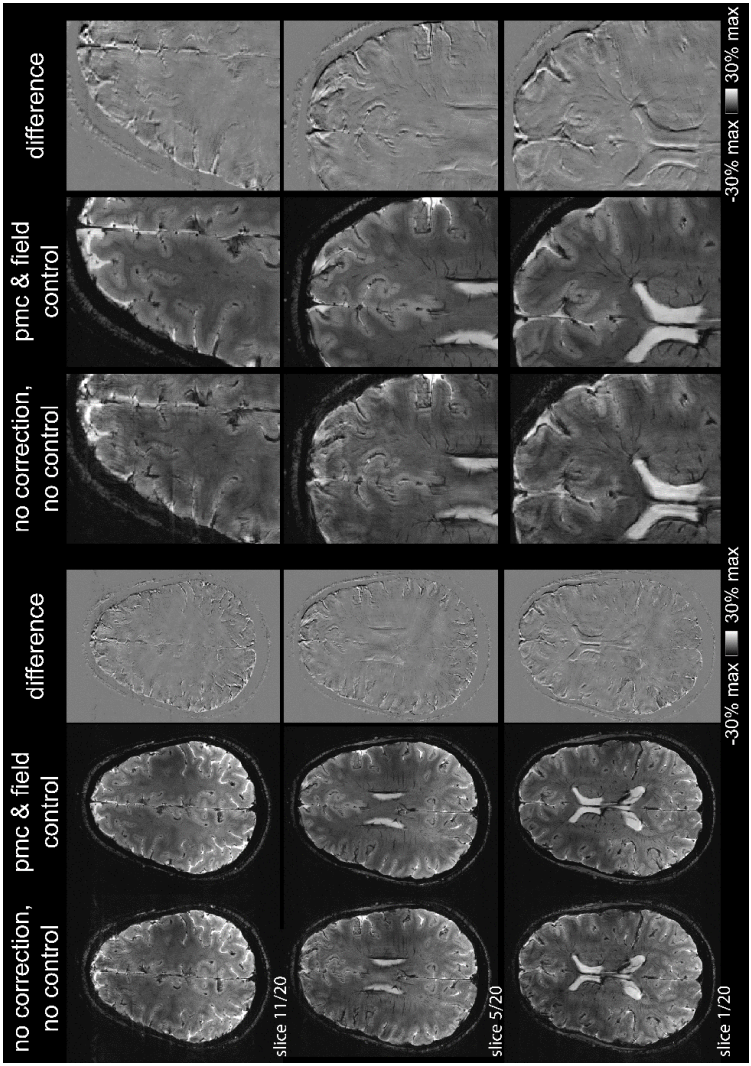

Figure 4.10: In vivo imaging with increased field perturbations due to an increased body mass index. Anatomical features that are indistinguishable in the uncorrected case become visible in the corrected case.

Figure 4.12 shows three slices of in vivo experiments with instructed motion. The subject was instructed to change the leg position every 1min15sec and lie still the rest of the time. The instructions were designed to mimic an uncooperative subject. Without correction and control, the homogeneity in white matter is corrupted and anatomical features such as gray-white matter boundaries are not distinguishable, e.g. in the regions shown in the close-ups. Inhomogeneity in white matter and motion blurring are particularly pronounced in these data and the overall image quality is strongly deteriorated. Image quality is recovered when both prospective motion correction and field control are employed. The difference images to the corrected case highlights the differences. In all slices, intensity modulation, principally along RL, and motion artefacts, mainly at the anterior of the slices, are visible. The close-ups make the improvement of the image quality clear: gray-white matter boundaries are distinct and vessels near the ventricles are well depicted (slice 4).

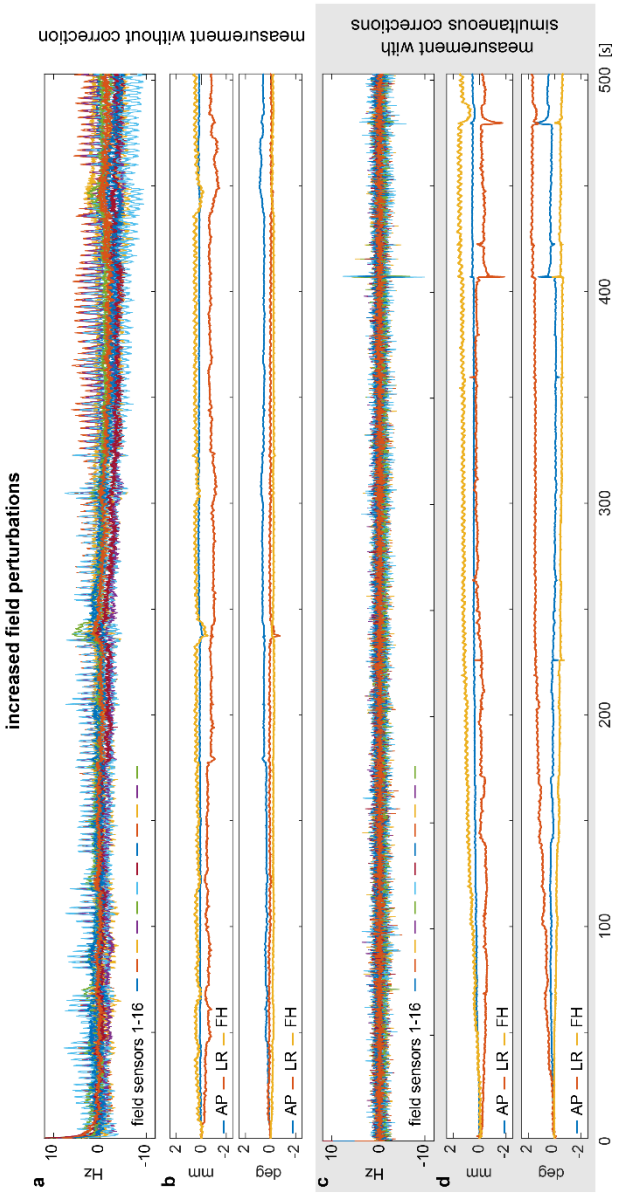

Figure 4.11: Field traces and motion parameters of in vivo experiments with increased field perturbations.

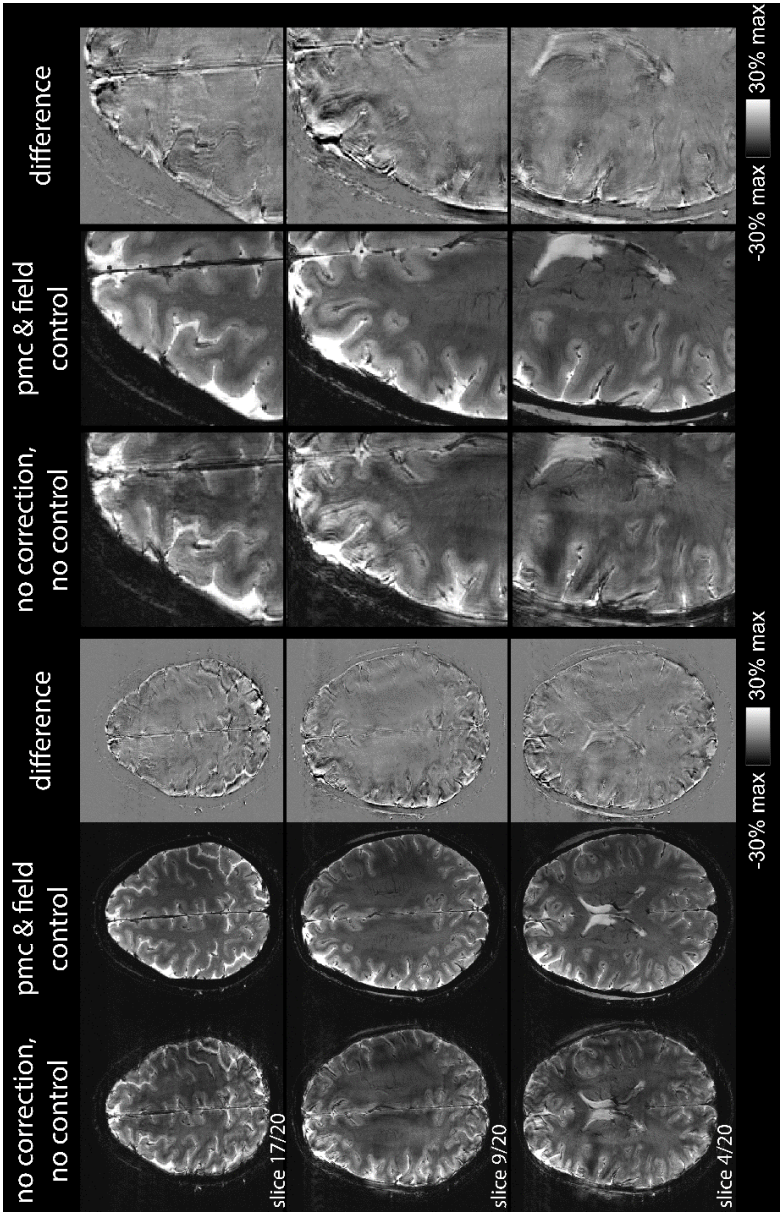

Figure 4.12: Three slices from the in vivo experiments with instructed motion without and with joint control.

Figure 4.13 shows the field traces and rigid-body parameters corresponding to Figure 4.12. In the field traces (Figure 4.13a), breathing dynamics are visible. Shifts in the field coincide with leg movements and large field excursions of up to two dozen of Hz occur. The field excursions are mostly brought back to baseline in the experiment with joint corrections (Figure 4.13c). Some imperfections in the field traces remain at times when legs were repositioned. Such changes yielded field changes covering a large bandwidth. As for Figure 4.4, field traces are not perfectly stabilized because of the finite bandwidth of the field control loop's controller. These imperfections did not lead to appreciable image quality deterioration (cf. Figure 4.12). Motion parameters were comparable in the two experiments (Figure 4.13b,d) with clearly visible head motion at times of leg movement. The corresponding field aRMS and rigid-body parameters STD of the four experiments are reported in Table 4.1, and the STD of the field translated in shim terms are reported in Table 4.2.

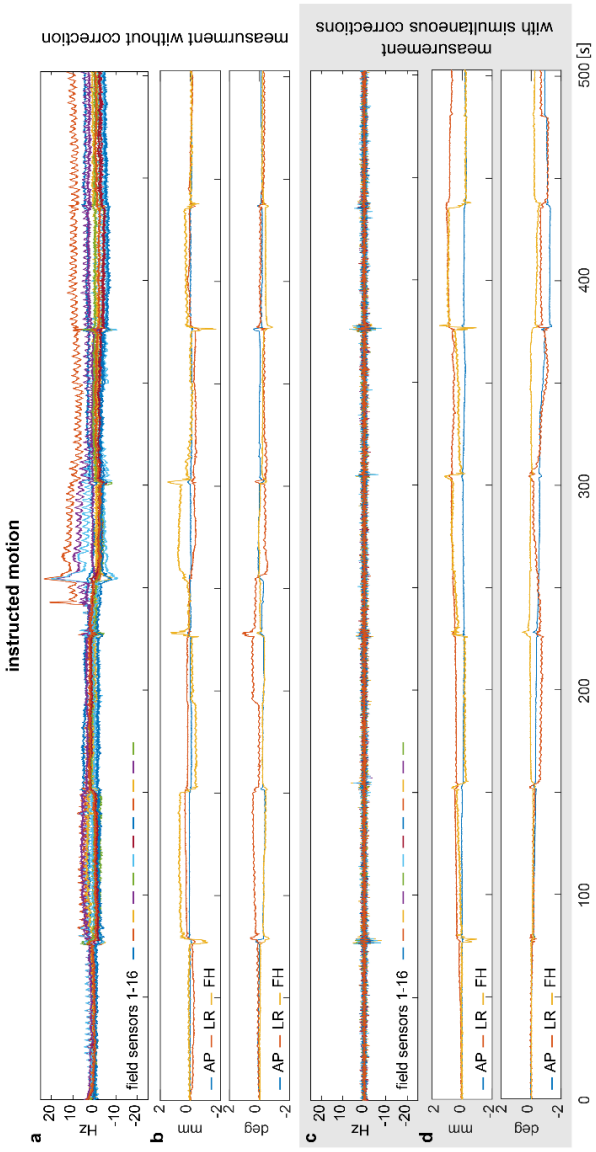

Figure 4.13: Field traces and motion parameters of in vivo experiments with instructed motion. The subject changed the leg position at regular intervals (approx. every 1min 15sec).

Table 4.1 presents the statistics of field fluctuation and motion parameters for all imaging experiments. On average, field control decreases the field aRMS from 1.952 Hz to 0.739 Hz. The field aRMS without field control is lower in the in vivo imaging experiments with normal breathing than in the phantom imaging experiments because breathing dynamics make the field return close to baseline periodically during the scan while in the phantom experiment only the field drift is present. Besides, the level of field fluctuations does not only depend on the experimental design but also on the noise present in the scanner. The scanner background noise was probably higher for the phantom experiments due to an increase in hardware temperature as the data were acquired without pauses between the scans contrary to the in vivo data for which breaks between scans were consented to allow the subject to relax (between 3 and 5 minutes). During this time the hardware could cool down.

In the experiments with increased field perturbations, field control obviously reduces the field aRMS but not to the same level as in the normal breathing case. This is likely due to the described remaining peak at about 410 sec as shown in Figure 4.11c. In the experiments with instructed motion, field aRMS without correction is the highest of all. Field control decreases the aRMS to a level similar to the phantom and normal breathing experiments. Root mean square of the rigid-body parameters reflect the traces presented in Figure 4.7, Figure 4.9, Figure 4.11, and Figure 4.13. The scans without PMC have at most as much motion as in the scan with PMC which excludes that the image

quality achieved in the experiments with PMC is due to absence of motion.

corrections		average rms [Hz]	std translation [mm]			std rotation [deg]		
field control	motion correction	field sensors	AP	RL	FH	AP	RL	FH
phantom imaging								
no	no	1.946	0.033	0.024	0.031	0.015	0.014	0.021
no	yes	1.866	0.034	0.024	0.032	0.016	0.013	0.022
yes	no	0.771	0.034	0.025	0.033	0.016	0.014	0.022
yes	yes	0.626	0.034	0.024	0.032	0.016	0.014	0.022
in vivo imaging - normal breathing								
no	no	1.605	0.073	0.129	0.128	0.112	0.095	0.044
no	yes	1.502	0.032	0.108	0.111	0.096	0.160	0.104
yes	no	0.700	0.050	0.288	0.148	0.176	0.110	0.098
yes	yes	0.686	0.020	0.336	0.111	0.208	0.038	0.145
in vivo imaging - increased field perturbations								
no	no	1.986	0.061	0.255	0.155	0.171	0.082	0.056
yes	yes	0.933	0.138	0.288	0.454	0.179	0.455	0.197
in vivo imaging - instructed motion								
no	no	2.806	0.054	0.219	0.354	0.135	0.292	0.145
yes	yes	0.719	0.086	0.257	0.377	0.401	0.351	0.152

Table 4.1: Average root-mean-square (rms) of field measurements and standard deviation (std) of rigid-body parameters for all imaging experiments.

Table 4.2 presents the field aRMS translated in shim terms. A few observations can be made: the different shim terms are not used in the same way. The terms which are most strongly used are the 0^{th} and 1^{st} order shim terms. The 2^{nd} and 3^{rd} order shim terms were used in the *in vivo* experiments but not much in the phantom experiments. The higher order spatial complexity of the *in vivo* perturbations were not equally represented by all 2^{nd} and 3^{rd} order shim terms. ZY, Z2, ZX, Z2Y, Z3,

and Z3X are more represented than ZS2 for example. These shim terms were particularly solicited in the instructed motion experiments.

corrections		root mean square of the field in shim terms [Hz max 20]															
field control	motion correction	Z0	Y	Z	X	S2	ZY	Z2	ZX	C2	S3	ZS2	Z2Y	Z3	Z2X	ZC2	C3
phantom imaging																	
no	no	1.818	1.159	0.242	1.174	0.288	0.188	0.088	0.259	0.154	0.044	0.023	0.028	0.040	0.079	0.011	0.015
no	yes	2.117	1.155	0.380	1.449	0.294	0.219	0.081	0.228	0.119	0.034	0.022	0.015	0.071	0.094	0.011	0.034
yes	no	0.409	0.310	0.501	1.015	0.163	0.078	0.109	0.059	0.196	0.023	0.014	0.018	0.040	0.020	0.016	0.035
yes	yes	0.400	0.394	0.585	0.486	0.249	0.071	0.074	0.062	0.173	0.021	0.012	0.015	0.039	0.020	0.017	0.045
normal breathing																	
no	no	0.692	1.119	0.625	1.506	0.203	0.535	0.550	0.267	0.290	0.084	0.016	0.236	0.387	0.130	0.102	0.056
no	yes	1.085	0.891	1.392	0.815	0.494	0.222	0.479	0.315	0.128	0.102	0.092	0.160	0.454	0.299	0.088	0.150
yes	no	0.680	0.315	0.565	0.499	0.140	0.084	0.134	0.103	0.219	0.029	0.014	0.027	0.140	0.046	0.025	0.029
yes	yes	0.443	0.553	0.555	0.725	0.207	0.073	0.126	0.105	0.322	0.026	0.014	0.030	0.076	0.045	0.027	0.024
increased field perturbations																	
no	no	1.192	1.156	0.812	1.233	0.439	0.436	0.290	0.584	0.236	0.109	0.056	0.477	0.227	0.394	0.150	0.260
yes	yes	0.746	0.408	0.943	0.603	0.139	0.136	0.161	0.137	0.160	0.033	0.020	0.061	0.086	0.107	0.041	0.041
instructed motion																	
no	no	1.703	2.043	2.615	1.007	0.650	0.497	0.715	0.555	0.293	0.172	0.149	0.479	1.001	0.426	0.258	0.240
yes	yes	0.634	0.373	0.902	0.600	0.133	0.086	0.182	0.087	0.221	0.034	0.015	0.027	0.144	0.056	0.031	0.032

Table 4.2: Root-mean-square values of the field translated in shim terms for all imaging experiments in [HzMax20] notation.

4.4 Discussion

According to these results, the proposed strategy of simultaneous field and motion control is effective and robust. In particular, simultaneous control has been found to be stable although both feedback loops operate on the same physical quantities, i.e., the gradient fields. This indicates that the measures taken to decouple the two loops have been successful and not impeded by residual cross-talk.

Notably, robust operation has been accomplished without compromising the sensing precision in either loop. At ≤0.017mm and ≤0.015° the precision of translation and rotation sensing is competitive with Ref. (24,27), which report current NMR-based implementations of motion tracking alone. Likewise, with a field sensing precision of ≤ 0.472 Hz, our results are very similar to those reported in Ref. (3). At these levels of precision, propagation of residual measurement noise translates into hardly noticeable degradation according to our high-resolution phantom results. With sensing bandwidths of 20Hz for PMC and 10Hz for field control, adequate correction bandwidths of 20 Hz and about 0.27Hz, respectively, have been reached.

Simultaneous control has been shown to be effective in T2* imaging in vivo under normal and challenging conditions with increased field perturbation and head motion. Notably, in all circumstances dual correction yielded clearly superior image quality compared to either single correction. This implies that, for T2* imaging and related purposes such as SWI and QSM, advancing either type of correction alone faces diminishing returns.

The benefit from addressing both problems in concert will be most pronounced at high field, at high resolution, and in patients with difficulty to cooperate. One prominent realm of application will thus be high-field T2* scanning in studies of neurodegeneration.

While simultaneous control did prove to be stable, this study also illustrates that cross-talk does still occur. Specifically, geometry updates had slight effects on field control, indicating that rotation of gradients altered eddy-current and vibration effects that persist for some time after gradient switching. However, the PMC loop was not sensitive to shim operation by virtue of relying on high-frequency field dynamics. Therefore, field disturbances induced by geometry updates did not propagate back into the motion loop, preventing potential instability. For common head movements, the cross-talk effects were weak and in the noise range. Only for very large sequence rotations of +/-30°, the cross-talk effect became substantial. Still, even in this case field control brought the field back to baseline within one TR of 100ms. The existence of an interaction shows that the operation of the two loops is, as anticipated, more complex than the operation of the two single loops.

Eddy-current and vibration effects vary even without geometry updates, e.g., after variable phase-encoding and spoiler gradients. To avoid related confound, field measurement was performed between the readout and spoiler gradients. As stated in the methods section, the most generic choice would be to perform the field measurement at the echo time of the imaging sequence. This is conceptually straightforward but will require additional communication to adjust the target values of field control along with the scan geometry.

Motion sensing, on the other hand, while not affected by field control, was found to be subject to a minor source of error evident from the rigid-body parameters obtained in the phantom experiment. Small sudden shifts occurred when the phase encoding gradient changed sign. This indicates slightly different behavior of the gradient amplifiers depending on polarity, which however remains to be verified. At about 50 µm, the related error was small compared to the resolution and did not visibly affect imaging results. For even higher precision, motion tracking could be enhanced by real-time field tracking in the laboratory frame[150], which permits accounting for subtle changes in gradient output.

Settling behavior and correction bandwidth of a proportional integral controller are governed by the choice of proportional gain and integration time, the sensing bandwidth, and the plant's transfer function. Outside the control bandwidth, perturbations are not rejected and, just above the band limit, even amplified. Tuning of the field controller is hence a compromise between correction bandwidth and noise level. In our setup, sufficient bandwidth for suppressing effects of breathing and limb motion is achieved at only slight noise amplification (from 0.471Hz to 0.713Hz). Few remaining instances of fast perturbations, settling over few seconds (i.e., the inverse of the control bandwidth), did not noticeably impair image quality. The control bandwidth depends on latency, sensing bandwidth, and bandwidth of the shim system. To increase it, the most limiting of these factors should be improved. To reduce latency, computation and digital communication must be accelerated while higher-rate sensing can be achieved with field probes with faster recovery[151,152]. Generic ways of enhancing the shimming bandwidth are active shielding[153–155] and matrix pre-emphasis[156].

The motion correction loop used in this work is a simpler control system in that it relies on purely proportional feedback. At unit proportional gain it is not affected by constant offset and thus does not require an integral term and associated tuning. Proportional-integral control as used for field stabilization would reduce sensitivity to high-frequency perturbation at the expense of control bandwidth and thus be adequate only at higher rates of motion detection and update.

Unlike previous work tackling both motion and physiological field perturbation, the reported implementation deploys dynamic shimming up to 3rd order. Our results confirm the relevance of 2nd- and 3rd-order shimming for in vivo measurements as discussed in[2,121,136,141,157] (cf. Table 4.2). For field control with yet more spatial accuracy, both field sensing and field actuation will need to be advanced.

To advance sensing, one option is to use more accurate models of how field readouts at the probe positions relate to actual field patterns in the head. For perturbation due to breathing, this has been achieved with a learning approach based on dynamic B0 mapping along the respiratory cycle[121,158–160].

On the actuation side, spherical harmonic shimming up to third order has been found to be adequate in this work. More spatial diversity can be required in low regions of the brain that are closer to sources of perturbation such as the chest, shoulders, and arms[141]. To this end, the shim hardware should be optimized for related field patterns, demanding designs that deviate from traditional sets of spherical harmonics. The shim coils could be brought closer to the subject, increased in number, and tailored in terms of geometry. Promising advances in this direction have recently been reported[161–164].

Field control as performed in this work chiefly targets perturbations that originate from sources outside the head, using external means of field sensing and actuation. This approach is justified by fundamental magnetostatics, which state that the field in a source-free volume can be fully known and canceled by measurement and currents, respectively, on the surface. In this case, the relationship between sensing results and best shim settings is straightforward. With internal sources, external measurement and correction are intrinsically incomplete and best shim settings are harder to determine.

Internal sources can be of concern. For instance, due to its susceptibility the head itself is a source of magnetic field and thus causes field perturbation when it moves[165–167]. A prominent example is change in the orientation of the frontal sinuses, which modifies the field in the pre-frontal cortex. At 7T, this effect has been found to reach the order of 1.3 Hz per degree of rotation[166]. Movement of parts of the head such as swallowing likewise cause field variation[168].

In the present work, these effects were not found to be limiting. Larger perturbation from internal sources, e.g., upon extensive motion, could be addressed by dynamic B0 mapping, which effectively performs internal field sensing via NMR in the tissue. Such mapping could be performed in a navigator approach during actual imaging[2,56,148,157,169] or beforehand, in a learning phase that relates dynamic B0 maps to run-time readouts such as motion parameters[167] or readings from a breathing belt[121] or external field probes[159,170]. Alternatively, field perturbation by head motion could be estimated by calculating the field emanating from the head using a susceptibility model[171].

In this work, combined field and motion correction has been demonstrated for generic T2*-weighted spin-warp imaging but is not limited to this type of sequence. It should generally benefit all modes of head imaging and spectroscopy that are sensitive to off-resonance, especially those using gradient echoes with long echo time and/or long readouts. For implementation of the dual control loop the only requirement is suitable timing of the sensing intervals as detailed in the Methods section. According to measures 4&5 the field should be measured outside of sequence gradients and away from switching gradients, i.e., in a silent part of the sequence. This is often possible. A sufficient spacing from the last switching gradient should ensure that the effects of the eddy currents is small given the expected gradient amplitude changes caused by gradient stepping over time and sequence rotations.

Sequences that are too densely populated with gradient elements such as, e.g., steady-state approaches with minimal repetition time, will require field measurement to overlap with gradient operation. In this case, dual control will require perfect knowledge of the gradient behavior and, similarly to the case of field measurement at the echo time, adjustment of target values along with geometry update.

Simultaneous motion and field control can potentially be based on sensing methods other than those used in this work. For effective control, sensing should (i) support sufficient loop bandwidth by being itself suitably high-rate, (ii) be of sufficient precision, and (iii) capture the spatial complexity of field perturbations adequately.

Motion tracking could be performed with navigators[14–17,172] or optically[18–20,40–42] if suitable lines of sight are available. Optical methods offer ample

precision and bandwidth for the MRI application while navigators suffer from the need to trade-off precision, bandwidth, and scan time overhead. Within the realm of NMR-based tracking, viable alternatives include the use of dedicated tracking modules[26,44] or just native sequence elements[27], real-time field tracking in the laboratory frame[150], and other detection concepts such as inductive transmission of marker signals into the head coil[25,30].

Field control was initially proposed by Van Gelderen[121]. It was performed by learning the relationship between breathing depth and field changes in the head. At the time, this correction was implemented for field perturbation of up to second order but could be implemented for disturbances of higher order and be used in a dual control setup. Double-echo navigators[173,174] also have potential to serve as field sensing modality under the condition that field determination is accurate and rapid.

Dual control can hence be accomplished with a variety of implementations and has the potential to enhance neuroimaging in a large range of challenging research and clinical contexts.

Chapter 5

High-resolution T2*-weighted imaging of subcortical brain enhanced by motion and field compensation

Parts of this work were published in:

Aranovitch A.*, Vionnet L.*, Gross S., Dietrich B.E., Kasper L., Wilm B., Schmid T., Brunner D.O., Pruessmann K.P., *High-resolution T2*-weighted imaging of subcortical brain enhanced by motion and field compensation*, Joint Annual Meeting ISMRM-ESMRMB 2018, Paris, France, 2018.

*authors with equal contribution

Manuscript in preparation

5.1 Introduction

Neuroimaging at ultra-high field (UHF) holds the prospect of depicting brain structures in-vivo with unprecedented clarity[175]. Changes and abnormalities in the cerebral cortex and subcortical brain are known to be associated with neurologic disease and disorder, such as Huntington's disease (HD), Alzheimer's disease (AD) or Parkinson's disease (PD). A variety of structures have reportedly been used as indicators to detect and characterize neurodegenerative diseases, including the basal ganglia[176,177], the hippocampus[178], the brainstem and cortical structures[179]. Visualizing intra-cortical contrast variations and the large amount of small subcortical brain structures and their nuclei demands a high image resolution, which is facilitated by the SNR advantage of UHF.

Along with image resolution, image contrast plays a key role in obtaining useful anatomical information. A recent review regarding the visualization of the human subcortex at UHF found that T2* based scans were employed most often to visualize structures such as the thalamus or the subthalamic nucleus and can thus be considered one of the most sought-after contrasts at UHF[36]. The importance of T2* based contrasts is further underlined by comparative studies performed at UHF for imaging of the basal ganglia and their subdivisions[180]. The appeal of T2* weighted imaging and its derived contrasts, such as susceptibility weighted imaging (SWI) or quantitative susceptibility mapping (QSM), stems from its sensitivity to local field changes. These are caused by susceptibility variations in liquids or tissues, e.g. due to differences in oxygenation levels or iron and myelin content.

Therefore, high-resolution T2*-based scans for visualizing deep brain structures at UHF have great potential for applications in neuroimaging. However, such scans come with a number of challenges. For sufficient SNR, high-resolution scans tend to have an extended scan duration which generally increases the amount of involuntary subject motion, including rigid-body head motion that may hamper high-resolution imaging. Moreover, due to their long echo times T2* based scans are sensitive to field fluctuations, such as those caused by subject breathing[120,121] or limb motion. The resulting image artefacts, including ghosting and signal dropout, are exacerbated at UHF and particularly severe in caudal parts of the brain which are closer to the sources of field perturbation.

A range of methods has been devised to address these issues. Head tracking data obtained via dedicated hardware or through navigators may be used to correct for rigid-body head motion retrospectively[17] or prospectively[12,18,26]. Established motion correction methods have been applied to brain MRI with highest resolutions and extended scan durations, and their potential to obtain datasets rich in anatomic detail has been demonstrated[53,54,181,182]. Field compensation methods, on the other hand, can be used to correct for zeroth or even higher-order field fluctuations retrospectively[60,183] or prospectively[3,121,140]. The utility of a prospective correction approach with up to third-order shim updates has been demonstrated by Duerst et al[141] and was found to be beneficial for T2* mapping[142] and quantitative susceptibility mapping[143].

Recent methodological advances aimed at fostering high-resolution T2*-weighted scans by simultaneously correcting for rigid-body head motion as well as field fluctuations[15,134,184]. One such approach combined two

prospective correction methods based on NMR sensors, each of which offers state-of-the-art performance in its individual correction task[184]. A stable co-operation of these two real-time control systems actuating the magnetic fields and deriving their inputs from the fields they actuate has been verified and no significant compromise of the performance in the individual correction mechanisms was detected. This combined approach corrected for complementary effects of motion and field fluctuations and provided promising initial results of the upper brain at a resolution of 0.4 mm. Moreover, the dual correction approach is synergistic in that the benefit of motion correction, which includes the robust depiction of tiny structures, could easily be compromised by cloud-like artefacts stemming from field fluctuations, if not corrected for.

Since this dual control scheme allows to carry out scans without the impairment of head motion or field fluctuations, it is possible to transition to long MRI scans with high resolution and SNR, where these effects tend to be particularly confounding factors. Thus, the purpose of the present work is to explore the image quality obtainable at 7T by applying this combined correction approach. One-hour highest-resolution T2* weighted brain scans (0.25 mm x 0.25 mm x 1 mm) were carried out in challenging regions such as subcortical brain and the brainstem. Notable structures in the basal ganglia, the midbrain or the thalamus were identified and other structures of interest for a range of neurological conditions were highlighted.

5.2 Methods

5.2.1 Hardware

All experiments were performed on a 7T Philips Achieva system (Philips Healthcare, Best, The Netherlands) using a 32-channel head receive array (Nova Medical, Wilmington, Massachusetts, USA). A total of 20 NMR field sensors[31] based on ^{19}F were operated using a stand-alone acquisition system[33]. For motion tracking, four sensors (T1 = 2.1 ms, droplet diameter = 1.3 mm) were head-mounted using a 3D-printed headset. For field control, 16 sensors (T1 = 86 ms, droplet diameter = 0.8 mm) were rigidly attached to a laser-sintered frame accommodated in between the transmit and receiver array.

A third-order spherical harmonic shim system was available on the host MR system, consisting of a zeroth-order, five second-order and seven third-order shim coils (Philips Healthcare, Best, The Netherlands). The corresponding shim amplifiers were controlled with analog input voltages. First-order shims were controlled with a custom-built gradient override unit that enabled to apply additional voltage demand[3].

5.2.2 Data acquisition & processing

To explore different brain regions depicted in various orientation, five one-hour 2D GRE scans were carried out. Each scan consisted of five averages that were realigned prior to averaging using a Matlab (MathWorks, Natick, MA, USA) routine. The detailed scan parameters and scan planning are provided in Figure 5.1. An experienced and healthy volunteer was scanned according to the applicable ethics. Apart from a foam to lie on, no additional padding was used. The scans were performed in separate sessions and on different days.

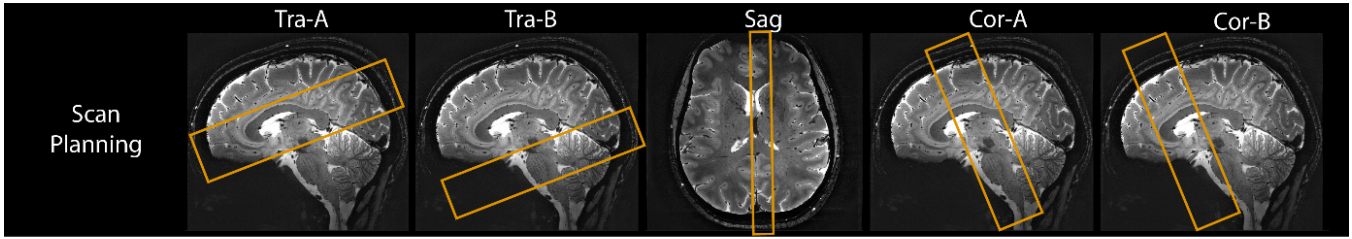

Orientation	Transversal	Transversal	Sagittal	Coronal	Coronal
Resolution	0.25 x 0.25 x 1 mm^3	0.25 x 0.25 x 1.2 mm^3	0.25 x 0.25 x 1 mm^3	0.25 x 0.25 x 1 mm^3	0.25 x 0.25 x 1 mm^3
Slice gap	1 mm	0.5 mm	0 mm	1 mm	1 mm
FOV (ap, fh, rl)	[210 39 190] mm	[210 33.50 190] mm	[190 210 20] mm	[39 210 190] mm	[39 210 190] mm
TE/TR/Flip angle	25 ms / 950 ms / 50°				
Slices	20				
Averages	5				
Bandwidth	91.4 Hz/px				
Scan duration	1 hour				

Figure 5.1: A total of five one-hour scans was performed with sequence parameters as shown in the figure. The top row indicates the scan planning for every acquisition, which was chosen such as to cover cortical and subcortical brain regions.

5.2.3 Simultaneous PMC and field control

Simultaneous PMC and field control was implemented as described and characterized with respect to stable operation in Ref. ([184]). Figure 5.2a illustrates a schematic of the two control loops based on two sets of NMR sensors. Their FID measurements during a dedicated position and field sensing module were used to derive the inputs for both loops. These sensing modules were inserted consecutively after the readout gradient as illustrated in Figure 5.2b. The position sensing module contained a sinusoidal gradient on every axis to encode the position of the sensors[24] (amplitude = 7 mT/m, duration = 1 ms, frequencies = [2, 3, 4] kHz). The field sensing module consisted of a block without any gradient activity (duration = 2.8 ms) during which the 16 sensors used for field control performed a magnetic field measurement. Due to the different relaxation times of the two sensor sets, the PMC loop was operated every TR, i.e. at an update rate of 47.5 ms, while excitation and signal acquisition of the sensors in the feedback loop was performed every other TR, i.e. every 95 ms.

To obtain head tracking data for PMC geometry updates, four NMR field probes were head-mounted using a 3D-printed headset. Their positions were calculated via the formula in Ref. (27)

$$\boldsymbol{r} = (\boldsymbol{F}\boldsymbol{G})^{+}\boldsymbol{F}(\gamma^{-1}\boldsymbol{D}\boldsymbol{\phi} - \boldsymbol{g}_0),$$

where $\boldsymbol{\phi}$ is the measured phase time course of a marker, $\boldsymbol{G} = [\boldsymbol{g_x}, \boldsymbol{g_y}, \boldsymbol{g_z}]$ and $\boldsymbol{g}_0$ denote the three linear and one homogeneous field component obtained by preceding calibration, $\boldsymbol{F}$ is a filter for separating the sinusoidal frequencies used for position encoding, $\boldsymbol{D}$ is a

first-order difference operator and γ the gyromagnetic ratio of the NMR-active sample of the sensors.

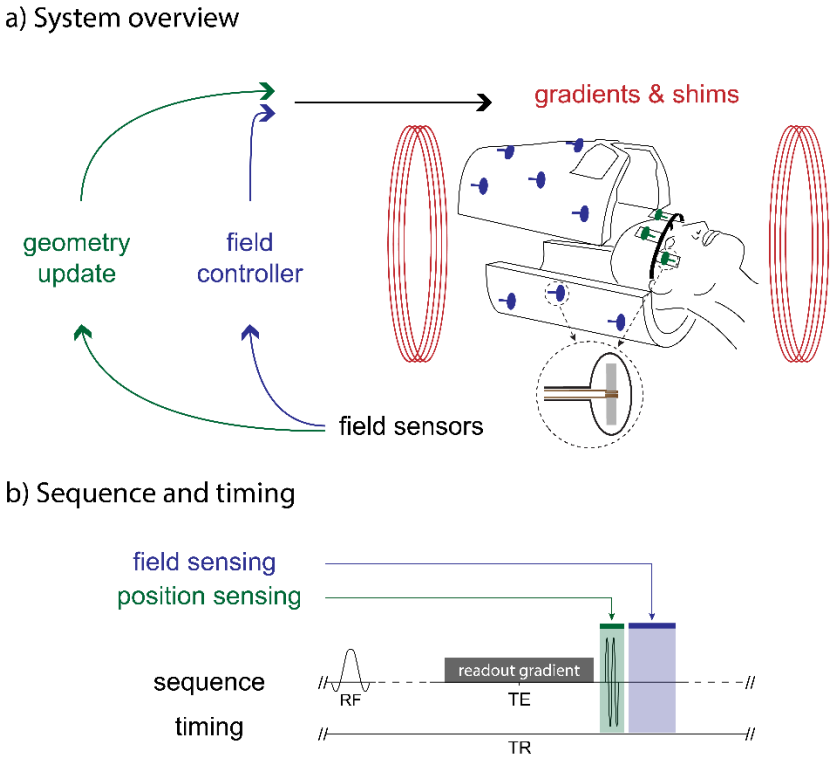

Figure 5.2: a) A schematic of the experimental setup along with the two control loops for prospective motion correction and field control. Head-mounted field sensors (green) are used to perform head tracking and yield corresponding rigid-body parameters that are used for scan geometry updates. Stationary field sensors (blue) distributed around the receiver array perform field measurements that serve as input for the controller which determines the demanded shim update to maintain a baseline field. b) A position and a field sensing module were inserted after the readout gradient. The 1 ms position sensing module contained a sinusoidal gradient on every axis to spatially encode the head-

mounted sensors, whereas the 2.8 ms field sensing module contained no gradient activity.

To compute the rigid-body transformation between the sensor positions at each time point of measurement relative to their position at the beginning of each scan, the method of Umeyama was used[47]. The resulting rotation matrix and translation vector used for PMC geometry updates were sent to the scanner host via TCP using a vendor-provided external communication interface[46].

For real-time field control, the 16 NMR sensors placed in between the transmit and receive arrays performed field measurements and a proportional-integral controller determined the shim voltages with the goal to maintain the field at a reference baseline[3]. The demanded correction field at time t, $\boldsymbol{B}_{\mathrm{corr}}(t)$, was determined using the formula $\boldsymbol{B}_{\mathrm{corr}}(t) = K_p\left(\boldsymbol{e}(t) + \frac{1}{T_i}\int_0^t \boldsymbol{e}(\tau)d\tau\right)$ where $\boldsymbol{e}(t) = \boldsymbol{B}_{target}(t=0) - \boldsymbol{B}_{total}(t)$ is an error term denoting the difference between the targeted baseline magnetic field at $t = 0$ and the current total field as determined using the field probes. K_p and T_i are proportional and integral constants that influence the stability and rejection bandwidth of the loop. They were set to $K_p = 0.27$ and $T_i = 0.07\ s$, as in Ref. ([184]). The voltages controlling the shim coils were then computed by $\boldsymbol{u}(t) = \boldsymbol{C}^{+}\boldsymbol{B}_{\mathrm{corr}}(t)$, where $\boldsymbol{C}^{+}$ denotes the Moore-Penrose pseudo-inverse of matrix $\boldsymbol{C}$, whose entries C_{ij} are obtained in a preceding calibration and represent the static field change measured by the i-th field probe resulting from applying unit voltage to the j-th shim channel.

The individual applications performing signal processing for PMC and field control were programmed in LabView (National Instruments, Houston, Texas, USA).

5.2.4 Data labelling

A set of regions and structures was compiled that are of interest for a range of neurological conditions. These regions included the basal ganglia, the thalamus, the brainstem (midbrain, pons, medulla oblongata), cortex, white matter structures, the hippocampus, the cerebellum and the trigeminal nerve. The basal ganglia, the thalamus and the brainstem were annotated and parcellated using a range of anatomical atlases[185–188] and scientific publications. During this process the window levels were adjusted freely to emphasize individual structures.

5.3 Results

5.3.1 Motion and field traces

Recordings of the rigid-body parameters and the applied field corrections were available at a rate of approximately 20 Hz and 10 Hz, respectively, throughout the full scan duration. The entire recordings are visualized in Figure 5.3. Head motion of up to 3 mm and 2 degrees occurred during the scans. The applied correction on the individual shim channels, including 0^{th}, 1^{st}, 2^{nd} and 3^{rd} order shim terms, is shown in "HzMax20" notation, which represents the field changes occurring on the surface of a sphere with a diameter of 20 cm around the isocenter. Various trends are visible in the curves. Most notably, the Y channel in the transversal and coronal scan, and the X channel of the sagittal scan exhibit a sawtooth shape, which reflects gradient stepping during each

of the five averages. This is likely due to induced eddy-currents that cause subtle field changes at the time points when the field measurements for the feedback loop are performed. Moreover, the curves exhibit drifts that correlate with the rigid-body parameters, particularly in the higher orders, which is a result of field changes induced by head motion.

A one-minute snippet from the first transversal scan provides a zoomed view (Figure 5.3, bottom) and shows the breathing-induced fluctuations for one representative shim channel from every order and the corresponding rigid-body motion parameters. The peak-to-peak values within a breathing cycle are about 2 Hz for the zeroth order and first-order x channel, and about 0.5 Hz for the Z2 and Z2X term, respectively. The breathing motion is also visible in the rigid-body parameters, specifically in translation along FH and rotation about RL.

5.3.2 Overview

To provide an impression of the obtained dataset, exemplary slices are depicted in Figure 5.4. The images are free of conspicuous motion or breathing-related artefacts and exhibit a high quality throughout. Vessels and veins appear sharp and also lower brain regions are robustly depicted, which is particularly visible in the sagittal and coronal slices. Slight signal loss is visible in the transversal slices towards the sinuses which cannot be avoided, but does not impede the assessment of relevant regions. In the following, zoomed images of several brain regions and structures will be presented in greater detail.

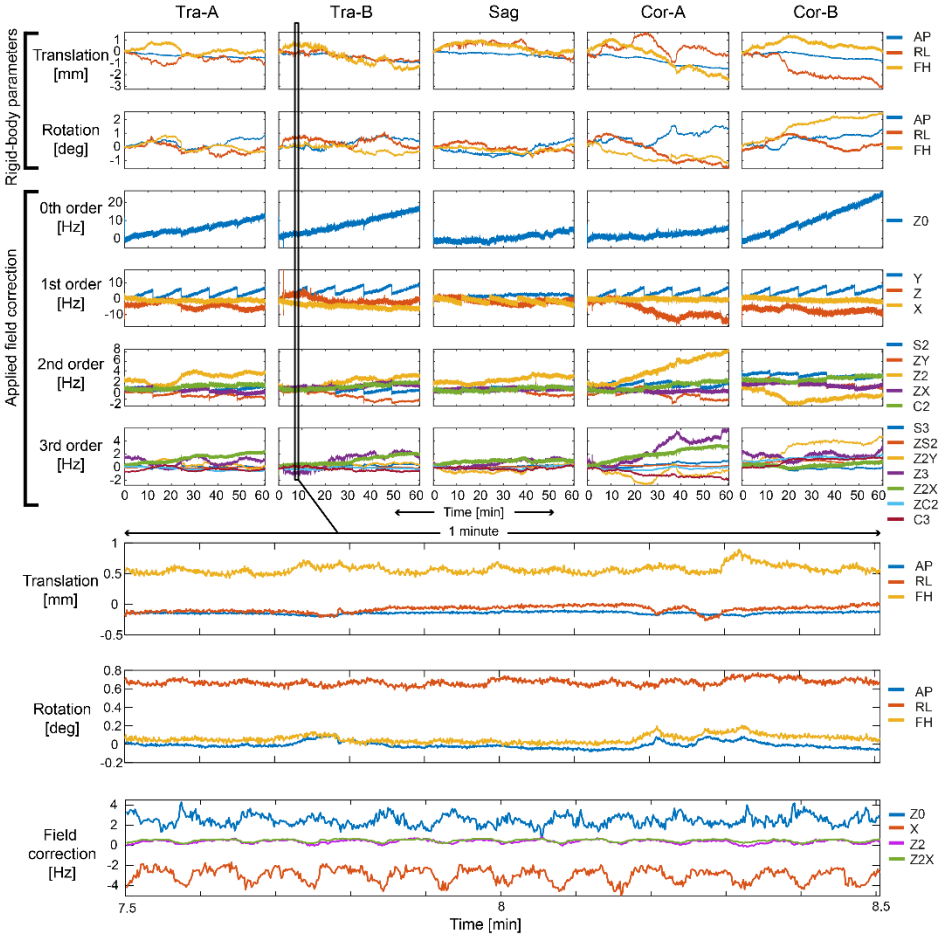

Figure 5.3: The entire set of recorded rigid-body parameters and applied field corrections performed during all scans. The applied field corrections are plotted for every order and given in "HzMax20" notation, which describes the field change induced by the respective shim term on the surface of an imaginary sphere around the isocenter with a diameter of 20 cm. A zoomed view shows a one-minute snippet from scan "Tra-A" to highlight breathing-related dynamics.

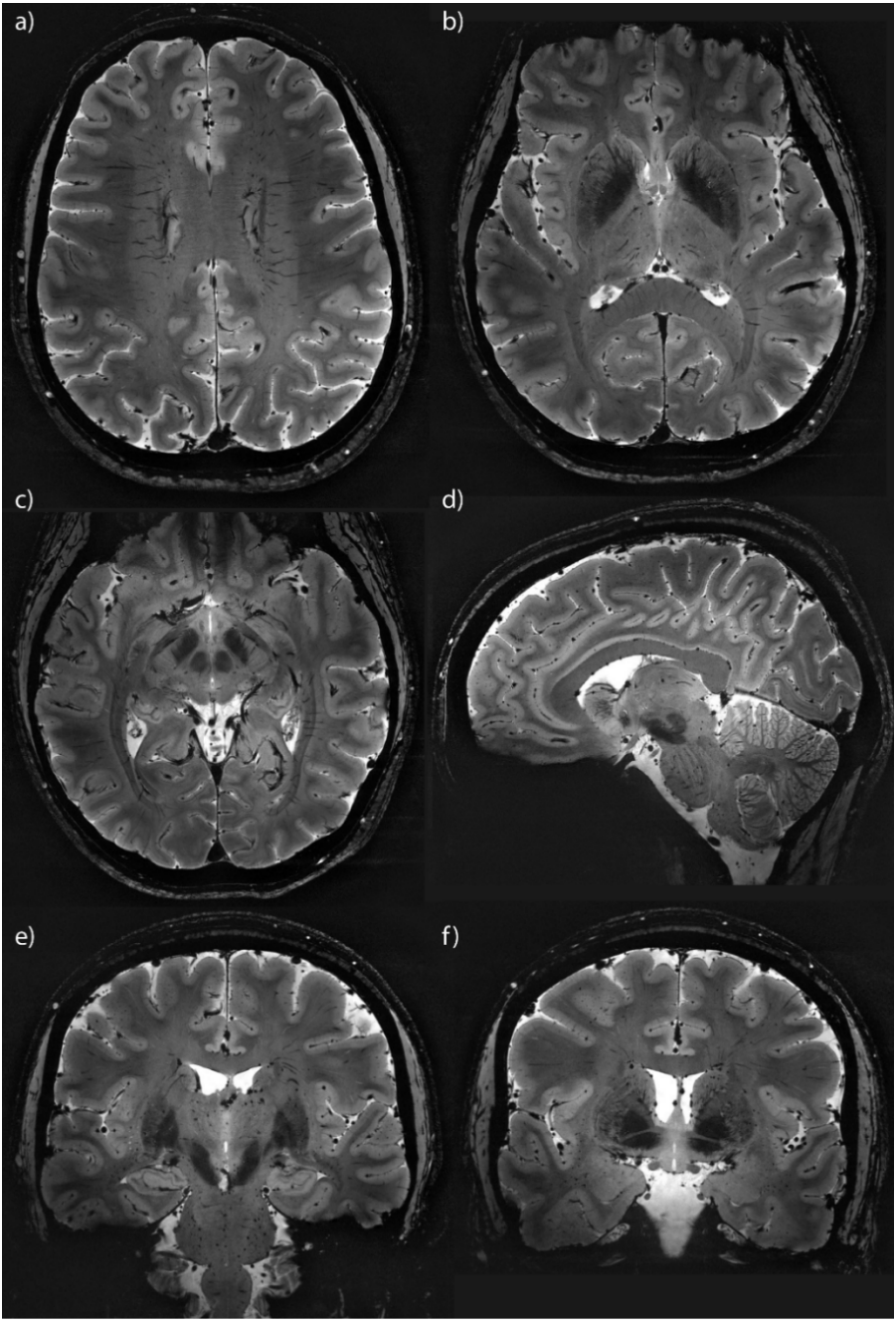
a)
b)
c)
d)
e)
f)

Figure 5.4: Exemplary slices from the acquired dataset. a, b, c) from "Tra-A", (d) from "Sag", (e) from "Cor-1", (f) from "Cor-2", cf. Figure 5.1. The slices exhibit a high image quality, including lower regions such as the brainstem. Tiny vessels and veins are depicted sharply and a large amount of structural details is visible throughout.

5.3.3 Anatomical regions

5.3.3.1 Basal Ganglia and Thalamus

Figure 5.5 shows representative slices depicting axial and coronal zoomed sections of the basal ganglia region along with the thalamus. The substructure of the globus pallidus can be discerned and closely matches plate 27 in the Schaltenbrandt atlas (Figure 5.5a). Specifically, the pallidum laterale, pallidum mediale externum and pallidum mediale internum, separated by the lamina pallidi medialis and lamina pallidi incompleta can be seen. The head of the caudate nucleus can also be detected. Moreover, the subthalamic nucleus and the substantia nigra are visible and can be delineated from surrounding gray and white matter in Figure 5.5a,b. At the given T2* weighting, both structures exhibit a low signal intensity, but may still be distinguished from each other since the subthalamic nucleus has slightly higher signal intensity. Figure 5.5b shows a coronal slice located ventrally. It displays structures in an area cranial to the subthalamic nucleus that are typically referred to as fields of Forel (H1, H2) and the zona incerta. This region was labelled and parcellated according to plate 27 in the Schaltenbrandt atlas.

Figure 5.5c contains an axial view of the basal ganglia and thalamus region. The vascular structure inside the putamen is depicted in fine detail and in close agreement to histological images (e.g. Schaltenbrandt plate 17). The basal ganglia structures were labelled according to plate

54 in the Schaltenbrandt atlas. Note that the angulation of the transversal slices in the dataset slightly differs from the orientation in anatomical atlases in that it is moderately tilted around the right-left axis. Therefore, structures located anteriorly on a slice in the dataset tend to appear in lower slices of the atlases. The anterior commissure and the column of fornix are prominently displayed and the caudate nucleus is demarcated by the anterior limb of the internal capsule. The division of the globus pallidus into an internal and external part is less pronounced than in the coronal view (Figure 5.5a), however, the lamina pallidi medialis separating the two is still visible.

The thalamus consists of a multitude of adjacent nuclei some of which can be discerned in Figure 5.5c and d. The suggested parcellation was performed in agreement with plate 53 from the Schaltenbrandt atlas and was guided by contrast variations in tissue and symmetries between the two brain hemispheres. The pulvinar's division into a lateral and medial part is visible on both slices along with several nuclei from the ventral nuclear group.

The claustrum is visible between the capsula externa and capsula extrema (Figure 5.5b,c).

Figure 5.5d exhibits fine tubular structures running from the subthalamic nucleus to the internal globus pallidus and traversing the posterior limb of the internal capsule. Such structures have been observed previously and likely constitute pallidofugal fibers[189].

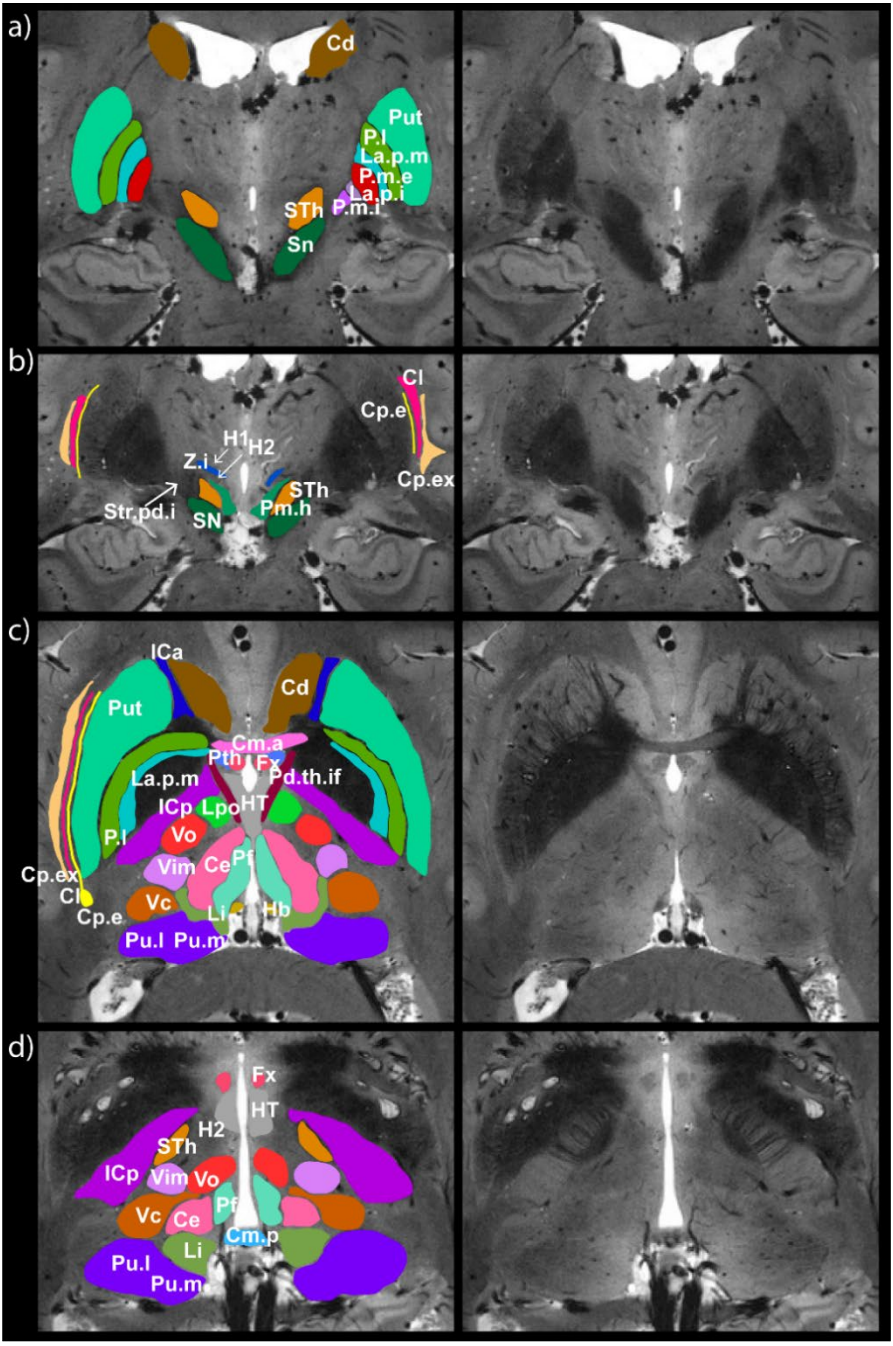
a)
Cd
Put
P.l
La.p.m
P.m.e
La.p.i
STh
P.m.l
Sn
b)
Cl
Cp.e
H1
H2
Z.i
STh
Cp.ex
Str.pd.i
SN
P.m.h
c)
ICa
Cd
Put
Cm.a
Pth
Fx
La.p.m
Pd.th.if
ICp
Lpo
HT
P.l
Vo
Vim
Ce
Pf
Cp.ex
Cl
Vc
Li
Hb
Cp.e
Pu.l
Pu.m
d)
Fx
HT
H2
STh
ICp
Vim
Vo
Pf
Vc
Ce
Cm.p
Li
Pu.l
Pu.m

Figure 5.5: Coronal (a, b) and transversal (c, d) cross sections of the basal ganglia and thalamus. Put: putamen, P.l: pallidum laterale, La.p.m: lamina pallidi medialis, P.m.e: pallidum mediale externum, La.p.i: lamina pallidi incompleta, P.m.i: pallidum mediale internum, STh: subthalamic nucleus, SN: substantia nigra, Cd: caudate nucleus, Cp.ex: capsula extrema, Cl: claustrum, Cp.e: capsula externa, Str.pd.i: striae pedunculi interni, Pm.h: nucleus postmammillaris hypothalamic, ICa: anterior limb of internal capsule, ICp: posterior limb of internal capsule, Cm.a: anterior commissure, Cm.p: posterior commissure, Hb: habenula, Fx: fornix, Pth: prothalamus, HT: hypothalamus, Z.i.: zona incerta, H1: field of Forel, H2: field of Forel, Vim: nuclei ventrointermedii, Vo: nuclei ventroorales, Vc: nuclei ventrocaudales, Ce: nuclei centrales thalami, Li: nucleus limitans thalami, Pf: nucleus parafascicularis thalami, Pu.l: pulvinar laterale, Pu.m: pulvinar mediale.

5.3.3.2 Midbrain

Figure 5.6 shows the variety of structures located in the midbrain. Substructure within the red nucleus can be identified in transversal and sagittal views (Figure 5.6a,c). Its devision was parcellated according to Olszewski and Baxter's atlas (p. 272/273). The medullary lamella can be discerned as a slightly hyperintense structure, dividing the red nucleus into pars oralis, pars dorsomedialis and pars caudalis.

The substantia nigra can be delimited from surrounding structures and a moderate contrast variation within the substantia nigra is visible in Figure 5.6b and d, showing the pars compacta and pars reticulata.

The mammillary bodies are visible on Figure 5.6b-d. The column of fornix and the mammilothalamic tract are depicted in Figure 5.6a and c. Figure 5.6c shows a sagittal slice, which was parcellated according to plate 37 in the Schaltenbrandt atlas, that reveals the course of the body and the

column of fornix as it ends in the mammillary bodies. In the posterior part, the superior and inferior colliculi are shown along with the habenula. Moreover, structures including the superior colliculus, the lateral and medial lemniscus, lateral and medial geniculate bodies are parcellated on transversal slices (Figure 5.6a,b) based on pages 42-49 in von Hagen's atlas, and plates 32-42 in Olszewski and Baxter's atlas.

The cerebellar peduncle is visible across all transversal slices in Figure 5.6 and the interpeduncular nucleus can be seen in the caudal part of the midbrain (von Hagen's atlas, p. 71).

Another symmetric arc-shaped contrast variation occurs between the red nuclei on Figure 5.6d and is highlighted by a dashed line. According to plate 38 in Olszewski and Baxter's atlas this could be a plausible shape and location of a nuclei group consisting of the oculomotor nucleus, the Edinger-Westphal nucleus and the interstitial nucleus of Cajal.

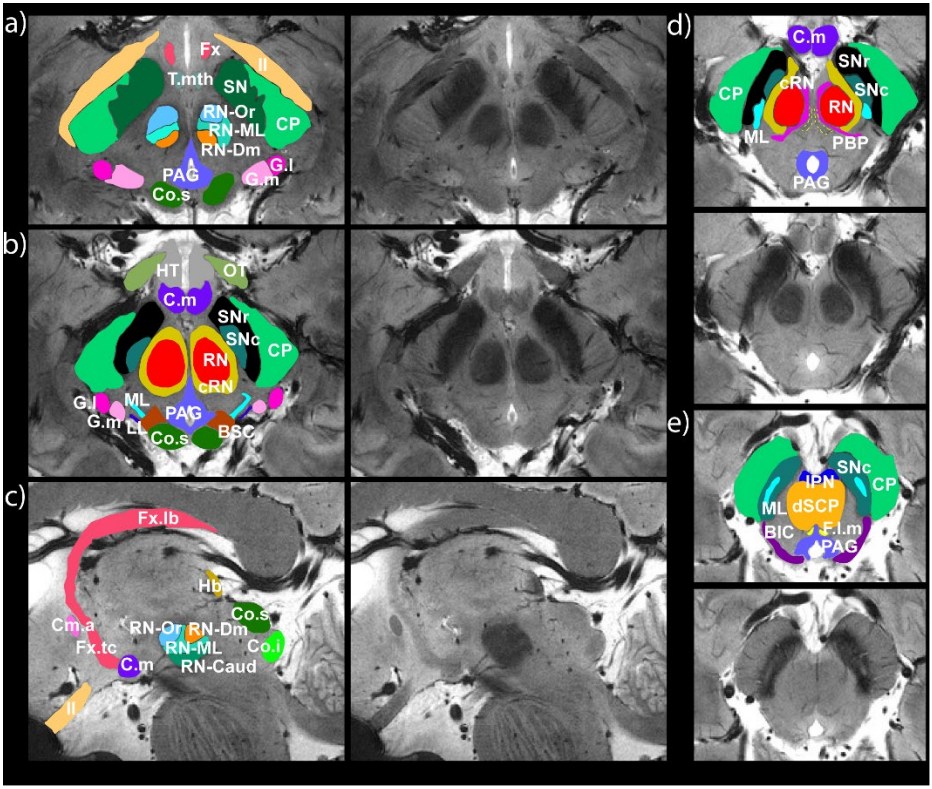

Figure 5.6: Detailed view of the midbrain in transversal and sagittal cross sections. C.m: mammillary bodies, T.mth: mammillothalamic tract, RN: red nucleus, RN-Or: red nucleus pars oralis, RN-Dm: red nucleus pars dorsomedialis, RN-Caud: red nucleus pars caudalis, RN-ML: medullary lamella of red nucleus, cRN: capsula of red nucleus, HT: hypothalamus, SN: substantia nigra, SNc: substantia nigra pars compacta, SNr: substantia nigra pars reticulate, CP: cerebellar peduncle, Cm.a: anterior commissure, OT: optic tract, PAG: periaqueductal gray, Hb: habenula, Co.s: superior colliculus, Co.i: inferior colliculus, ML: medial lemniscus, LL: lateral lemniscus, dSCP: decussation of superior cerebellar peduncle, PBP: parabrachial pigmented nucleus, IPN: interpeduncular nucleus, F.l.m: medial

longitudinal fasciculus, BSC: brachium of superior colliculus, BIC: brachium of inferior colliculus, G.l: lateral geniculate body, G.m: medial geniculate body, II: optic nerve, Fx.lb: fornix pars libera, Fx.tc: fornix pars tecta.

5.3.3.3 Pons and medulla

Two transversal and two sagittal sections through the pons and medulla are shown in Figure 5.7. Within the pons, two different types of fiber bundles can be discerned. Transverse pontine fibers running in medial-lateral direction (hypointense) that are associated with pontine nuclei. Also, fiber bundles aligned in superior-inferior direction are visible on the sagittal sections (hyperintense) and constitute various longitudinal tracts, such as the corticospinal or corticobulbar tracts.

The medial longitudinal fasciculus is demarcated in the transversal sections (Figure 5.7a,b) and the sagittal section shows its ascending course along the brainstem, ventral to periaqueductal gray matter (Figure 5.7d). Moreover, the superior cerebellar peduncle (Figure 5.7b) and the decussation of the superior cerebellar peduncle (Figure 5.7d) are visible.

The reticulotegmental nucleus is marked on Figure 5.7a according to Ref. (190), page 334.

Subtle hypointense spots are contoured with dashed lines (Figure 5.7a,b) that constitute various tracts, one of which is likely the central tegmental tract. The inferior olive is visible within the medulla oblongata (Figure 5.7c).

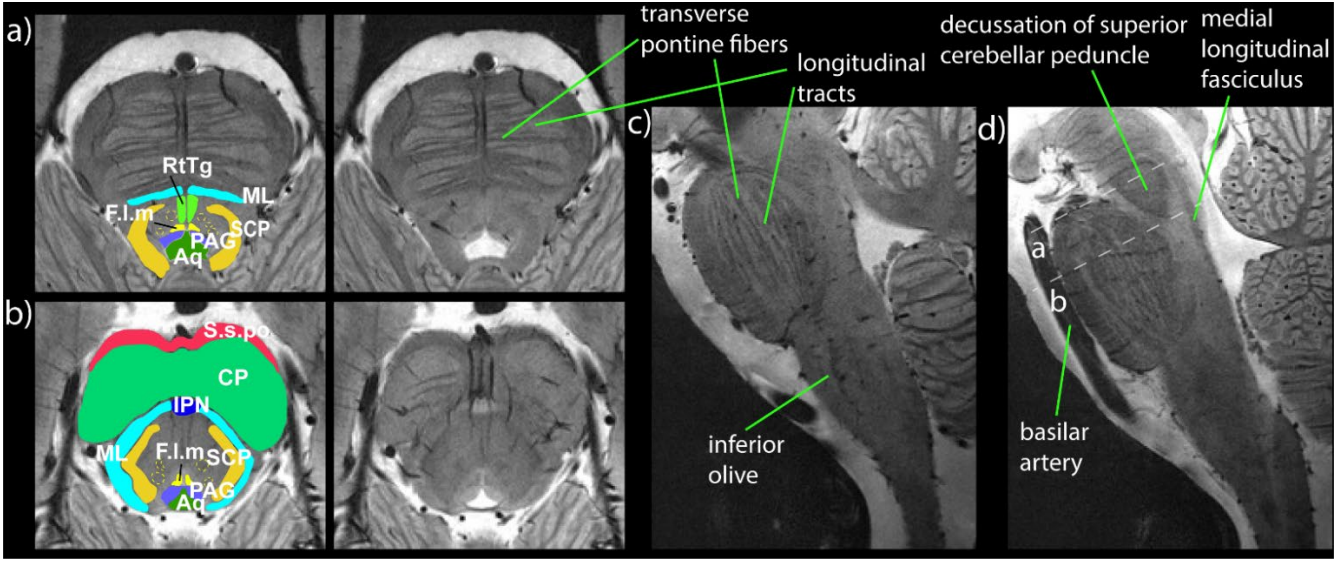

Figure 5.7: Zoomed view on transversal and sagittal slices depicting the pons and medulla oblongtata. F.l.m: medial longitudinal fasciculus, CP: cerebellar peduncle, Aq: aqueduct, PAG: periaqueductal gray, IPN: interpeduncular nucleus, ML: medial lemniscus, RtTg: reticulotegmental nucleus, SCP: superior cerebellar peduncle, S.s.po: striatum superficiale pontis.

5.3.3.4 Other structures

Figure 5.8 displays zoomed sections to emphasize different features visible within white matter. Figure 5.8a shows a large amount of tiny blood vessels in mediolateral direction along with striatal bridges. Figure 5.8b,c present magnified sections of the corpus callosum in axial and sagittal view. The fibrous microstructure of the corpus callosum is revealed directly on these magnitude images. Moreover, small white spaces commonly referred to as Virchow-Robin-spaces can be seen in Figure 5.8d.

Several examples of contrast within cortical grey matter are highlighted in Figure 5.9. A laminar contrast variation of up to three sectors can be observed throughout the brain. Figure 5.9a demonstrates an example of three laminar regions, a hypointense one between two hyperintense ones, while Figure 5.9b shows a gyrus containing two regions, a hyperintense and a hypointense one. This laminar contrast variation likely reflects cortical layers, as intracortical R2* contrast was mostly attributed to layer-specific variations of iron content, as reported through post-mortem MRI, histological staining and electron microscopy[191]. In the occipital lobe, the stria of gennari exhibits a particularly strong contrast on these heavily T2* weighted images. Its fine structure is accurately delineated on both the sagittal and the transversal views (Figure 5.9c,d).

Figure 5.10a shows successive coronal slices with zoomed sections of the hippocampus, ordered in anterior-to-posterior direction. Starting with the head of the hippocampus, the narrowing of its body can be tracked towards posterior slices. The three cortical convolutions known as digitationes hippocampi are clearly displayed in the first column. The

folding of the cornu ammonis can be seen in the second and third column. Figure 5.10b shows an axial view of the amygdala on both the right and left brain hemispheres.

Figure 5.11 displays coronal sections through the cerebellum, showing the two hemispheres and the middle zone called the vermis. Individual lobules and fissures can be detected and the tight folding of the cerebellar cortex around the interior white matter of the cerebellum is visualized. The dentate nucleus is discernable within white matter, appearing as a strongly hypointense structure. The superior and inferior colliculi located cranially to the cerebellum are visible in Figure 5.11a.

The trigeminal nerve (fifth cranial nerve) and its surrounding structures are shown in three different sections in Figure 5.12. Specifically, the trigeminal ganglion within the Meckel cave is shown in all three orientations (arrows). Black dots are clearly discernable within the ganglion in the coronal section (Figure 5.12a), that likely constitute separate nerve bundles. Figure 5.12b shows the trigeminal nerve emerging from the lateral pons and its cisternal segment can be seen as it traverses the prepontine cistern.

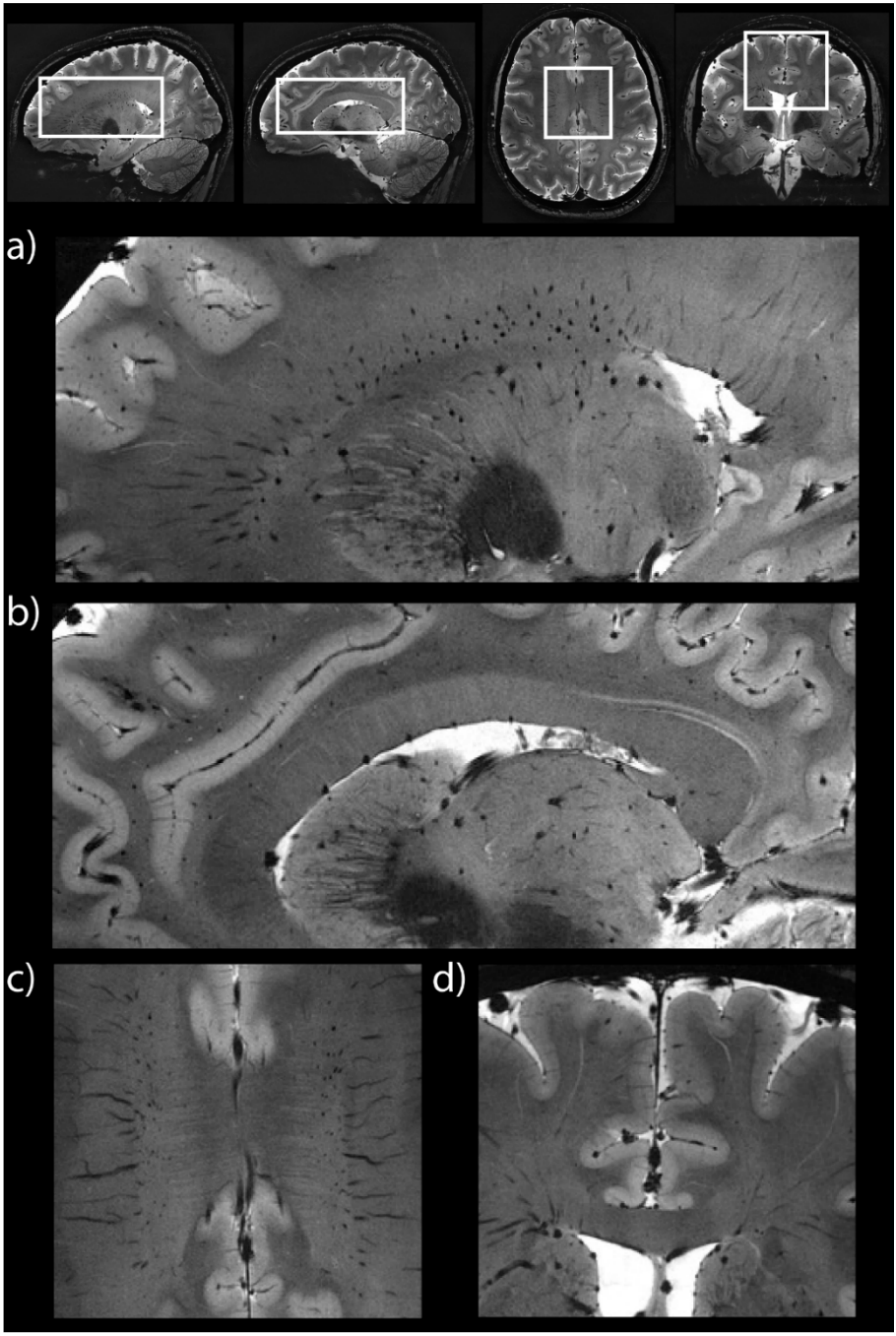
a)
b)
c)
d)

Figure 5.8: Zoomed section to highlight different areas within white matter. a) a large amount of vessels and striatal bridges is visible. b,c) the fibrous structure of the corpus callosum is directly revealed. d) small white spaces are visible that are referred to as Virchow-Robin spaces.

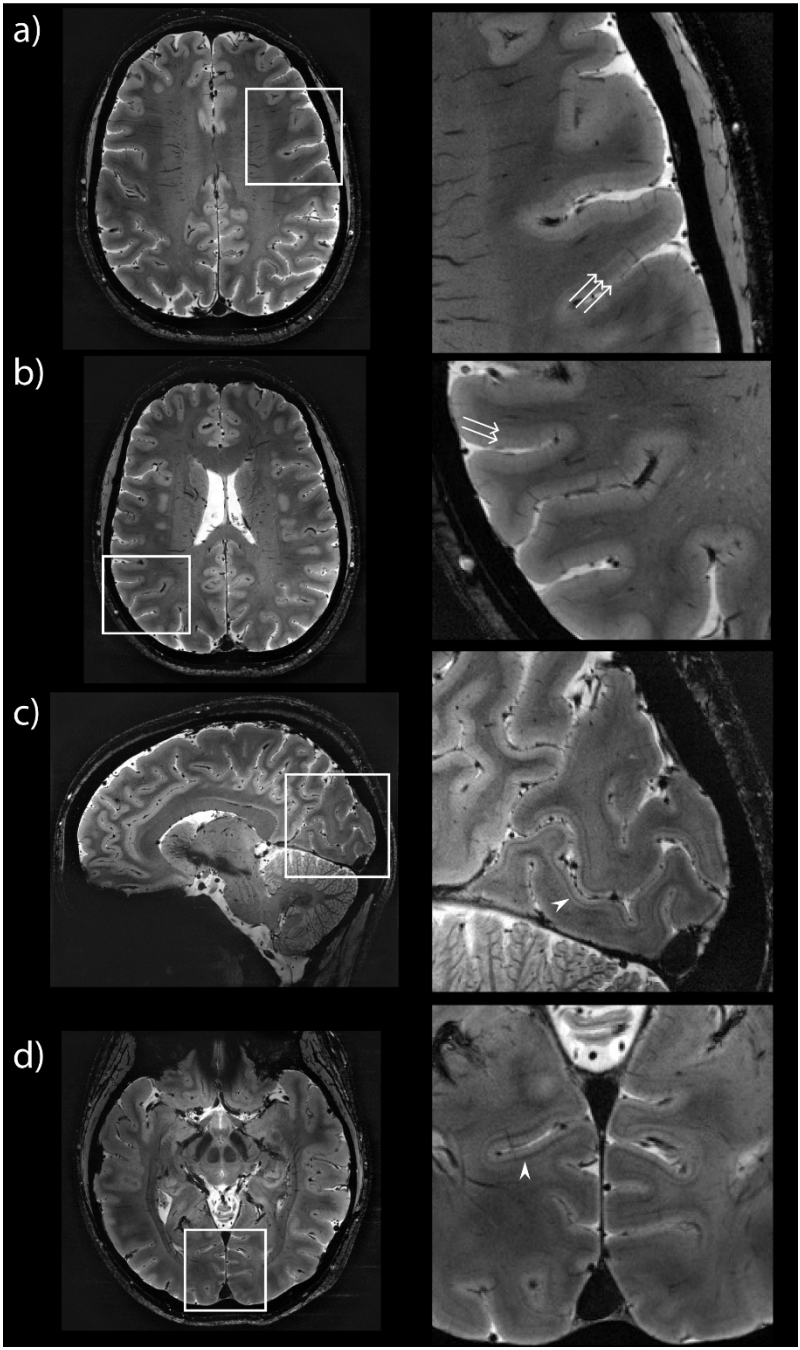
a)
b)
c)
d)

Figure 5.9: Examples of intracortical contrast in various parts of the brain. a,b) a laminar contrast variation is visible within cortical grey matter (arrows). c,d) the stria of gennari is accurately depicted in the occipital lobe (arrow heads).

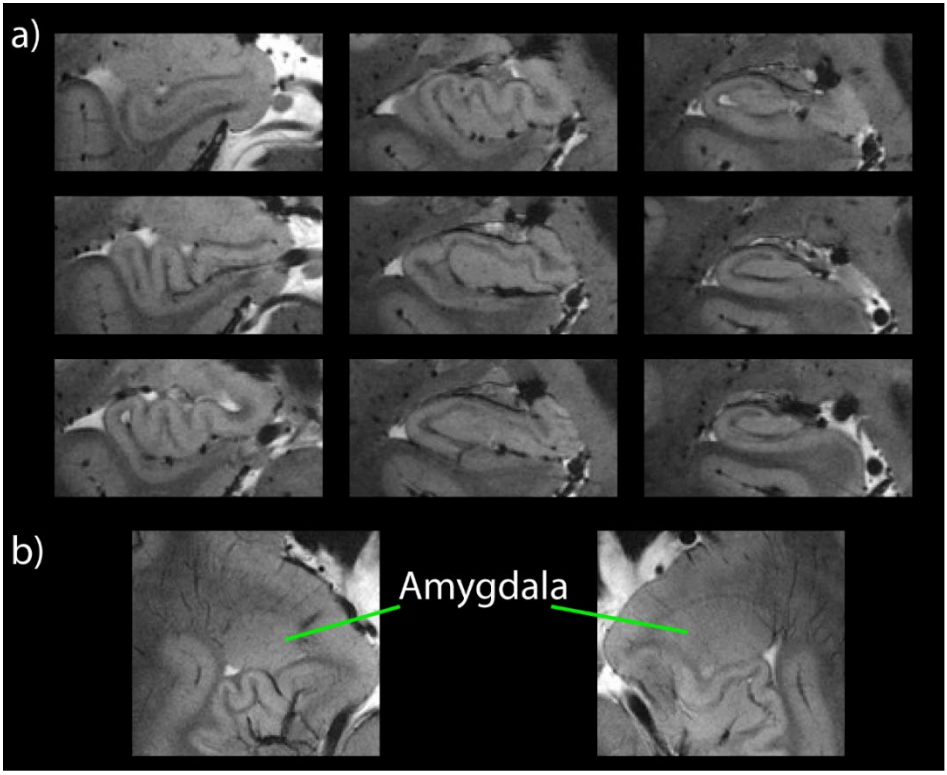

Figure 5.10: a) Several successive slices depicting the hippocampus from anterior-to-posterior direction. The convolved and folded structure of the hippocampus is visualized accurately. b) Axial view of the amygdala on both brain hemispheres.

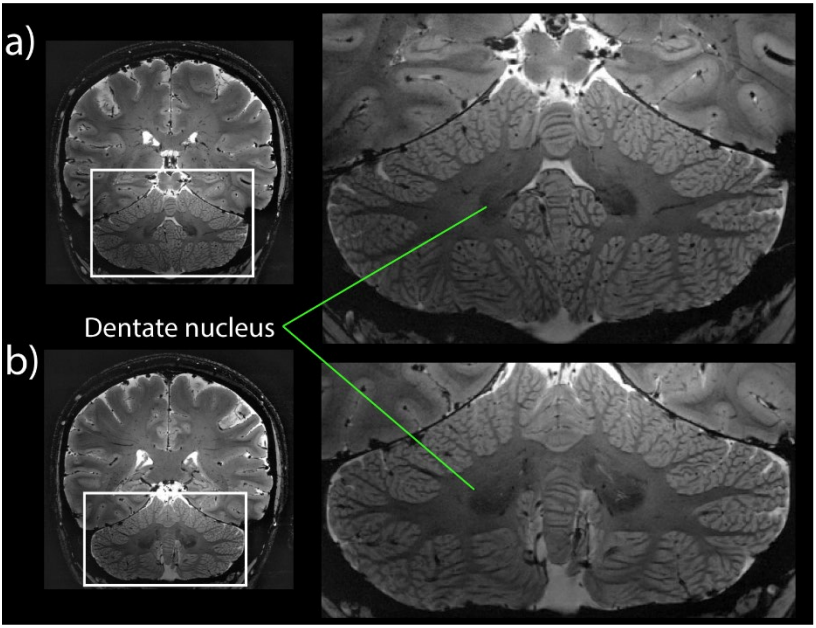

Figure 5.11: Coronal section through the cerebellum depicting the dentate nucleus along with several lobules and fissures. The folding of the cerebellar cortex around the interior white matter is visible.

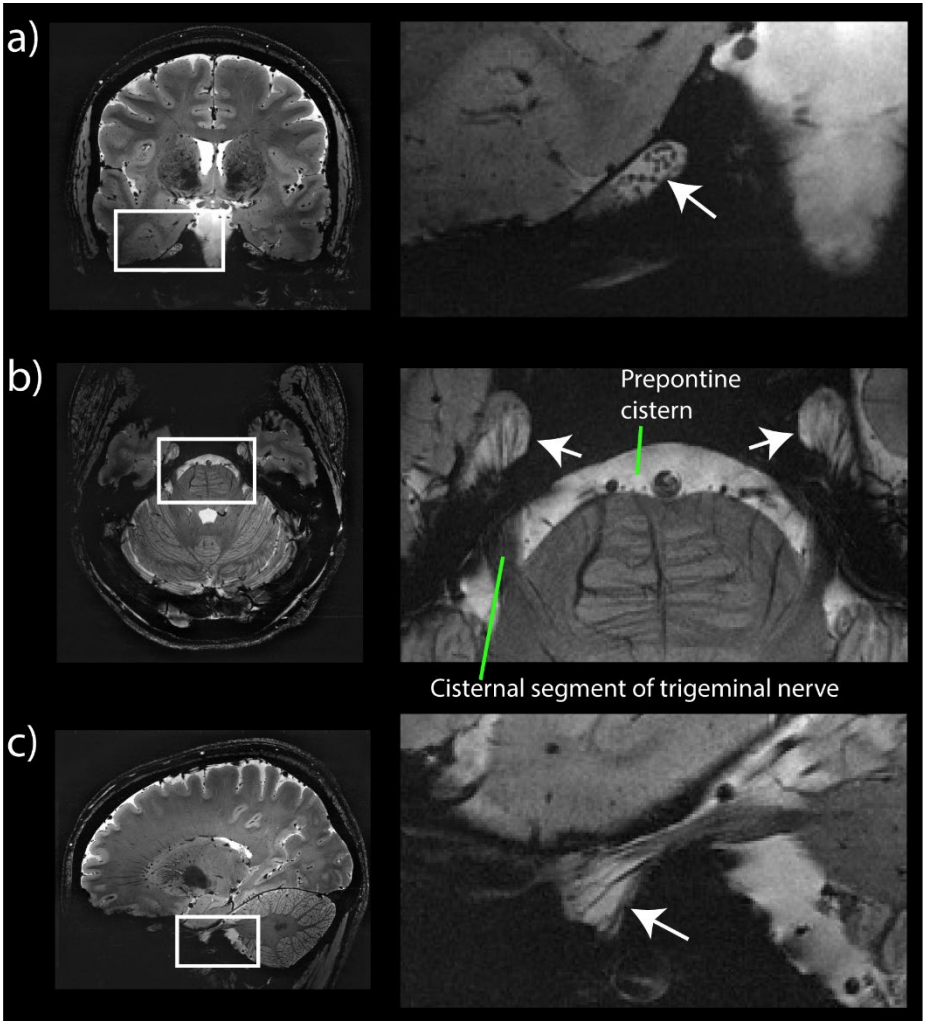

Figure 5.12: Three different views of the trigeminal nerve along with Meckel's cave. The trigeminal ganglion is visible in all orientations (arrow). a) the coronal section displays distinct black dots within the trigeminal ganglion, potentially depicting nerve bundles. b) course of the trigeminal nerve as it emerges from the lateral pons and traverses the prepontine cistern. c) sagittal view of the trigeminal nerve and ganglion.

5.4 Discussion

The results obtained in this work indicate that the dual control scheme provided high image quality in the challenging scenario of highest resolution T2* weighted scans covering the isocortex and subcortical brain regions. The extended duration of these scans resulted in acquiring data in the presence of head motion that exceeded imaging resolution by several times. Close inspection of the depicted brain regions revealed many anatomical structures and features that can be used for the detection and characterization of disease and disorders, such as the putamen, the caudate nucleus, the hippocampus or brainstem nuclei.

The acquired magnitude images exhibit a large variety of anatomic features that coincide well with histologic data from anatomical atlases, such as substructure of the globus pallidus, substructure of the red nucleus and small brainstem nuclei. The identified structures also included the entire set of 17 structures that were reported in a recent review[36] as the most frequently targeted ones based on the analysis of 163 scientific papers.

The visualization of transverse pontine fibers and tracts in the pons was particularly clear in transversal and sagittal sections and qualitatively approaches a level of detail as encountered in post-mortem studies, e.g. Ref. ([192]). Fine structures, such as the reticulotegmental nucleus or the medial longitudinal fasciculus were successfully visualized although they were reportedly not discernable in R2* data obtained in a previous study[193].

The depiction of adjacent structures with a relatively short T2*, such as the subthalamic nucleus and substantia nigra[194], revealed the limited ability of a strong T2* weighting to delineate the associated boundary as a consequence of the low signal intensities.

The qualitative image feature of up to threefold laminar contrast variation within cortical grey matter coincides with post-mortem high-resolution scans carried out with similar contrast and even smaller voxel size in a study that used these lamination patterns to discriminate between AD patients and non-neurological controls[179].

The direct visualization of the fibrous structure of the corpus callosum, whose structure develops with age[195], was reported using UHF MRI[196]. Due to the increased spatial resolution of the images presented in the present study, the fibrous structure is depicted even clearer.

The images obtained in this work exhibit a high effective resolution. Although no conspicuous artefacts are visible, a decrease in effective resolution could have potentially been caused by pulsatile brain motion. Such motion cannot adequately be measured and corrected with external sensors. Pulsatile motion of brain structures up to a few hundred microns has been reported in previous studies[197]. However, the potential bias of the reported quantitative results should be re-assessed because cardioballistic head movement during the cardiac cycle was not accounted for. Such movement has been detected using both NMR sensors[27] and optical means[18], exceeding 100 µm in foot-head direction[18].

The long scan duration needed to acquire five averages was a consequence of the SNR limited regime associated with small voxel

size. A higher SNR efficiency is needed to truly reduce scan time while conserving sufficient SNR at highest image resolution. Decreasing the acquisition bandwidth to increase SNR yield is a possibility, although it is generally more prone to off-resonance artefacts and tends to compromise the effective resolution due to PSF broadening associated with long readout duration. Resorting to a 3D encoded gradient echo sequence of corresponding contrast is of limited efficacy in terms of SNR efficiency since the T1 relaxation time of the targeted tissues is rather long relative to the typical TR in the performed scans. Ultimately, the use of higher magnetic field strengths combined with state-of-the-art receiver arrays provides an efficient means to increase SNR[198].

Simultaneous correction of head motion and field fluctuations can also be accomplished using other methodologies than NMR sensor based ones as employed in this study. However, the requirements on the respective correction loops are high. For motion detection, a high tracking precision is required, which generally depends on the targeted image resolution. In the present study, the tracking precision was one order of magnitude higher than the in-plane image resolution. Moreover, the tracking means should provide a sampling frequency that is able to capture the typical bandwidth of head motion that has been assessed to be approximately 12 Hz in earlier work[50]. Such specifications are offered by optical tracking methods, which, however, come with the line-of-sight requirement[18]. For field control, accurate field sensing and sufficiently fast shim actuation is needed. Navigator-based field mapping techniques have been proposed[15,148] and also the use of discrete off-resonance markers[60]. It is also worth exploring multi-coil shimming

setups that can achieve more local shimming and use loops with small inductances that lend themselves for dynamic shimming[161].

Field control performed in this work addresses external sources of field perturbation. However, it is important to acknowledge that there are external and internal sources of field perturbation. To counter field perturbations in the imaging volume, field control, as performed in this work, relies on the measurement of magnetic fields around the head. This approach assumes that there are no internal magnetic field sources, i.e. magnetic field sources inside the imaging volume. However, the head itself can be considered as an internal source of magnetic field perturbation due to its susceptibility distribution. Therefore, head motion may impact the measurements of the field probes around the head. In fact, recent work aimed at inferring head motion parameters from such measurements[167]. The motion and field traces presented in Figure 5.3 exhibit a moderate degree of correlation, visible mostly in higher-order shim terms, which is a manifestation of this effect. Since field control assumes external field perturbation and corrects for it, this effect might introduce subtle bias in the correction. In the present work, this did not seem to compromise the quality of field control, presumably, since the major part of temporal field variation is caused by breathing and was successfully compensated for. Also, zeroth-order correction was virtually unaffected by head motion. For an increased amount of motion, a model could be developed to discriminate between externally or internally induced field changes. Such a model could be based on a training phase to relate head motion parameters and field changes[167] or on computations of the expected field changes caused by head motion relying on a susceptibility model of the head[171],

which has recently been explored using a simplified susceptibility model[199]. To address internal field changes, several navigator-based methods have been proposed for on-the-fly B0 mapping and correction[148].

We believe that a dual control scheme as used in the present study will be of increasing importance at even higher field strengths, since respiration-induced B0 fluctuations will become more severe and the high-resolution objective ever more appealing. Note that the tracking precision of the employed head tracking approach using NMR field probes will also increase with field strength. In addition to increased SNR, higher field enhances the contrast of T2* based scans by increasing the effect of magnetic susceptibility variations across different tissues, e.g. becoming ever more sensitive to variations in iron or myelin content.

The results in this work indicate that dual control provides high image quality in extended T2*-weighted high resolution scans throughout the brain. Since it counters two of the main physiologic confounding factors, it offers the perspective to perform more robust imaging in different population groups. There is potential to apply this method to derived contrasts such as QSM, that has been used for clear distinction of the subthalamic nucleus from the adjacent substantia nigra[194,200] and provided promising results for the depiction of nuclei in the brainstem[193]. In fact, recent work demonstrated the potential of PMC for high-resolution QSM[182] and the application of field control to QSM was shown to enhance robustness and stability of the QSM method[143]. It is therefore assumed that the employed dual correction approach is highly promising also for derived contrasts, such as SWI or QSM.

Chapter 6

Conclusion & Outlook

This thesis has contributed to advancing the methodology of motion detection with NMR markers and has demonstrated its effectiveness for prospective motion correction of high-resolution scans at UHF. A new tracking method has been developed that eliminated one of the major drawbacks of NMR marker based tracking, namely the need to modify the sequence. Also, the development and in-depth characterization of the real-time field tracking approach for marker localization has obviated the calibration step which has been an obstacle to practical use. Additionally, it was shown that real-time field tracking enhances the tracking performance relative to calibration approaches. These developments facilitate the routine use of NMR markers for motion detection.

A further methodological advancement has been the combination of PMC with real-time field control, both based on NMR sensors. It was shown that the two control loops operate in a stable manner without compromising the performance of the individual correction loops.

Moreover, this combination proved to be synergistic and corrected for complementary effects in high-resolution T2* weighted imaging. It allowed an enhanced depiction of subcortical brain regions with highest-resolution T2* weighted scans and many anatomical features were visualized.

In the following a few remarks are presented to point to open questions and potential future directions.

6.1 Further methodological advances of NMR marker based tracking and motion correction

On the algorithmic side, different signal models are possible, as indicated in the discussion in chapter 3. Knowledge of the field dynamics the probes are exposed to is crucial for localization accuracy. Although a first-order model provided reliable tracking results, the adoption of higher-order field models is possible given the availability of field probes in the laboratory frame. At this point it is questionable if an extension of the spherical harmonic basis to higher orders is the most promising strategy, because higher orders require ever more field probes in the laboratory frame. For practical reasons, the goal will always be to obtain good accuracy with a limited amount of laboratory field probes. Therefore, an empirical basis might result in a more favorable trade-off.

In the scenarios studied in the present thesis, the occurring head motion was small and the probes were placed close to the head, such that they remained within the linear range of the gradient system and reliable tracking could be performed without gradient non-linearity correction. However, a recent study has shown that gradient non-linearity correction

can be necessary to attain sufficient tracking accuracy, particularly when the probes are placed further from the isocenter[62].

The knowledge of field dynamics needed to localize the probes has so far been obtained using a preceding calibration or real-time field tracking. Another alternative is given by GIRF (gradient impulse response function) prediction[52]. This approach has not been explored yet for marker tracking and would allow to obtain the relevant gradient dynamics without real-time field tracking or a dedicated calibration measurement, relying just on the one-time GIRF calibration. Thermal effects could also be accounted for based on recent efforts to account for thermal variation of the GIRFs using temperature sensors[61,201,202].

Further developments are conceivable on the hardware level. The cables of the field probes used in this thesis were thin and had a small bending radius, which provided a high degree of flexibility and minimized the forces exerted on the probes. Further flexibility could be obtained via optical links or wireless operation of NMR markers, which certainly poses some challenges.

As mentioned in chapter 1, there are some effects that are not addressed by PMC. These effects include inhomogeneity of receive and transmit fields, gradient non-linearity as well as field changes inside the brain induced by changing orientation of the head relative to the main magnetic field. Mere adaptation of the field-of-view, as done during PMC, is generally not sufficient to address all these issues. However, it has been shown that some of these effects can be addressed by retrospective correction[55,56,203]. The severity of these effects generally depends on the imaging sequence and the intensity of motion and should be assessed carefully. For example, sequences relying on

accurate knowledge of the B_0 map, such as spiral readouts, will probably require an additional correction step beyond PMC for successful motion correction. For the scenarios studied in this work, no conspicuous artefacts were visible that were potentially caused by any of these effects.

6.2 Head mount design

The use of head-mounted markers for head tracking requires a robust solution for marker attachment. This requirement is shared by all marker-based techniques. The variety of solutions for marker attachment strongly depends on the specific type of the marker or markers used. For instance, optical tracking of a moiré-phase-pattern marker[18] requires the placement of only one small marker. Here, limitations arise from the line-of-sight requirement, so that arbitrary positions are not possible. For the case of NMR field probes used in this work, the solution space of possible head attachments looks different, since there are four markers that need to be distributed and the cables need to be considered. However, it is beneficial that no line-of-sight is needed, which extends the possible solution space.

In fact, marker fixation may even be considered a bottleneck given that the physics of many tracking modalities permit extremely high tracking precision and accuracy. Without doubt, the overall performance of a tracking system will depend not only on the tracking performance per se, but also on the reliability of the demanded rigid relationship between the head and the marker/markers.

The above considerations call for a thorough assessment and validation of potential mounting systems. To this end, a gold standard is needed.

A generally accepted gold standard is fixation of markers to the upper jaw. While not the most comfortable solution for a patient, it lends itself for benchmarking potential mounting systems and is also widely used for the demonstration of PMC, particularly with optical tracking systems.

The experiments carried out within this work were done on a 7T system with a 32 channel receiver array, which was rather tight and motion ranges were therefore intrinsically limited. The obtained results testify to the adequateness of the 3D-printed headset used for the studied scenarios. However, there are some limitations associated with the use of such a headset. This approach is obviously limited when larger motion occurs such that the headset touches the inner wall of the receiver array which will very likely result in displacement of the headset relative to the head. In the experience with compliant subjects this has not occurred, but for uncooperative subjects or subjects with difficulties in lying still this will likely be an issue. Also, since the space in the receiver array was very limited, head size was another restricting factor in that it resulted in even less freedom to move for larger head size and, eventually, not fitting at all.

Among other possibilities described in the literature, there is the attachment to EEG caps[60] or, as envisaged by a commercial provider of optical tracking, attachment via a nose bridge.

The development of an optimal solution, which may include trade-offs between tracking performance and convenience of marker placement will play a crucial role for the future and the acceptance of marker based motion detection in general.

6.3 Neuroimaging at UHF

UHF imaging holds the promise to depict brain structures with tremendous detail. Methods such as motion correction or field control will gain further importance with the pursuit of high-resolution imaging and T2* based contrasts, which benefit from high magnetic field. Such applications will likely evolve with the wider adoption of high-field MR systems, especially considering the recent clearance of a 7T system by the Food and Drug Administration (FDA).

Future work should further explore the value that could be added in medical research through high-resolution neuroimaging. This demands collaboration with medical doctors and neuroscientists to study potential improvements in early disease detection and characterization, particularly with regard to neurodegenerative dementias[204]. From a data perspective, a high-resolution depiction of the brain with meaningful contrast can be considered to be particularly rich in features, which motivates exploring to which extent machine learning methods could support the analysis and interpretation of such images.

The in vivo noninvasive visualization of brain structures at a wholly new scale opens the door to see a plethora of small nuclei, tracts and substructures of larger entities in the brain. However, obtaining access to a ground truth which explains what exactly has been visualized using MRI is difficult and hardly possible in living organisms. Histological atlases, as used for labelling of anatomical structures in chapter 5 of this thesis, provide a detailed view of the underlying anatomy, but include data of only a small number of brains, thus not accounting for potential variability of structures across subjects. Closer links between the visualization of brain structures and tissue properties using MR contrasts

are desirable to validate what is depicted with MRI. Arguably, the most insight is obtained when post-mortem specimens undergo MR scans and are subsequently analyzed with histological staining and microscopy techniques. This allows not only more unequivocal labelling of structures but also permits identifying sources of contrast. An example of the latter includes work by Fukunaga et al[191], that aimed to establish the origin of laminar contrast variation in cortical grey matter. Upon chemical extraction of iron from brain specimens, they were able to conclude that R2* contrast resulted predominantly from variations in iron concentration rather than from variations in myelin concentration.

6.4 On the clinical impact of motion correction

Despite many years of method development, the adoption of head motion correction techniques into clinical routine has so far been limited.

To foster the clinical impact of head motion correction techniques, rigid requirement specifications are needed in terms of tracking accuracy, precision and update rate, which will clearly depend on the envisaged scenario and will help devise a method that is tailored to user needs. What seems to hold for all head tracking methods is that there is a trade-off between the tracking performance and practicality. Here, “practicality” sums up all characteristics of the tracking method other than tracking performance, i.e. its interference with the workflow, ease of implementation, patient comfort etc.

For the clinical setting, the relevant criterion for successful motion correction should be the diagnostic value of an image. If motion correction resulted in images with sufficient diagnostic value, which would have otherwise been excessively corrupted by motion artefacts or

only possible with sedation of the patient, a true success story could emerge.

Measureable goals would be a decrease in the number of repeated scans and the possibility to newly image patients without sedation. Since many neurological scans are performed with coarser resolutions than a few hundred micrometers, compromises in tracking performance relative to the one needed for highest-resolution scans could be accepted if motion detection was performed such that it is fosters adoption by clinical users, e.g. with an easy-to-use wearable that offers high patient comfort and minimizes additional efforts of the operator.

References

1. Andre JB, Bresnahan BW, Mossa-Basha M, Hoff MN, Smith CP, Anzai Y, Cohen WA. Toward Quantifying the Prevalence, Severity, and Cost Associated With Patient Motion During Clinical MR Examinations. *Journal of the American College of Radiology*. 2015;12(7):689-695. doi:10.1016/j.jacr.2015.03.007.

2. Versluis MJ, Peeters JM, van Rooden S, van der Grond J, van Buchem MA, Webb AG, van Osch MJP. Origin and reduction of motion and f0 artifacts in high resolution T2*-weighted magnetic resonance imaging: Application in Alzheimer's disease patients. *NeuroImage*. 2010;51(3):1082-1088. doi:10.1016/j.neuroimage.2010.03.048.

3. Duerst Y, Wilm BJ, Dietrich BE, Vannesjo SJ, Barmet C, Schmid T, Brunner DO, Pruessmann KP. Real-time feedback for spatiotemporal field stabilization in MR systems. *Magnetic Resonance in Medicine*. 2015;73(2):884-893. doi:10.1002/mrm.25167.

4. Power JD, Silver BM, Silverman MR, Ajodan EL, Bos DJ, Jones RM. Customized head molds reduce motion during resting state fMRI scans. *NeuroImage*. 2019;189:141-149. doi:10.1016/j.neuroimage.2019.01.016.

5. Pruessmann KP, Weiger M, Scheidegger MB, Boesiger P. SENSE: Sensitivity encoding for fast MRI. *Magnetic Resonance in Medicine*. 1999;42(5):952-962. doi:10.1002/(SICI)1522-2594(199911)42:5<952::AID-MRM16>3.0.CO;2-S.

6. Lustig M, Donoho D, Pauly JM. Sparse MRI: The application of compressed sensing for rapid MR imaging. *Magnetic Resonance in Medicine*. 2007;58(6):1182-1195. doi:10.1002/mrm.21391.

7. Korin HW, Farzaneh F, Wright RC, Riederer SJ. Compensation for effects of linear motion in MR imaging. *Magnetic Resonance in Medicine*. 1989;12(1):99-113. doi:10.1002/mrm.1910120113.

8. Atkinson D, Hill DLG. Reconstruction after rotational motion. *Magnetic Resonance in Medicine*. 2003;49(1):183-187. doi:10.1002/mrm.10333.

9. Atkinson D, Hill DLG, Stoyle PNR, Summers PE, Keevil SF. Automatic correction of motion artifacts in magnetic resonance images using an entropy focus criterion. *IEEE Transactions on Medical Imaging*. 1997;16(6):903-910. doi:10.1109/42.650886.

10. Loktyushin A, Nickisch H, Pohmann R, Schölkopf B. Blind retrospective motion correction of MR images. *Magn Reson Med*. 2013;70(6):1608-1618. doi:10.1002/mrm.24615.

11. Batchelor PG, Atkinson D, Irarrazaval P, Hill DLG, Hajnal J, Larkman D. Matrix description of general motion correction applied to multishot images. *Magn Reson Med*. 2005;54(5):1273-1280. doi:10.1002/mrm.20656.

12. Maclaren J, Herbst M, Speck O, Zaitsev M. Prospective motion correction in brain imaging: A review. *Magn Reson Med*. 2013;69:621-636. doi:10.1002/mrm.24314.

13. Godenschweger F, Kägebein U, Stucht D, Yarach U, Sciarra A, Yakupov R, Lüsebrink F, Schulze P, Speck O. Motion correction in MRI of the brain. *Phys Med Biol*. 2016;61(5):R32. doi:10.1088/0031-9155/61/5/R32.

14. Welch EB, Manduca A, Grimm RC, Ward HA, Jack Jr. CR. Spherical navigator echoes for full 3D rigid body motion measurement in MRI. *Magn Reson Med*. 2002;47:32-41. doi:10.1002/mrm.10012.

15. van der Kouwe AJW, Benner T, Dale AM. Real-time rigid body motion correction and shimming using cloverleaf navigators. *Magn Reson Med*. 2006;56:1019-1032. doi:10.1002/mrm.21038.

16. Tisdall MD, Hess AT, Reuter M, Meintjes EM, Fischl B, van der Kouwe AJW. Volumetric navigators for prospective motion correction and selective reacquisition in neuroanatomical MRI.

Magnetic Resonance Medicine. 2012;68:389-399. doi:10.1002/mrm.23228.

17. Gallichan D, Marques JP, Gruetter R. Retrospective correction of involuntary microscopic head movement using highly accelerated fat image navigators (3D FatNavs) at 7T. *Magn Reson Med*. 2016;75:1030-1039. doi:10.1002/mrm.25670.

18. Maclaren J, Armstrong BSR, Barrows RT, Danishad KA, Ernst T, Foster CL, Gumus K, Herbst M, Kadashevich IY, Kusik TP, Li Q, Lovell-Smith C, Prieto T, Schulze P, Speck O, Stucht D, Zaitsev M. Measurement and Correction of Microscopic Head Motion during Magnetic Resonance Imaging of the Brain. *PLoS ONE*. 2012;7(11):e48088. doi:10.1371/journal.pone.0048088.

19. Aksoy M, Forman C, Straka M, Skare S, Holdsworth S, Hornegger J, Bammer R. Real-time optical motion correction for diffusion tensor imaging. *Magn Reson Med*. 2011;66(2):366-378. doi:10.1002/mrm.22787.

20. Zaitsev M, Dold C, Sakas G, Hennig J, Speck O. Magnetic resonance imaging of freely moving objects: prospective real-time motion correction using an external optical motion tracking system. *NeuroImage*. 2006;31(3):1038-1050. doi:10.1016/j.neuroimage.2006.01.039.

21. Olesen OV, Paulsen RR, Hojgaard L, Roed B, Larsen R. Motion Tracking for Medical Imaging: A Nonvisible Structured Light Tracking Approach. *IEEE Transactions on Medical Imaging*. 2012;31(1):79-87. doi:10.1109/TMI.2011.2165157.

22. Maclaren J, Kyme A, Aksoy M, Bammer R. Towards Markerless Optical Tracking for Prospective Motion Correction in Brain Imaging. *In Proceedings of the 24th Annual Meeting of ISMRM, Singapore, 2016*. p. 1858.

23. Ooi MB, Aksoy M, Maclaren J, Watkins RD, Bammer R. Prospective motion correction using inductively coupled wireless

RF coils. *Magn Reson Med*. 2013;70:639-647. doi:10.1002/mrm.24845.

24. Haeberlin M, Kasper L, Barmet C, Brunner DO, Dietrich BE, Gross S, Wilm BJ, Kozerke S, Pruessmann KP. Real-time motion correction using gradient tones and head-mounted NMR field probes. *Magn Reson Med*. 2015;74:647-660. doi:10.1002/mrm.25432.

25. Sengupta S, Tadanki S, Gore JC, Welch EB. Prospective real-time head motion correction using inductively coupled wireless NMR probes. *Magn Reson Med*. 2014;72:971-985. doi:10.1002/mrm.25001.

26. Ooi MB, Krueger S, Thomas WJ, Swaminathan SV, Brown TR. Prospective Real-Time Correction for Arbitrary Head Motion Using Active Markers. *Magn Reson Med*. 2009;62(4):943-954. doi:10.1002/mrm.22082.

27. Aranovitch A, Haeberlin M, Gross S, Dietrich BE, Wilm BJ, Brunner DO, Schmid T, Luechinger R, Pruessmann KP. Prospective motion correction with NMR markers using only native sequence elements. *Magnetic Resonance in Medicine*. 2018;79(4):2046-2056. doi:10.1002/mrm.26877.

28. Niekerk A van, Kouwe A van der, Meintjes E. A Method for Measuring Orientation Within a Magnetic Resonance Imaging Scanner Using Gravity and the Static Magnetic Field (VectOrient). *IEEE Transactions on Medical Imaging*. 2017;36(5):1129-1139. doi:10.1109/TMI.2017.2652502.

29. van Niekerk A, van der Kouwe A, Meintjes E. Toward “plug and play” prospective motion correction for MRI by combining observations of the time varying gradient and static vector fields. *Magnetic Resonance in Medicine*. 2019;82(3):1214-1228. doi:10.1002/mrm.27790.

30. Schildknecht C, Brunner DO, Schmid T, Reber J, Marjanovic J, Pruessmann KP. Wireless motion tracking with short-wave

radiofrequency. *In Proceedings of the 27th Annual Meeting of ISMRM, Montreal, Canada, 2019*. p. 0066.

31. De Zanche N, Barmet C, Nordmeyer-Massner JA, Pruessmann KP. NMR probes for measuring magnetic fields and field dynamics in MR systems. *Magn Reson Med*. 2008;60:176-186. doi:10.1002/mrm.21624.

32. Gross S, Barmet C, Dietrich BE, Brunner DO, Schmid T, Pruessmann KP. Dynamic nuclear magnetic resonance field sensing with part-per-trillion resolution. *Nature Communications*. 2016;7:13702. doi:10.1038/ncomms13702.

33. Dietrich BE, Brunner DO, Wilm BJ, Barmet C, Gross S, Kasper L, Haeberlin M, Schmid T, Vannesjo SJ, Pruessmann KP. A field camera for MR sequence monitoring and system analysis. *Magn Reson Med*. 2016;75:1831-1840. doi:10.1002/mrm.25770.

34. Barmet C, Zanche ND, Pruessmann KP. Spatiotemporal magnetic field monitoring for MR. *Magn Reson Med*. 2008;60:187-197. doi:10.1002/mrm.21603.

35. Ooi MB, Krueger S, Thomas WJ, Swaminathan SV, Brown TR. Prospective Real-Time Correction for Arbitrary Head Motion Using Active Markers. *Magn Reson Med*. 2009;62:943-954. doi:10.1002/mrm.22082.

36. Keuken MC, Isaacs BR, Trampel R, Zwaag W van der, Forstmann BU. Visualizing the Human Subcortex Using Ultra-high Field Magnetic Resonance Imaging. *Brain Topogr*. 2018;31(4):513-545. doi:10.1007/s10548-018-0638-7.

37. Zaitsev M, Maclaren J, Herbst M. Motion artifacts in MRI: A complex problem with many partial solutions. *J Magn Reson Imaging*. 2015;42(4):887-901. doi:10.1002/jmri.24850.

38. Loktyushin A, Nickisch H, Pohmann R, Schölkopf B. Blind multirigid retrospective motion correction of MR images. *Magn Reson Med*. 2015;73:1457-1468. doi:10.1002/mrm.25266.

39. Odille F, Vuissoz P-A, Marie P-Y, Felblinger J. Generalized Reconstruction by Inversion of Coupled Systems (GRICS) applied to free-breathing MRI. *Magn Reson Med*. 2008;60(1):146-157. doi:10.1002/mrm.21623.

40. Schulz J, Siegert T, Reimer E, Labadie C, Maclaren J, Herbst M, Zaitsev M, Turner R. An embedded optical tracking system for motion-corrected magnetic resonance imaging at 7T. *Magn Reson Mater Phy*. 2012;25(6):443-453. doi:10.1007/s10334-012-0320-0.

41. Qin L, van Gelderen P, Derbyshire JA, Jin F, Lee J, de Zwart JA, Tao Y, Duyn JH. Prospective Head Movement Correction for High Resolution MRI using an In-bore Optical Tracking System. *Magn Reson Med*. 2009;62:924-934. doi:10.1002/mrm.22076.

42. Benjaminsen C, Jensen RR, Wighton P, Tisdall MD, Johannesen HH, Law I, van der Kouwe AJW, Olesen OV. Real Time MRI Motion Correction with Markerless Tracking. *In Proceedings of the 24th Annual Meeting of ISMRM, Singapore, 2016*. p. 1860.

43. White N, Roddey C, Shankaranarayanan A, Han E, Rettmann D, Santos J, Kuperman J, Dale A. PROMO: Real-time prospective motion correction in MRI using image-based tracking. *Magn Reson Med*. 2010;63:91-105. doi:10.1002/mrm.22176.

44. Qin L, Schmidt EJ, Tse ZTH, Santos J, Hoge WS, Tempany-Afdhal C, Butts-Pauly K, Dumoulin CL. Prospective motion correction using tracking coils. *Magn Reson Med*. 2013;69:749-759. doi:10.1002/mrm.24310.

45. Andersen M, Madsen KH. Placement of field probes for stabilization of breathing-induced B0-fluctuations in the brain. *In Proceedings of the 23th Annual Meeting of ISMRM, Toronto, 2015*. p. 1015.

46. Smink J, Häkkinen M, Holthuizen R, Krueger S, Ries M, Berber Y, Moonen C, Köhler M, Vahala E. eXTernal Control (XTC): a flexible, real-time, low-latency, bi-directional scanner interface. *In*

Proceedings of the 19th Annual Meeting of ISMRM, Montreal, Canada, 2011. p. 1755.

47. Umeyama S. Least-squares estimation of transformation parameters between two point patterns. *IEEE Transactions on Pattern Analysis and Machine Intelligence*. 1991;13(4):376-380. doi:10.1109/34.88573.

48. Friedman L, Glover GH. Report on a multicenter fMRI quality assurance protocol. *J Magn Reson Imaging*. 2006;23(6):827-839. doi:10.1002/jmri.20583.

49. Aksoy M, Maclaren J, Bammer R. Prospective motion correction for 3D pseudo-continuous arterial spin labeling using an external optical tracking system. *Magnetic Resonance Imaging*. 2017;39(Supplement C):44-52. doi:10.1016/j.mri.2017.01.018.

50. Haeberlin M, Aranovitch A, Wilm BJ, Brunner DO, Dietrich BE, Barmet C, Pruessmann KP. Advances in Prospective Motion Correction with Gradient Tones. *In Proceedings of the 24th Annual Meeting of ISMRM, Singapore, 2016*. p. 337.

51. Maclaren J, Speck O, Hennig J, Zaitsev M. A Kalman filtering framework for prospective motion correction. *In Proceedings of the 17th Annual Meeting of ISMRM, Honolulu, Hawaii, USA, 2009*. p. 4602.

52. Vannesjo SJ, Haeberlin M, Kasper L, Pavan M, Wilm BJ, Barmet C, Pruessmann KP. Gradient system characterization by impulse response measurements with a dynamic field camera. *Magn Reson Med*. 2013;69:583-593. doi:10.1002/mrm.24263.

53. Stucht D, Danishad KA, Schulze P, Godenschweger F, Zaitsev M, Speck O. Highest Resolution In Vivo Human Brain MRI Using Prospective Motion Correction. *PLoS ONE*. 2015;10(7):e0133921. doi:10.1371/journal.pone.0133921.

54. Lüsebrink F, Sciarra A, Mattern H, Yakupov R, Speck O. T1-weighted in vivo human whole brain MRI dataset with an

ultrahigh isotropic resolution of 250 μm. *Scientific Data*. 2017;4:170032. doi:10.1038/sdata.2017.32.

55. Bammer R, Aksoy M, Liu C. Augmented Generalized SENSE Reconstruction to Correct for Rigid Body Motion. *Magn Reson Med*. 2007;57:90-102. doi:10.1002/mrm.21106.

56. Yarach U, Luengviriya C, Stucht D, Godenschweger F, Schulze P, Speck O. Correction of B 0-induced geometric distortion variations in prospective motion correction for 7T MRI. *Magn Reson Mater Phy*. 2016;29:319-332. doi:10.1007/s10334-015-0515-2.

57. Frost R, Wighton P, Karahanoğlu FI, Robertson RL, Grant PE, Fischl B, Tisdall MD, Kouwe A van der. Markerless high-frequency prospective motion correction for neuroanatomical MRI. *Magnetic Resonance in Medicine*. 2019;82(1):126-144. doi:10.1002/mrm.27705.

58. Singh A, Zahneisen B, Keating B, Herbst M, Chang L, Zaitsev M, Ernst T. Optical tracking with two markers for robust prospective motion correction for brain imaging. *Magn Reson Mater Phy*. 2015;28(6):523-534. doi:10.1007/s10334-015-0493-4.

59. Maclaren J, Aksoy M, Ooi MB, Zahneisen B, Bammer R. Prospective motion correction using coil-mounted cameras: Cross-calibration considerations. *Magnetic Resonance in Medicine*. 2018;79(4):1911-1921. doi:10.1002/mrm.26838.

60. Jorge J, Gretsch F, Gallichan D, Marques JP. Tracking discrete off-resonance markers with three spokes (trackDOTS) for compensation of head motion and B0 perturbations: Accuracy and performance in anatomical imaging. *Magnetic Resonance in Medicine*. 2018;79(1):160-171. doi:10.1002/mrm.26654.

61. Dietrich BE, Reber J, Brunner DO, Wilm BJ, Pruessmann KP. Analysis and Prediction of Gradient Response Functions under Thermal Load. *In Proceedings of the 24th Annual Meeting of ISMRM, Singapore, 2016*. p. 3551.

62. Eschelbach M, Aghaeifar A, Bause J, Handwerker J, Anders J, Engel E-M, Thielscher A, Scheffler K. Comparison of prospective head motion correction with NMR field probes and an optical tracking system. *Magnetic Resonance in Medicine*. 2019;81(1):719-729. doi:10.1002/mrm.27343.

63. Haacke EM. Susceptibility weighted imaging. December 2003. https://patents.google.com/patent/US6658280B1/en. Accessed July 10, 2019.

64. Haacke EM, Xu Y, Cheng Y-CN, Reichenbach JR. Susceptibility weighted imaging (SWI). *Magnetic Resonance in Medicine*. 2004;52(3):612-618. doi:10.1002/mrm.20198.

65. Yablonskiy DA, Haacke EM. Theory of NMR signal behavior in magnetically inhomogeneous tissues: The static dephasing regime. *Magnetic Resonance in Medicine*. 1994;32(6):749-763. doi:10.1002/mrm.1910320610.

66. Yablonskiy DA. Quantitation of intrinsic magnetic susceptibility-related effects in a tissue matrix. Phantom study. *Magnetic Resonance in Medicine*. 1998;39(3):417-428. doi:10.1002/mrm.1910390312.

67. Tang MY, Chen TW, Zhang XM, Huang XH. GRE T2∗-Weighted MRI: Principles and Clinical Applications. *Biomed Res Int*. 2014;2014. doi:10.1155/2014/312142.

68. Okazaki S, Sakaguchi M, Hyun B, Nagano K, Tagaya M, Sakata Y, Sakaguchi T, Kitagawa K. Cerebral Microbleeds Predict Impending Intracranial Hemorrhage in Infective Endocarditis. *CED*. 2011;32(5):483-488. doi:10.1159/000331475.

69. Ward H, Shum D, Wallace G, Boon J. Pediatric traumatic brain injury and procedural memory. *J Clin Exp Neuropsychol*. 2002;24(4):458-470. doi:10.1076/jcen.24.4.458.1032.

70. Tong KA, Ashwal S, Holshouser BA, Shutter LA, Herigault G, Haacke EM, Kido DK. Hemorrhagic Shearing Lesions in Children

and Adolescents with Posttraumatic Diffuse Axonal Injury: Improved Detection and Initial Results. *Radiology*. 2003;227(2):332-339. doi:10.1148/radiol.2272020176.

71. Tong KA, Ashwal S, Holshouser BA, Nickerson JP, Wall CJ, Shutter LA, Osterdock RJ, Haacke EM, Kido D. Diffuse axonal injury in children: Clinical correlation with hemorrhagic lesions. *Annals of Neurology*. 2004;56(1):36-50. doi:10.1002/ana.20123.

72. Babikian T, Freier MC, Tong KA, Nickerson JP, Wall CJ, Holshouser BA, Burley T, Riggs ML, Ashwal S. Susceptibility Weighted Imaging: Neuropsychologic Outcome and Pediatric Head Injury. *Pediatric Neurology*. 2005;33(3):184-194. doi:10.1016/j.pediatrneurol.2005.03.015.

73. Ashwal S, Babikian T, Gardner-Nichols J, Freier M-C, Tong KA, Holshouser BA. Susceptibility-Weighted Imaging and Proton Magnetic Resonance Spectroscopy in Assessment of Outcome After Pediatric Traumatic Brain Injury. *Archives of Physical Medicine and Rehabilitation*. 2006;87(12, Supplement):50-58. doi:10.1016/j.apmr.2006.07.275.

74. Park J-H, Park S-W, Kang S-H, Nam T-K, Min B-K, Hwang S-N. Detection of Traumatic Cerebral Microbleeds by Susceptibility-Weighted Image of MRI. *J Korean Neurosurg Soc*. 2009;46(4):365-369. doi:10.3340/jkns.2009.46.4.365.

75. Tong K, Holshouser B, Wu Z. Traumatic Brain Injury. In: *Susceptibility Weighted Imaging in MRI*. Wiley-Blackwell; 2011:171-190. doi:10.1002/9780470905203.ch11.

76. Geurts BHJ, Andriessen TMJC, Goraj BM, Vos PE. The reliability of magnetic resonance imaging in traumatic brain injury lesion detection. *Brain Injury*. 2012;26(12):1439-1450. doi:10.3109/02699052.2012.694563.

77. Beauchamp MH, Beare R, Ditchfield M, Coleman L, Babl FE, Kean M, Crossley L, Catroppa C, Yeates KO, Anderson V. Susceptibility weighted imaging and its relationship to outcome

after pediatric traumatic brain injury. *Cortex*. 2013;49(2):591-598. doi:10.1016/j.cortex.2012.08.015.

78. Tate DF, Gusman M, Kini J, Reid M, Velez CS, Drennon AM, Cooper DB, Kennedy JE, Bowles AO, Bigler ED, Lewis JD, Ritter J, York GE. Susceptibility Weighted Imaging and White Matter Abnormality Findings in Service Members With Persistent Cognitive Symptoms Following Mild Traumatic Brain Injury. *Mil Med*. 2017;182(3-4):e1651-e1658. doi:10.7205/MILMED-D-16-00132.

79. Saini J, Kesavadas C, Thomas B, Kapilamoorthy TR, Gupta AK, Radhakrishnan A, Radhakrishnan K. Susceptibility weighted imaging in the diagnostic evaluation of patients with intractable epilepsy. *Epilepsia*. 2009;50(6):1462-1473. doi:10.1111/j.1528-1167.2008.01882.x.

80. Colbert CA, Holshouser BA, Aaen GS, Sheridan C, Oyoyo U, Kido D, Ashwal S. Value of Cerebral Microhemorrhages Detected with Susceptibility-weighted MR Imaging for Prediction of Long-term Outcome in Children with Nonaccidental Trauma. *Radiology*. 2010;256(3):898-905. doi:10.1148/radiol.10091842.

81. Iwasaki H, Fujita Y, Hara M. Susceptibility-weighted imaging in acute-stage pediatric convulsive disorders. *Pediatrics International*. 2015;57(5):922-929. doi:10.1111/ped.12678.

82. Verma RK, Abela E, Schindler K, Krestel H, Springer E, Huber A, Weisstanner C, Hauf M, Gralla J, Wiest R. Focal and Generalized Patterns of Cerebral Cortical Veins Due to Non-Convulsive Status Epilepticus or Prolonged Seizure Episode after Convulsive Status Epilepticus – A MRI Study Using Susceptibility Weighted Imaging. *PLOS ONE*. 2016;11(8):e0160495. doi:10.1371/journal.pone.0160495.

83. Kwan BYM, Salehi F, Ohorodnyk P, Lee DH, Burneo JG, Mirsattari SM, Steven D, Hammond R, Peters TM, Khan AR. Usage of SWI (susceptibility weighted imaging) acquired at 7T for qualitative evaluation of temporal lobe epilepsy patients with

histopathological and clinical correlation: An initial pilot study. *Journal of the Neurological Sciences*. 2016;369:82-87. doi:10.1016/j.jns.2016.07.066.

84. Pittau F, Baud MO, Jorge J, Xin L, Grouiller F, Iannotti GR, Seeck M, Lazeyras F, Vulliémoz S, Vargas MI. MP2RAGE and Susceptibility-Weighted Imaging in Lesional Epilepsy at 7T. *Journal of Neuroimaging*. 2018;28(4):365-369. doi:10.1111/jon.12523.

85. Toh CH, Wei K-C, Chang C-N, Hsu P-W, Wong H-F, Ng S-H, Castillo M, Lin C-P. Differentiation of Pyogenic Brain Abscesses from Necrotic Glioblastomas with Use of Susceptibility-Weighted Imaging. *American Journal of Neuroradiology*. 2012;33(8):1534-1538. doi:10.3174/ajnr.A2986.

86. Lai PH, Chang HC, Chuang TC, Chung HW, Li JY, Weng MJ, Fu JH, Wang PC, Li SC, Pan HB. Susceptibility-Weighted Imaging in Patients with Pyogenic Brain Abscesses at 1.5T: Characteristics of the Abscess Capsule. *American Journal of Neuroradiology*. 2012;33(5):910-914. doi:10.3174/ajnr.A2866.

87. Antulov R, Dolic K, Fruehwald-Pallamar J, Miletic D, Thurnher MM. Differentiation of pyogenic and fungal brain abscesses with susceptibility-weighted MR sequences. *Neuroradiology*. 2014;56(11):937-945. doi:10.1007/s00234-014-1411-6.

88. Cho S-M, Rice C, Marquardt RJ, Zhang LQ, Khoury J, Thatikunta P, Buletko AB, Hardman J, Uchino K, Wisco D, Group on behalf of IES and IC (IESIC). Magnetic Resonance Imaging Susceptibility-Weighted Imaging Lesion and Contrast Enhancement May Represent Infectious Intracranial Aneurysm in Infective Endocarditis. *CED*. 2017;44(3-4):210-216. doi:10.1159/000479706.

89. Li C, Ai B, Li Y, Qi H, Wu L. Susceptibility-weighted imaging in grading brain astrocytomas. *European Journal of Radiology*. 2010;75(1):e81-e85. doi:10.1016/j.ejrad.2009.08.003.

90. Berberat J, Grobholz R, Boxheimer L, Rogers S, Remonda L, Roelcke U. Differentiation Between Calcification and Hemorrhage in Brain Tumors Using Susceptibility-Weighted Imaging: A Pilot Study. *American Journal of Roentgenology*. 2014;202(4):847-850. doi:10.2214/AJR.13.10745.

91. Mohammed W, Xunning H, Haibin S, Jingzhi M. Clinical applications of susceptibility-weighted imaging in detecting and grading intracranial gliomas: a review. *Cancer Imaging*. 2013;13(2):186-195. doi:10.1102/1470-7330.2013.0020.

92. Franceschi AM, Moschos SJ, Anders CK, Glaubiger S, Collichio FA, Lee CB, Castillo M, Lee YZ. Utility of Susceptibility Weighted Imaging (SWI) in the Detection of Brain Hemorrhagic Metastases from Breast Cancer and Melanoma. *J Comput Assist Tomogr*. 2016;40(5):803-805. doi:10.1097/RCT.0000000000000420.

93. Hermier M, Nighoghossian N. Contribution of susceptibility-weighted imaging to acute stroke assessment. *Stroke*. 2004;35(8):1989–1994.

94. Sehgal V, Delproposto Z, Haacke EM, Tong KA, Wycliffe N, Kido DK, Xu Y, Neelavalli J, Haddar D, Reichenbach JR. Clinical applications of neuroimaging with susceptibility-weighted imaging. *Journal of Magnetic Resonance Imaging*. 2005;22(4):439-450. doi:10.1002/jmri.20404.

95. Elnekeidy AE, Yehia A, Elfatatry A. Importance of susceptibility weighted imaging (SWI) in management of cerebro-vascular strokes (CVS). *Alexandria Journal of Medicine*. 2014;50(1):83-91. doi:10.1016/j.ajme.2013.05.006.

96. Thomas B, Somasundaram S, Thamburaj K, Kesavadas C, Gupta AK, Bodhey NK, Kapilamoorthy TR. Clinical applications of susceptibility weighted MR imaging of the brain–a pictorial review. *Neuroradiology*. 2008;50(2):105–116.

97. Naik D, Viswamitra S, Kumar AA, Srinath MG. Susceptibility weighted magnetic resonance imaging of brain: A multifaceted

powerful sequence that adds to understanding of acute stroke. *Ann Indian Acad Neurol*. 2014;17(1):58-61. doi:10.4103/0972-2327.128555.

98. Chen C-Y, Chen C-I, Tsai FY, Tsai P-H, Chan WP. Prominent Vessel Sign on Susceptibility-Weighted Imaging in Acute Stroke: Prediction of Infarct Growth and Clinical Outcome. *PLoS One*. 2015;10(6). doi:10.1371/journal.pone.0131118.

99. Park M-G, Oh S-J, Baik SK, Jung DS, Park K-P. Susceptibility-Weighted Imaging for Detection of Thrombus in Acute Cardioembolic Stroke. *J Stroke*. 2016;18(1):73-79. doi:10.5853/jos.2015.01417.

100. Haacke EM, Makki M, Ge Y, Maheshwari M, Sehgal V, Hu J, Selvan M, Wu Z, Latif Z, Xuan Y, Khan O, Garbern J, Grossman RI. Characterizing iron deposition in multiple sclerosis lesions using susceptibility weighted imaging. *Journal of Magnetic Resonance Imaging*. 2009;29(3):537-544. doi:10.1002/jmri.21676.

101. Souza JM de, Domingues RC, Cruz LCH, Domingues FS, Iasbeck T, Gasparetto EL. Susceptibility-Weighted Imaging for the Evaluation of Patients with Familial Cerebral Cavernous Malformations: A Comparison with T2-Weighted Fast Spin-Echo and Gradient-Echo Sequences. *American Journal of Neuroradiology*. 2008;29(1):154-158. doi:10.3174/ajnr.A0748.

102. George U, Jolappara M, Kesavadas C, Gupta AK. Susceptibility-weighted imaging in the evaluation of brain arteriovenous malformations. *Neurol India*. 2010;58(4):608-614. doi:10.4103/0028-3886.68668.

103. Jagadeesan BD, Delgado Almandoz JE, Moran CJ, Benzinger TLS. Accuracy of Susceptibility-Weighted Imaging for the Detection of Arteriovenous Shunting in Vascular Malformations of the Brain. *Stroke*. 2011;42(1):87-92. doi:10.1161/STROKEAHA.110.584862.

104. El-Koussy M, Schroth G, Gralla J, Brekenfeld C, Andres RH, Jung S, Shahin MA, Lovblad KO, Kiefer C, Kottke R. Susceptibility-Weighted MR Imaging for Diagnosis of Capillary Telangiectasia of the Brain. *American Journal of Neuroradiology*. 2012;33(4):715-720. doi:10.3174/ajnr.A2893.

105. Marsecano C, Perri M, Michelini G, Varrassi M, Splendiani A, di Cesare E, Masciocchi C, Gallucci M. Vascular malformation mimicking multiple sclerosis active plaque: Usefulness of susceptibility weighted imaging (SWI) to perform correct diagnosis. *Neuroradiol J*. 2015;28(5):488-492. doi:10.1177/1971400915609337.

106. Bartzokis G, Tishler TA. MRI evaluation of basal ganglia ferritin iron and neurotoxicity in Alzheimer's and Huntingon's disease. *Cell Mol Biol (Noisy-le-grand)*. 2000;46(4):821-833.

107. Acosta-Cabronero J, Williams GB, Cardenas-Blanco A, Arnold RJ, Lupson V, Nestor PJ. In Vivo Quantitative Susceptibility Mapping (QSM) in Alzheimer's Disease. *PLOS ONE*. 2013;8(11):e81093. doi:10.1371/journal.pone.0081093.

108. Bergen JMG van, Li X, Hua J, Schreiner SJ, Steininger SC, Quevenco FC, Wyss M, Gietl AF, Treyer V, Leh SE, Buck F, Nitsch RM, Pruessmann KP, Zijl PCM van, Hock C, Unschuld PG. Colocalization of cerebral iron with Amyloid beta in Mild Cognitive Impairment. *Scientific Reports*. 2016;6:35514. doi:10.1038/srep35514.

109. Barbosa JHO, Santos AC, Tumas V, Liu M, Zheng W, Haacke EM, Salmon CEG. Quantifying brain iron deposition in patients with Parkinson's disease using quantitative susceptibility mapping, R2 and R2*. *Magnetic Resonance Imaging*. 2015;33(5):559-565. doi:10.1016/j.mri.2015.02.021.

110. Murakami Y, Kakeda S, Watanabe K, Ueda I, Ogasawara A, Moriya J, Ide S, Futatsuya K, Sato T, Okada K, Uozumi T, Tsuji S, Liu T, Wang Y, Korogi Y. Usefulness of Quantitative Susceptibility Mapping for the Diagnosis of Parkinson Disease.

American Journal of Neuroradiology. 2015;36(6):1102-1108. doi:10.3174/ajnr.A4260.

111. van Bergen JMG, Hua J, Unschuld PG, Lim IAL, Jones CK, Margolis RL, Ross CA, van Zijl PCM, Li X. Quantitative susceptibility mapping suggests altered brain iron in premanifest Huntington's disease. *AJNR Am J Neuroradiol*. 2016;37(5):789-796. doi:10.3174/ajnr.A4617.

112. Langkammer C, Liu T, Khalil M, Enzinger C, Jehna M, Fuchs S, Fazekas F, Wang Y, Ropele S. Quantitative Susceptibility Mapping in Multiple Sclerosis. *Radiology*. 2013;267(2):551-559. doi:10.1148/radiol.12120707.

113. Chen W, Gauthier SA, Gupta A, Comunale J, Liu T, Wang S, Pei M, Pitt D, Wang Y. Quantitative Susceptibility Mapping of Multiple Sclerosis Lesions at Various Ages. *Radiology*. 2014;271(1):183-192. doi:10.1148/radiol.13130353.

114. Liu T, Surapaneni K, Lou M, Cheng L, Spincemaille P, Wang Y. Cerebral Microbleeds: Burden Assessment by Using Quantitative Susceptibility Mapping. *Radiology*. 2012;262(1):269-278. doi:10.1148/radiol.11110251.

115. Schweser F, Deistung A, Lehr BW, Reichenbach JR. Differentiation between diamagnetic and paramagnetic cerebral lesions based on magnetic susceptibility mapping. *Med Phys*. 2010;37(10):5165-5178. doi:10.1118/1.3481505.

116. Chen W, Zhu W, Kovanlikaya Ii, Kovanlikaya A, Liu T, Wang S, Salustri C, Wang Y. Intracranial Calcifications and Hemorrhages: Characterization with Quantitative Susceptibility Mapping. *Radiology*. 2013;270(2):496-505. doi:10.1148/radiol.13122640.

117. Deistung A, Schweser F, Wiestler B, Abello M, Roethke M, Sahm F, Wick W, Nagel AM, Heiland S, Schlemmer H-P, Bendszus M, Reichenbach JR, Radbruch A. Quantitative Susceptibility Mapping Differentiates between Blood Depositions

and Calcifications in Patients with Glioblastoma. *PLOS ONE*. 2013;8(3):e57924. doi:10.1371/journal.pone.0057924.

118. Wang Y, Spincemaille P, Liu Z, Dimov A, Deh K, Li J, Zhang Y, Yao Y, Gillen KM, Wilman AH, Gupta A, Tsiouris AJ, Kovanlikaya I, Chiang GC-Y, Weinsaft JW, Tanenbaum L, Chen W, Zhu W, Chang S, Lou M, Kopell BH, Kaplitt MG, Devos D, Hirai T, Huang X, Korogi Y, Shtilbans A, Jahng G-H, Pelletier D, Gauthier SA, Pitt D, Bush AI, Brittenham GM, Prince MR. Clinical quantitative susceptibility mapping (QSM): Biometal imaging and its emerging roles in patient care. *Journal of Magnetic Resonance Imaging*. 2017;46(4):951-971. doi:10.1002/jmri.25693.

119. Straub S, Laun FB, Emmerich J, Jobke B, Hauswald H, Katayama S, Herfarth K, Schlemmer H-P, Ladd ME, Ziener CH, Bonekamp D, Röthke MC. Potential of quantitative susceptibility mapping for detection of prostatic calcifications. *J Magn Reson Imaging*. 2017;45(3):889-898. doi:10.1002/jmri.25385.

120. Van de Moortele P-F, Pfeuffer J, Glover GH, Ugurbil K, Hu X. Respiration-induced B0 fluctuations and their spatial distribution in the human brain at 7 Tesla. *Magn Reson Med*. 2002;47:888-895. doi:10.1002/mrm.10145.

121. Gelderen P van, Zwart JA de, Starewicz P, Hinks RS, Duyn JH. Real-time shimming to compensate for respiration-induced B0 fluctuations. *Magnetic Resonance in Medicine*. 2007;57(2):362-368. doi:10.1002/mrm.21136.

122. Jehenson P, Westphal M, Schuff N. Analytical method for the compensation of eddy-current effects induced by pulsed magnetic field gradients in NMR systems. *Journal of Magnetic Resonance (1969)*. 1990;90(2):264-278. doi:10.1016/0022-2364(90)90133-T.

123. Boesch C, Gruetter R, Martin E. Temporal and spatial analysis of fields generated by eddy currents in superconducting magnets: Optimization of corrections and quantitative characterization of

magnet/gradient systems. *Magnetic Resonance in Medicine*. 1991;20(2):268-284. doi:10.1002/mrm.1910200209.

124. Liu Q, Hughes DG, Allen PS. Quantitative characterization of the eddy current fields in a 40-cm bore superconducting magnet. *Magnetic Resonance in Medicine*. 1994;31(1):73-76. doi:10.1002/mrm.1910310112.

125. Hu X, Kim SG. Reduction of signal fluctuation in functional MRI using navigator echoes. *Magn Reson Med*. 1994;31(5):495-503.

126. Wu Y, Chronik BA, Bowen C, Mechefske CK, Rutt BK. Gradient-induced acoustic and magnetic field fluctuations in a 4T whole-body MR imager. *Magnetic Resonance in Medicine*. 2000;44(4):532-536. doi:10.1002/1522-2594(200010)44:4<532::AID-MRM6>3.0.CO;2-Q.

127. Clayton DB, Elliott MA, Leigh JS, Lenkinski RE. 1H Spectroscopy without Solvent Suppression: Characterization of Signal Modulations at Short Echo Times. *Journal of Magnetic Resonance*. 2001;153(2):203-209. doi:10.1006/jmre.2001.2442.

128. Foerster BU, Tomasi D, Caparelli EC. Magnetic field shift due to mechanical vibration in functional magnetic resonance imaging. *Magnetic Resonance in Medicine*. 2005;54(5):1261-1267. doi:10.1002/mrm.20695.

129. Lange T, Maclaren J, Buechert M, Zaitsev M. Spectroscopic imaging with prospective motion correction and retrospective phase correction. *Magnetic Resonance in Medicine*. 2012;67(6):1506-1514. doi:10.1002/mrm.23136.

130. Wowk B, McIntyre MC, Saunders JK. k-Space detection and correction of physiological artifacts in fMRI. *Magn Reson Med*. 1997;38(6):1029-1034.

131. Noll DC, Genovese CR, Vazquez AL, O'Brien JL, Eddy WF. Evaluation of respiratory artifact correction techniques in

multishot spiral functional MRI using receiver operator characteristic analyses. *Magn Reson Med*. 1998;40(4):633-639.

132. Liu H-L, Kochunov P, Lancaster JL, Fox PT, Gao J-H. Comparison of navigator echo and centroid corrections of image displacement induced by static magnetic field drift on echo planar functional MRI. *Journal of Magnetic Resonance Imaging*. 2001;13(2):308-312. doi:10.1002/1522-2586(200102)13:2<308::AID-JMRI1044>3.0.CO;2-L.

133. Durand E, Moortele P-F van de, Pachot-Clouard M, Bihan DL. Artifact due to B0 fluctuations in fMRI: Correction using the k-space central line. *Magnetic Resonance in Medicine*. 2001;46(1):198-201. doi:10.1002/mrm.1177.

134. Gretsch F, Marques JP, Gallichan D. Investigating the accuracy of FatNav-derived estimates of temporal B0 changes and their application to retrospective correction of high-resolution 3D GRE of the human brain at 7T. *Magnetic Resonance in Medicine*. 2018;80(2):585-597. doi:10.1002/mrm.27063.

135. Glover GH, Lai S. Self-navigated spiral fMRI: interleaved versus single-shot. *Magn Reson Med*. 1998;39(3):361-368.

136. Vannesjo SJ, Wilm BJ, Duerst Y, Gross S, Brunner DO, Dietrich BE, Schmid T, Barmet C, Pruessmann KP. Retrospective correction of physiological field fluctuations in high-field brain MRI using concurrent field monitoring. *Magn Reson Med*. 2015;73:1833-1843. doi:10.1002/mrm.25303.

137. Wilm BJ, Barmet C, Pavan M, Pruessmann KP. Higher order reconstruction for MRI in the presence of spatiotemporal field perturbations. *Magnetic Resonance in Medicine*. 2011;65(6):1690-1701. doi:10.1002/mrm.22767.

138. Hofer DC, Kahwaty VN, Valentino CR. NMR field frequency lock system. August 1978. http://www.freepatentsonline.com/4110681.html. Accessed August 10, 2018.

139. Hoult DI, Richards RE, Styles P. A novel field-frequency lock for a superconducting spectrometer. *Journal of Magnetic Resonance (1969)*. 1978;30(2):351-365. doi:10.1016/0022-2364(78)90106-3.

140. Boer VO, Bank BL vd, Vliet G van, Luijten PR, Klomp DWJ. Direct B0 field monitoring and real-time B0 field updating in the human breast at 7 tesla. *Magnetic Resonance in Medicine*. 2012;67(2):586-591. doi:10.1002/mrm.23272.

141. Duerst Y, Wilm BJ, Wyss M, Dietrich BE, Gross S, Schmid T, Brunner DO, Pruessmann KP. Utility of real-time field control in T2*-Weighted head MRI at 7T. *Magn Reson Med*. 2016;76:430-439. doi:10.1002/mrm.25838.

142. Wyss M, Duerst Y, Nanz D, Kasper L, Wilm BJ, Dietrich BE, Gross S, Schmid T, Brunner DO, Pruessmann KP. Feedback field control improves the precision of T2 * quantification at 7 T. *NMR Biomed*. 2017;30(10). doi:10.1002/nbm.3753.

143. Özbay PS, Duerst Y, Wilm BJ, Pruessmann KP, Nanz D. Enhanced quantitative susceptibility mapping (QSM) using real-time field control. *Magnetic Resonance in Medicine*. 2018;79(2):770-778. doi:10.1002/mrm.26735.

144. Derbyshire JA, Wright GA, Henkelman RM, Hinks RS. Dynamic scan-plane tracking using MR position monitoring. *Journal of Magnetic Resonance Imaging*. 1998;8(4):924-932. doi:10.1002/jmri.1880080423.

145. Krueger S, Schaeffter T, Weiss S, Nehrke K, Rozijn T, Boernert P. Prospective Intra-Image Compensation for Non-Periodic Rigid Body Motion Using Active Markers. :1.

146. Dumoulin CL, Souza SP, Darrow RD. Real-time position monitoring of invasive devices using magnetic resonance. *Magnetic Resonance in Medicine*. 1993;29(3):411-415. doi:10.1002/mrm.1910290322.

147. Ooi MB, Krueger S, Muraskin J, Thomas WJ, Brown TR. Echo-planar imaging with prospective slice-by-slice motion correction using active markers. *Magn Reson Med*. 2011;66(1):73-81. doi:10.1002/mrm.22780.

148. Alhamud A, Taylor PA, van der Kouwe AJW, Meintjes EM. Real-time measurement and correction of both B0 changes and subject motion in diffusion tensor imaging using a double volumetric navigated (DvNav) sequence. *NeuroImage*. 2016;126:60-71. doi:10.1016/j.neuroimage.2015.11.022.

149. Vannesjo SJ, Duerst Y, Vionnet L, Dietrich BE, Pavan M, Gross S, Barmet C, Pruessmann KP. Gradient and shim pre-emphasis by inversion of a linear time-invariant system model. *Magnetic Resonance in Medicine*. 2017;78(4):1607-1622. doi:10.1002/mrm.26531.

150. Aranovitch A, Haeberlin M, Gross S, Dietrich BE, Kasper L, Wilm BJ, Brunner DO, Schmid T, Pruessmann KP. Active-marker motion detection with real-time field tracking in the laboratory frame. *In Proceedings of the 25th Annual Meeting of ISMRM, Honolulu, 2017*. p. 0300.

151. Dietrich BE, Brunner DO, Wilm BJ, Barmet C, Pruessmann KP. Continuous Magnetic Field Monitoring Using Rapid Re-Excitation of NMR Probe Sets. *IEEE Transactions on Medical Imaging*. 2016;35(6):1452-1462. doi:10.1109/TMI.2016.2514608.

152. Looser A, Barmet C, Fox T, Blacque O, Gross S, Nussbaum J, Pruessmann KP, Alberto R. Ultrafast Ligand Self-Exchanging Gadolinium Complexes in Ionic Liquids for NMR Field Probes. *Inorg Chem*. 2018;57(4):2314-2319. doi:10.1021/acs.inorgchem.7b03191.

153. Mansfield P, Chapman B. Active magnetic screening of coils for static and time-dependent magnetic field generation in NMR imaging. *J Phys E: Sci Instrum*. 1986;19(7):540–545. doi:10.1088/0022-3735/19/7/008.

154. Mansfield P, Chapman B. Multishield active magnetic screening of coil structures in NMR. *Journal of Magnetic Resonance (1969)*. 1987;72(2):211-223. doi:10.1016/0022-2364(87)90283-6.

155. Turner R. Gradient coil design: A review of methods. *Magnetic Resonance Imaging*. 1993;11(7):903-920. doi:10.1016/0730-725X(93)90209-V.

156. Duerst Y, Wilm BJ, Dietrich BE, Gross S, Schmid T, Brunner DO, Pruessmann KP. Real-Time Field Control Using Full 3rd-Order Matrix Pre-Emphasis. *In Proceedings of the 24th Annual Meeting of ISMRM, Singapore, 2016*. p. 0045.

157. van Rooden S, Versluis MJ, van der Grond J, van Buchem MA, van Zijl P, Webb AG. High-field imaging of neurodegenerative diseases. *Neuroimaging Clin N Am*. 2012;22(2):159-171, ix. doi:10.1016/j.nic.2012.02.005.

158. Andersen M, Hanson LG, Madsen KH, Wezel J, Boer V, van der Velden T, van Osch MJP, Klomp D, Webb AG, Versluis MJ. Measuring motion-induced B0-fluctuations in the brain using field probes. *Magn Reson Med*. 2016;75:2020-2030. doi:10.1002/mrm.25802.

159. Gross S, Duerst Y, Vionnet L, Barmet C, Pruessmann KP. B0-Atlas with Field-Probe Guidance: Application in Real-Time Field Control. *In Proceedings of the 24th Annual Meeting of ISMRM, Singapore, 2016*. p. 0930.

160. Vannesjo SJ, Clare S, Kasper L, Tracey I, Miller KL. Trace-based correction of breathing-induced field fluctuations in T2*-weighted imaging of the spinal cord. *bioRxiv*. September 2018:406371. doi:10.1101/406371.

161. Aghaeifar A, Mirkes C, Bause J, Steffen T, Avdievitch N, Henning A, Scheffler K. Dynamic B0 shimming of the human brain at 9.4 T with a 16-channel multi-coil shim setup. *Magnetic*

Resonance in Medicine. 2018;80(4):1714-1725. doi:10.1002/mrm.27110.

162. Juchem C, Nixon TW, McIntyre S, Boer VO, Rothman DL, de Graaf RA. Dynamic multi-coil shimming of the human brain at 7T. *Journal of Magnetic Resonance*. 2011;212(2):280-288. doi:10.1016/j.jmr.2011.07.005.

163. Littin S, Jia F, Layton KJ, Kroboth S, Yu H, Hennig J, Zaitsev M. Development and implementation of an 84-channel matrix gradient coil. *Magnetic Resonance in Medicine*. 2018;79(2):1181-1191. doi:10.1002/mrm.26700.

164. Harris CT, Handler WB, Chronik BA. A new approach to shimming: The dynamically controlled adaptive current network. *Magnetic Resonance in Medicine*. 2014;71(2):859-869. doi:10.1002/mrm.24724.

165. Jezzard P, Clare S. Sources of distortion in functional MRI data. *Hum Brain Mapp*. 1999;8(2-3):80-85.

166. Sulikowska A, Wharton S, Glover PM, Gowland PA. Will field shifts due to head rotation compromise motion correction? *In Proceedings of the 22th Annual Meeting of ISMRM, Milano, 2014*. p. 0885.

167. Bischoff BI, Smith JA, Mougin OE, Spencer GS, Aphiwatthanasumet K, Gowland PA, Bowtell RW. Relating external magnetic field changes to head movement using motion and field cameras. *In Proceedings of the 25th Annual Meeting of ISMRM, Hawaii, 2017*. p. 0303.

168. Birn RM, Bandettini PA, Cox RW, Jesmanowicz A, Shaker R. Magnetic field changes in the human brain due to swallowing or speaking. *Magn Reson Med*. 1998;40(1):55-60.

169. Ward HA, Riederer SJ, Jack CR. Real-time autoshimming for echo planar timecourse imaging. *Magnetic Resonance in Medicine*. 2002;48(5):771-780. doi:10.1002/mrm.10259.

170. Wezel J, Boer VO, van der Velden TA, Webb AG, Klomp DWJ, Versluis MJ, van Osch MJP, Garpebring A. A comparison of navigators, snap-shot field monitoring, and probe-based field model training for correcting B0-induced artifacts in T2*-weighted images at 7 T. *Magn Reson Med*. November 2016:n/a-n/a. doi:10.1002/mrm.26524.

171. Marques J p., Bowtell R. Application of a Fourier-based method for rapid calculation of field inhomogeneity due to spatial variation of magnetic susceptibility. *Concepts Magn Reson*. 2005;25B(1):65-78. doi:10.1002/cmr.b.20034.

172. Hoinkiss DC, Porter DA. Prospective motion correction in 2D multishot MRI using EPI navigators and multislice-to-volume image registration. *Magnetic Resonance in Medicine*. 2017;78(6):2127-2135. doi:10.1002/mrm.26951.

173. Reber PJ, Wong EC, Buxton RB, Frank LR. Correction of off resonance-related distortion in echo-planar imaging using EPI-based field maps. *Magnetic Resonance in Medicine*. 1998;39(2):328-330. doi:10.1002/mrm.1910390223.

174. Hutton C, Bork A, Josephs O, Deichmann R, Ashburner J, Turner R. Image Distortion Correction in fMRI: A Quantitative Evaluation. *NeuroImage*. 2002;16(1):217-240. doi:10.1006/nimg.2001.1054.

175. Balchandani P, Naidich TP. Ultra-High-Field MR Neuroimaging. *American Journal of Neuroradiology*. 2015;36(7):1204-1215. doi:10.3174/ajnr.A4180.

176. Doan NT, Bogaard SJA van den, Dumas EM, Webb AG, Buchem MA van, Roos RAC, Grond J van der, Reiber JHC, Milles J. Texture analysis of ultrahigh field T2*-weighted MR images of the brain: Application to Huntington's disease. *Journal of Magnetic Resonance Imaging*. 2014;39(3):633-640. doi:10.1002/jmri.24199.

177. Niccolini F, Politis M. Neuroimaging in Huntington's disease. *World J Radiol*. 2014;6(6):301-312. doi:10.4329/wjr.v6.i6.301.

178. Barnes J, Bartlett JW, van de Pol LA, Loy CT, Scahill RI, Frost C, Thompson P, Fox NC. A meta-analysis of hippocampal atrophy rates in Alzheimer's disease. *Neurobiology of Aging*. 2009;30(11):1711-1723. doi:10.1016/j.neurobiolaging.2008.01.010.

179. Kenkhuis B, Jonkman LE, Bulk M, Buijs M, Boon BDC, Bouwman FH, Geurts JJG, van de Berg WDJ, van der Weerd L. 7T MRI allows detection of disturbed cortical lamination of the medial temporal lobe in patients with Alzheimer's disease. *NeuroImage: Clinical*. 2019;21:101665. doi:10.1016/j.nicl.2019.101665.

180. Plantinga BR, Temel Y, Roebroeck A, Uludağ K, Ivanov D, Kuijf ML, ter Haar Romenij BM. Ultra-high field magnetic resonance imaging of the basal ganglia and related structures. *Front Hum Neurosci*. 2014;8. doi:10.3389/fnhum.2014.00876.

181. Federau C, Gallichan D. Motion-Correction Enabled Ultra-High Resolution In-Vivo 7T-MRI of the Brain. *PLOS ONE*. 2016;11(5):e0154974. doi:10.1371/journal.pone.0154974.

182. Mattern H, Sciarra A, Lüsebrink F, Acosta-Cabronero J, Speck O. Prospective motion correction improves high-resolution quantitative susceptibility mapping at 7T. *Magnetic Resonance in Medicine*. 0(0). doi:10.1002/mrm.27509.

183. Versluis MJ, Sutton BP, Bruin PW de, Börnert P, Webb AG, Osch MJ van. Retrospective image correction in the presence of nonlinear temporal magnetic field changes using multichannel navigator echoes. *Magnetic Resonance in Medicine*. 2012;68(6):1836-1845. doi:10.1002/mrm.24202.

184. Vionnet L, Aranovitch A, Duerst Y, Haeberlin M, Dietrich BE, Gross S, Kasper L, Schmid T, Pruessmann KP. Simultaneous prospective motion correction and feedback field control: T2*

weighted imaging at high field. *In Proceedings of the 25th Annual Meeting of ISMRM, Hawaii, 2017*. p. 0306.

185. Schaltenbrand G, Wahren W. *Atlas for Stereotaxy of the Human Brain*. Georg Thieme Verlag; 1977.

186. Büttner-Ennever JA, Horn AKE. *Olszewski and Baxter's Cytoarchitecture of the Human Brainstem*. 3rd ed. S. Karger AG, Basel; 2014.

187. von Hagens G, Whalley A, Maschke R, Kriz W. *Schnittanatomie Des Menschlichen Gehirns*. Steinkopff Verlag Darmstadt; 1990.

188. Cho Z-H. *7.0 Tesla MRI Brain Atlas*. 2nd ed. Springer-Verlag Berlin Heidelberg; 2015.

189. Schneider TM, Deistung A, Biedermann U, Matthies C, Ernestus R-I, Volkmann J, Heiland S, Bendszus M, Reichenbach JR. Susceptibility Sensitive Magnetic Resonance Imaging Displays Pallidofugal and Striatonigral Fiber Tracts. *Oper Neurosurg (Hagerstown)*. 2016;12(4):330-338. doi:10.1227/NEU.0000000000001256.

190. Horn AKE, Adamczyk C. Chapter 9 - Reticular Formation: Eye Movements, Gaze and Blinks. In: Mai JK, Paxinos G, eds. *The Human Nervous System (Third Edition)*. San Diego: Academic Press; 2012:328-366. doi:10.1016/B978-0-12-374236-0.10009-4.

191. Fukunaga M, Li T-Q, van Gelderen P, de Zwart JA, Shmueli K, Yao B, Lee J, Maric D, Aronova MA, Zhang G, Leapman RD, Schenck JF, Merkle H, Duyn JH. Layer-specific variation of iron content in cerebral cortex as a source of MRI contrast. *Proc Natl Acad Sci U S A*. 2010;107(8):3834-3839. doi:10.1073/pnas.0911177107.

192. Aggarwal M, Zhang J, Pletnikova O, Crain B, Troncoso J, Mori S. Feasibility of creating a high-resolution 3D diffusion tensor imaging based atlas of the human brainstem: A case study at

11.7T. *NeuroImage*. 2013;74:117-127. doi:10.1016/j.neuroimage.2013.01.061.

193. Deistung A, Schäfer A, Schweser F, Biedermann U, Güllmar D, Trampel R, Turner R, Reichenbach JR. High-Resolution MR Imaging of the Human Brainstem In vivo at 7 Tesla. *Front Hum Neurosci*. 2013;7. doi:10.3389/fnhum.2013.00710.

194. Deistung A, Schäfer A, Schweser F, Biedermann U, Turner R, Reichenbach JR. Toward in vivo histology: A comparison of quantitative susceptibility mapping (QSM) with magnitude-, phase-, and R2$*$-imaging at ultra-high magnetic field strength. *NeuroImage*. 2013;65:299-314. doi:10.1016/j.neuroimage.2012.09.055.

195. Hasan KM, Kamali A, Iftikhar A, Kramer LA, Papanicolaou AC, Fletcher JM, Ewing-Cobbs L. Diffusion tensor tractography quantification of the human corpus callosum fiber pathways across the lifespan. *Brain Research*. 2009;1249:91-100. doi:10.1016/j.brainres.2008.10.026.

196. Wiggins CJ, Schäfer A, Dhital B, Le Bihan D, Turner R. After over 200 years, 7 T magnetic resonance imaging reveals the foliate structure of the human corpus callosum in vivo. *BJR*. 2017;90(1073):20160906. doi:10.1259/bjr.20160906.

197. Soellinger M, Rutz AK, Kozerke S, Boesiger P. 3D cine displacement-encoded MRI of pulsatile brain motion. *Magnetic Resonance in Medicine*. 2009;61(1):153-162. doi:10.1002/mrm.21802.

198. Pohmann R, Speck O, Scheffler K. Signal-to-noise ratio and MR tissue parameters in human brain imaging at 3, 7, and 9.4 tesla using current receive coil arrays. *Magnetic Resonance in Medicine*. 2016;75(2):801-809. doi:10.1002/mrm.25677.

199. Bortolotti L, Smith JA, Gowland P, Bowtell RW. Simulation of external magnetic field changes due to head motion during 7

Tesla MRI scan. *In Proceedings of the 27th Annual Meeting of ISMRM, Montreal, 2019*. p. 4432.

200. Schäfer A, Forstmann BU, Neumann J, Wharton S, Mietke A, Bowtell R, Turner R. Direct visualization of the subthalamic nucleus and its iron distribution using high-resolution susceptibility mapping. *Human Brain Mapping*. 2012;33(12):2831-2842. doi:10.1002/hbm.21404.

201. Dietrich BE, Nussbaum J, Wilm BJ, Reber J, Pruessmann KP. Thermal Variation and Temperature-Based Prediction of Gradient Response. *In Proceedings of the 25th Annual Meeting of ISMRM, Hawaii, 2017*. p. 0079.

202. Nussbaum J, Wilm BJ, Dietrich BE, Pruessmann KP. Improved thermal modelling and prediction of gradient response using sensor placement guided by infrared photography. *In Proceedings of the 26th Annual Meeting of ISMRM, Paris, 2018*. p. 4210.

203. Yarach U, Luengviriya C, Danishad A, Stucht D, Godenschweger F, Schulze P, Speck O. Correction of gradient nonlinearity artifacts in prospective motion correction for 7T MRI. *Magn Reson Med*. 2015;73:1562-1569. doi:10.1002/mrm.25283.

204. McKiernan EF, O'Brien JT. 7T MRI for neurodegenerative dementias in vivo: a systematic review of the literature. *J Neurol Neurosurg Psychiatry*. 2017;88(7):564-574. doi:10.1136/jnnp-2016-315022.

Acknowledgements

This thesis completes five years of research and development at the Institute for Biomedical Engineering at the ETH Zurich and University of Zurich. Many people have contributed to the present work and I would like to express my gratitude to:

Prof Dr Klaas Pruessmann, who supervised this thesis and who gave me the chance to pursue the PhD research in his lab and provided an inspiring and stimulating atmosphere with much freedom to explore different ideas. In particular, I would like to express my gratitude for the time and effort he put into discussions with me over the past years and the invaluable advice and ideas he gave me. His ability to narrow down complex phenomena to the physics and basic principles they are governed by has always impressed me. Moreover, I would like to thank Klaas for his support when I competed for the young investigator award 2018.

Prof Dr Klaus Scheffler, for co-examining this thesis.

Max, who pioneered motion detection with NMR field probes in our group and introduced me to the topic and MRI in general. I had the pleasure to work with him during my master thesis and during the first two years of my PhD. Even after his time at the IBT, he kept his fascination with MRI and his interest and enthusiasm for motion correction. Also, I thank him for his feedback on two paper manuscripts and parts of the thesis.

Laetitia, for the fruitful collaboration in the project of simultaneous field control and motion correction. In particular, we went together through countless hours at the 7T, initially making the whole setup work and,

eventually, carrying out measurements to characterize the method and to obtain fascinating imaging data.

Simon, who built the field probes that were used for most of the experiments presented in this work and for proof reading two paper manuscripts and parts of the thesis.

Beni, Berti and David for their support with the operation of the NI system at the 3T and 7T.

Roger for ensuring smooth scanner operation and his help when problems occurred.

My office mates Romain, Maria, Christoph and, formerly, Yolanda and Matteo. In total, I have spent so much time in our office and therefore I highly value the friendly atmosphere and the laughs we had, which made me enjoy coming to the office.

All other current and former members of our group for the lunches, the discussions, the retreats and all activities as well as generally for the pleasant environment to be in.

Prof Dr Kozerke and his group members for discussions on MRI and for contributing to the great atmosphere on our floor.

Isabel and Marianne for taking care and managing of the administrative issues.

Bruno for running and maintaining the IT and taking care of storage issues occurring with the large amounts of data.

Stephen, for his great skill and help with mechanical construction.

My friends and family from all around, from Frankfurt and Zurich particularly, who are just awesome and constitute such an important part of my life.

And finally, my parents, for their care, support and advice. For endowing me with traits and values that have guided me ever since.